cAMP−EPAC−PKCε−RIM1α signaling regulates presynaptic long-term potentiation and motor learning

Xin-Tai Wang[1,2†], Lin Zhou[1†], Fang-Xiao Xu[1], De-Juan Wang[1], Xin-Yu Cai[1], Yin Wang[3], Sheng-Jian Ji,[4], Martijn Schonewille[5], J. Julius Zhu[6,*], Chris I. De Zeeuw[5,7,*], Ying Shen[1,*]

[1] Department of Physiology and Department of Psychiatry, Sir Run Run Shaw Hospital, Zhejiang University School of Medicine, Hangzhou 310058, China; [2] Institute of Life Sciences, College of Life and Environmental Sciences, Hangzhou Normal University, Hangzhou 311121, China; [3] Key Laboratory of Cranial Cerebral Diseases, Department of Neurobiology of Basic Medical College, Ningxia Medical University, Yinchuan 750004, China; [4] Department of Biology, Southern University of Science and Technology, Shenzhen 518055, China; [5] Department of Neuroscience, Erasmus MC, 3000 DR Rotterdam, The Netherlands; [6] Department of Pharmacology, University of Virginia, Charlottesville, VA 22904, U.S.A.; [7] Netherlands Institute for Neuroscience, Royal Academy of Sciences, 1105 BA Amsterdam, The Netherlands.

***For correspondence:** yshen@zju.edu.cn or c.dezeeuw@erasmusmc.nl or jjz4n@virginia.edu.

[†]These authors contributed equally to this work.

Competing interests: The authors declare that no competing interests exist.

Abstract

The cerebellum is involved in learning of fine motor skills, yet whether presynaptic plasticity contributes to such learning remains elusive. Here we report that the EPAC-PKCε module has a critical role in a presynaptic form of long-term potentiation in the cerebellum and motor behavior. Presynaptic cAMP−EPAC−PKCε signaling cascade induces a previously unidentified threonine phosphorylation of RIM1α, and thereby initiates the assembly of the Rab3A−RIM1α−Munc13-1 tripartite complex that facilitates docking and release of synaptic vesicles. Granule cell-specific blocking of EPAC−PKCε signaling abolishes presynaptic long-term potentiation at the parallel fiber to Purkinje cell synapses and impairs basic performance and learning of cerebellar motor behavior. These results unveil a functional relevance of presynaptic plasticity that is regulated through a novel signaling cascade, thereby enriching the spectrum of cerebellar learning mechanisms.

Introduction

The cerebellum has historically been viewed as a motor coordination center (*Ito, 2005*). Recent evidence implicates that the cerebellum is also involved in a variety of learning-dependent high-level behaviors, including motor precision (*Wagner and Luo, 2020*; *De Zeeuw, 2021*) as well as cognitive and emotional functions (*Schmahmann et al., 2019*). The unique capability of the cerebellum to govern fine-tuned motor and cognitive skills at a high temporal resolution critically depends on delicate coordination of multiple forms of plasticity (*De Zeeuw, 2021*). Indeed, recent studies indicate that, in addition to the renowned postsynaptic long-term depression (LTD) (*Ito, 2005*) and long-term potentiation (LTP) (*Schonewille et al., 2010*), other forms of synaptic or non-synaptic plasticity may also contribute to cerebellar motor learning (*Raymond and Medina, 2018*; *De Zeeuw, 2021*). However, the molecular underpinnings of presynaptic plasticity in the cerebellar cortex are merely starting to be explored (*Wang et al., 2021a*), and more importantly, whether presynaptic plasticity plays a role in cerebellar motor learning remains to be elucidated (*Le Guen and De Zeeuw, 2010*; *De Zeeuw, 2021*).

In this study, we identified a new presynaptic signaling module that comprises EPAC (exchange protein directly activated by cyclic adenosine monophosphate, cAMP) and PKCε (epsilon isozyme of protein kinase C), which turns out to control threonine phosphorylation of RIM1α, initiate assembly of a Rab3A-RIM1α-Munc13-1 tripartite complex, and thereby facilitate docking and release of synaptic vesicles at parallel fiber (PF) to Purkinje cell (PC) synapses. Importantly, presynaptic ablation of either EPAC or PKCε is sufficient to inhibit presynaptic LTP and impair motor performance and motor learning. These data unveil a new signaling cascade governing presynaptic LTP and for the first time clarify that presynaptic plasticity is required for

56 cerebellar motor learning.

Results

EPAC induces PKCε-dependent threonine phosphorylation of RIM1α

In order to study the function of EPACs at synapses, a series of centrifugations were employed to prepare cerebellar synaptosomes containing a number of synaptic proteins (*Figure 1A*). We found that most of EPAC1 and EPAC2 overlapped with vesicle glutamate transporter 1 (vGluT1) (*Figure 1B*), which is enriched in PF terminals (*Hioki et al., 2013*). Co-immunoprecipitation (co-IP) performed using synaptosomes showed that both EPAC1 and EPAC2 were precipitated by the RIM1 antibody (*Figure 1C*), indicating the ability of EPAC to interact with RIM1. To specify the action of EPAC, RIM1 was extracted from the synaptosomes by anti-RIM1 antibody-based co-IP (*Figure 1A*). Interestingly, we found that pan-phospho-threonine (p-Thr) antibodies detected only a weak signal in control synaptosomes, but a strong band in synaptosomes treated with 8-pCPT, a specific activator of EPAC (*Figure 1D*). In contrast, the level of pan-phospho-serine (p-Ser) remained unchanged after 8-pCPT treatment (*Figure 1D*). These results were confirmed by co-transfecting HA-RIM1α with Flag-EPAC1 or Flag-EPAC2 in HEK cells, where both types of EPAC as well as RIM1α were preferentially distributed along the cell membrane (*Figure 1–figure supplement 1A*). Again, HA-RIM1α was precipitated with the HA antibody to characterize p-Ser and p-Thr of RIM1α. Consistent with *in vivo* assay, neither EPAC1 nor EPAC2 altered serine phosphorylation of RIM1α, but both increased phosphorylation of threonine (*Figure 1–figure supplement 1B*).

Since EPAC is an effector of cAMP, we wondered whether cAMP also causes the phosphorylation of threonine sites of RIM1, which comprises 27 of such sites (*Figure 1–figure supplement 1C*). Hence, forskolin, an activator of adenylate cyclase, and ESI-09, an inhibitor of

EPAC (Gutierrez-Castellanos et al., 2017), were administered to synaptosomes, after which RIM1 p-Thr was measured. RIM1 p-Thr was vastly increased by forskolin alone, but not following co-application of both forskolin and ESI-09 (*Figure 1E*), indicating that cAMP leads to EPAC-dependent threonine phosphorylation of RIM1. We continued to examine the consequences on RIM1 phosphorylation in EPAC1 and EPAC2 double-knockout ($Epac^{dKO}$) mice. Using synaptosomes purified from $Epac^{dKO}$ mice, we found that RIM1 p-Thr was significantly reduced, whereas RIM1 p-Ser was unchanged (*Figure 1F*). Meanwhile, knockout of *Epac* did not change the expression of RIM1 (*Figure 1F*). The difference of RIM1 p-Thr in the $Epac^{dKO}$ mice was not accompanied by major structural difference, as EPAC deficiency did not interfere with lobule thickness or number of PC spines (*Figure 1–figure supplement 2A and B*). Together, these data strongly indicate that EPAC is necessary and sufficient to induce threonine phosphorylation of RIM1.

EPAC by itself lacks the kinase activity that is required for phosphorylation (*Kawasaki et al., 1998*; *Cheng et al., 2008*), which raises a question how EPAC mediates the phosphorylation of RIM1. We hypothesized that EPAC might act on RIM1 through the Rap1-PLCε-PKCε module (*Figure 1G*), which is shown to be activated by EPAC in neuroblastoma cells (*Schmidt et al., 2001*), dorsal root ganglion neurons (*Hucho et al., 2005*), as well as heart cells (*Oestreich et al., 2009*). Our hypothesis was corroborated by several lines of evidence. First, when Flag-EPAC1 and Flag-EPAC2 were expressed in HEK cells, phosphorylation at PKCε-S729 was significantly increased by both EPAC1 or EPAC2 expression, whereas phosphorylation at PKCα-S657 or PKCα-T638 was not altered (*Figure 1–figure supplement 3A*). Second, PKCε overlapped with vGluT1 in cerebellar synaptosomes (*Figure 1H*), suggesting the presence of PKCε at PF synapses.

Western blots showed that phosphorylation at PKCε-S729, but not at PKCα-S657 or PKCα-T638, was increased in cerebellar synaptosomes treated with 8-pCPT, whereas control buffer had no impact (*Figure 1I*). Third, phosphorylation at PKCε-S729 in the synaptosomes was significantly reduced by EPAC ablation ($Epac^{dKO}$ versus WT), whereas phosphorylation at PKCα-S657 or PKCα-T638 was unchanged (*Figure 1J*). These data indicate that EPAC is able to regulate PKCε activity. We next investigated whether PKCε can phosphorylate RIM1α. HA-RIM1α and His-PKCε were co-transfected into HEK cells and co-IP experiments showed that PKCε can bind to RIM1α (*Figure 1–figure supplement 3B*). In addition, RIM1α p-Thr was significantly increased in cells transfected with PKCε compared to the control (*Figure 1–figure supplement 3C*). To confirm *in vitro* findings, we generated mice with *Prkce* (the gene coding for PKCε) deletion specifically in cerebellar granule cells ($Prkce^{cKO}$) by crossing *Math1*-Cre (*Wang et al., 2021b*) with $Prkce^{f/f}$ mice (*Figure 1–figure supplement 2C-F*), and $Prkce^{cKO}$ mice showed normal lobule thickness and number of spines of PCs (*Figure 1–figure supplement 2G-H*). Subsequently, RIM1 phosphorylation was examined in cerebellar synaptosomes derived from $Prkce^{f/f}$ and $Prkce^{cKO}$ mice. Similar to the findings in $Epac^{dKO}$ mice, RIM1 p-Thr was significantly reduced, whereas both RIM1 p-Ser and total RIM1 were unchanged in $Prkce^{cKO}$ mice (*Figure 1K*). These data indicate that PKCε is able to regulate RIM1 p-Thr phosphorylation.

Finally, several lines of evidence demonstrated the causal relationship between EPAC and PKCε on the phosphorylation of RIM1α. First, we applied 8-pCPT alone or with εV1-2 (a selective PKCε inhibitor) to WT synaptosomes. The addition of εV1-2 to the synaptosomes strongly attenuated RIM1 p-Thr induced by 8-pCPT (*Figure 1–figure supplement 3D*). In contrast, RIM1 p-Thr was not affected by co-application of Gö6976, a PKCα/β inhibitor (*Figure 1–figure*

supplement 3D). Second, we administered phorbol 12-myristate 13-acetate (PMA), an activator of all PKC isoforms, alone or along with εV1-2 or Gö6976, so as to inhibit PKCε or PKCα/β, respectively. εV1-2, but not Gö6976, significantly suppressed RIM1α p-Thr in the synaptosomes (*Figure 1–figure supplement 3E*). Third, RIM1 phosphorylation was examined in *Prkce*^{cKO} synaptosomes, which were treated with either control saline or 8-pCPT. In this scenario, neither p-Thr nor p-Ser of RIM1 was changed (*Figure 1L*). Overall, these data strongly indicate that EPAC can trigger RIM1α p-Thr phosphorylation and that this activation requires PKCε.

EPAC-PKCε module is critical to vesicle docking and presynaptic release through acting on the Rab3A-RIM1α-Munc13-1 complex

Our finding that the EPAC-PKCε module regulates RIM1 activity through phosphorylation leads to an interesting question: does the EPAC-PKCε module function on synaptic formation and function through acting on RIM1? which is known to be critical to organization of the presynaptic active zone and neurotransmitter release (*Schoch et al., 2002*; *Han et al., 2011*; *Kaeser et al., 2011*; *Acuna et al., 2016*; *Persoon et al., 2019*).

To address this question, we first visualized PF-PC synapses using transmission electron microscopy (EM), in which PF boutons were identified by their presence of synaptic vesicles as well as their asymmetric synaptic contacts with PC spines (*Figure 2A and B*). No apparent abnormality was found in the size of the postsynaptic density or the synaptic cleft of PF-PC synapses in either *Epac*^{dKO} (n = 4) or *Prkce*^{cKO} (n = 4) mice, compared to corresponding WT (n = 4) and *Prkce*$^{f/f}$ (n = 4) mice (*Figure 2A and B*). However, the deletion of *Epac* significantly decreased the number of the docked vesicle pool (WT: 2.0 ± 0.1 vesicles, n = 98 boutons; *Epac*^{dKO}:

1.0 ± 0.1 vesicles, n = 127 boutons; $p < 0.0001$) (*Figure 2A*). This difference turned out to be specific to the active zone, as the total number of vesicles in PF terminals (within 100 nm away from active zone) was not affected (WT: 32.8 ± 2.4 vesicles, n = 98 boutons; *Epac*^{dKO}: 28.3 ± 1.5 vesicles, n = 127 boutons; $p = 0.15$). Similarly, the specific deletion of *Prkce* in granule cells also decreased the number of vesicles in the docked vesicle pool (*Prkce*$^{f/f}$: 1.6 ± 0.1 vesicles, n = 60 boutons; *Prkce*^{cKO}: 0.7 ± 0.1 vesicles, n = 66 boutons; $p < 0.0001$) (*Figure 2B*). Meanwhile, the total number of vesicles in PF terminals was also not affected (*Prkce*$^{f/f}$: 42.1 ± 2.3 vesicles, n = 57 boutons; *Prkce*^{cKO}: 39.1 ± 2.6 vesicles, n = 55 boutons; $p = 0.38$). These data demonstrate that both EPAC and PKCε are required for the docking of presynaptic vesicles.

We next examined the effect of the ablation of EPAC or PKCε on synaptic transmission. Miniature excitatory synaptic currents (mEPSCs) at PF-PC synapses were recorded in cerebellar slices from *Math1*-Cre;*Epac1*$^{f/f}$;*Epac2*$^{f/f}$ (*Epac1*^{cKO};*Epac2*^{cKO}) and *Prkce*^{cKO} mice, the former of which caused specific deletion of *Epac1* and *Epac2* in granule cells (*Figure 1–figure supplement 2I-L*), while *Math1*-Cre and *Prkce*$^{f/f}$ mice were used as corresponding controls. We found that mEPSC frequency was reduced in PCs from *Epac1*^{cKO};*Epac2*^{cKO} mice compared to PCs from *Math1*-Cre mice, whereas mean amplitude did not differ between two genotypes (*Figure 2C*). Similarly, the frequency but not the amplitude of mEPSCs was significantly lower in *Prkce*^{cKO} mice than corresponding *Prkce*$^{f/f}$ mice (*Figure 2D*). A decrease in mEPSC frequency may be due to a reduction in release probability (Pr). To determine if Pr is affected following deletion of presynaptic *Epac* and *Prkce*, we used a repeated stimulation protocol to estimate the readily releasable pool (RRP) size as well as Pr. Compared to *Math1*-Cre and *Prkce*$^{f/f}$ mice, repeated stimulation (20 Hz) revealed significant reductions in both RRP and Pr in *Epac1*^{cKO};*Epac2*^{cKO}

(*Figure 2E*) and *Prkce*^{cKO} mice (*Figure 2F*). These results indicate that EPAC or PKCε deficiency reduces Pr of PF-PC synapses, which is in line with the EM experiment demonstrating a reduced number of docked vesicles (*Figure 2A and B*). Overall, these results indicate that the EPAC-PKCε module is essential to presynaptic transmitter release at PF-PC synapses.

We continued to explore how exactly the EPAC-PKCε module modulates synaptic release. An essential process during neurotransmitter release is that Rab3A, RIM1α and Munc13-1 form a tripartite complex and act in concert to dock synaptic vesicles to a release-competent state (*Betz et al., 2001*; *Wang et al., 2001*; *Dulubova et al., 2005*). Thus, we investigated whether the EPAC-PKCε module acts on the Rab3A-RIM1α-Munc13-1 complex. By measuring the ratios of IP/input in co-IP assay of synaptosome extracts, we found that both Munc13-1 and Rab3A had significantly weaker binding ability with RIM1α in both *Epac*^{dKO} (*Figure 2G*) and *Prkce*^{cKO} (*Figure 2H*) synaptosomes, as compared to WT and *Prkce*$^{f/f}$ respectively. In contrast, neither *Epac* nor *Prkce* ablation changed the expression levels of Rab3A and Munc13 (*Figure 2G and H*). These data indicate that the deficiency of either EPAC or PKCε impairs protein interactions in the Rab3A-RIM1α-Munc13-1 complex.

In another set of experiments, we studied whether the EPAC-PKCε module is sufficient to boost protein interactions in the Rab3A-RIM1α-Munc13-1 complex. First, we treated WT synaptosomes with 8-pCPT and εV1-2, and measured the amount of Munc13-1 and Rab3A precipitated with RIM1. The quantification showed a significant increment of precipitated Munc13-1 and Rab3A when synaptosomes were incubated with 8-pCPT (*Figure 2I*). Second, we measured the amounts of precipitated Munc13-1 and Rab3A in WT synaptosomes treated with FR236924, a selective activator of PKCε. We found that precipitations of Munc13-1 and Rab3A

were both increased (*Figure 2J*). These data indicate that either EPAC or PKCε is sufficient to promote the formation of the tripartite complex. In parallel experiments, PKCε inhibitor εV1-2 prevented the increase of precipitated Munc13-1 and Rab3A induced by 8-pCPT (*Figure 2I*), while FR236924 failed to induce more precipitations of Munc13-1 and Rab3A in *Prkce*^{cKO} synaptosomes (*Figure 2K*). In summary, these data demonstrate that the EPAC-PKCε module regulates synaptic organization and transmitter release by regulating the stability of Rab3A-RIM1α-Munc13-1 complex.

Presynaptic PF-PC LTP depends on EPAC and PKCε

Repetitive stimuli of PF terminals result in an increased Pr of neurotransmitters, leading to the expression of presynaptic LTP (*Salin et al., 1996*; *Kimura et al., 1998*; *van Beugen et al., 2013*; *Hirano et al., 2016*; *Kaeser et al., 2008*; *Yang and Calakos, 2010*; *Martín et al., 2020*). If the EPAC-PKCε module determines transmitter release through regulating the phosphorylation level of RIM1α, it is reasonable to hypothesize that this cascade controls presynaptic PF-PC LTP.

To test this hypothesis, presynaptic LTP at PF-PC synapses was induced by a tetanus stimulation (8 Hz for 5 min) at voltage-clamp mode (-70 mV) (*Figure 3A*). The potentiation of EPSCs reached 131 ± 6% of baseline in WT mice (t = 38-40 min; n = 13; $p < 0.001$; *Figure 3B and C*), consistent with previous work (*Salin et al., 1996*; *Kaeser et al., 2008*). Concomitantly, paired-pulse facilitation (PPF) ratio decreased to 84 ± 4% (t = 38-40 min; n = 13; $p < 0.001$; *Figure 3C*), indicating a presynaptic contribution to this form of LTP (*Salin et al., 1996*). Next, we preincubated WT slices with forskolin for 20 min to ensure the effect of forskolin. In this condition, the tetanus stimulation for presynaptic LTP failed to induce synaptic potentiation in PCs

(*Figure 3–figure supplement 1A and B*), indicating that presynaptic LTP at PF-PC synapses occurs upon a rise in the cellular level of cAMP.

Next, we examined presynaptic PF-PC LTP in acute slices from *Epac*^{dKO} and *Epac1*^{cKO};*Epac2*^{cKO} mice. We made whole-cell recordings from PCs and found that 8-Hz stimulation failed to induce potentiation of EPSCs in *Epac*^{dKO} mice (104 ± 5% of baseline at t = 38-40 min; n = 11; p = 0.66) (*Figure 3–figure supplement 1C and D*). This finding was confirmed in recordings from slices of *Epac1*^{cKO};*Epac2*^{cKO} mice, in which *Epac* is deleted from the granule cells innervating the PCs, showing that presynaptic PF-PC LTP was also blocked (93 ± 4% of baseline at t = 38-40 min; n = 9; p = 0.059) (*Figure 3F and G*). In control experiments using *Math1*-Cre mice, the potentiation of EPSCs reached 120 ± 5% of baseline (t = 38-40 min; n = 10; p = 0.004; *Figure 3D and E*). These results indicate that presynaptic EPAC is required for presynaptic LTP.

To find out whether presynaptic PKCε is also required for presynaptic LTP, we recorded 8-Hz stimulation-induced EPSC potentiation in *Prkce*$^{f/f}$ and *Prkce*^{cKO} mice. Similar to WT and *Math1*-Cre mice, the potentiation of PF-EPSCs evoked by 8-Hz stimulation reached 120 ± 3% of baseline in control *Prkce*$^{f/f}$ mice (t = 38-40 min; n = 7; p = 0.004; *Figure 3H and I*). However, presynaptic ablation of PKCε completely blocked the induction of this form of LTP (99 ± 5%; n = 10; p = 0.065; *Figure 3J and K*), suggesting that presynaptic PF-PC LTP also requires PKCε. Here too, the PPF ratio was unaffected (p = 0.77 at t = 38-40 min; n = 10; *Figure 3K*). This conclusion was further confirmed following chemical inhibition of PKCε by continuously administering εV1-2 to cerebellar slices from WT mice, as εV1-2 completely blocked the induction of presynaptic PF-PC LTP (101 ± 4%; n = 9; p = 0.59; *Figure 3–figure supplement 1E and F*).

On the basis of our experiments in PCs from mice with presynaptic specific deletion of EPAC and PKCε, we conclude that the presynaptic EPAC-PKCε module is critical for presynaptic PF-PC LTP in the cerebellum.

EPAC and PKCε mediate cAMP-triggered EPSC potentiation

cAMP is also required for presynaptic LTP induced by electrical stimulation (*Salin et al., 1996*; *Le Guen and De Zeeuw, 2010*), and its agonists are enough to produce a prominent increase in glutamate release (*Weisskopf et al., 1994*; *Salin et al., 1996*). However, it remains unclear which downstream effector, EPAC or PKA (*Cheng et al., 2008*), is responsible for cAMP-induced potentiation. In particular, the central role of PKA in presynaptic LTP has been argued by studies showing that presynaptic LTP can still be intact when serine phosphorylation of RIM1 by PKA is interrupted (*Kaeser et al., 2008*; *Yang and Calakos, 2010*; also see *Lonart et al., 2003*). Therefore, we investigated whether the EPAC-PKCε module mediates cAMP-triggered EPSC potentiation.

We made whole-cell recordings from PCs and evoked PF-EPSCs every 30s in *Math1*-Cre, *Epac1*^{cKO};*Epac2*^{cKO} and *Prkce*^{cKO} mice. In *Math1*-Cre control mice, external application of forskolin produced a long-lasting elevation in PF-EPSC amplitude (*Figure 4A and B*), with a peak potentiation of 366 ± 25% (at 48-50 min; n = 15; *Figure 4C*). In contrast, simultaneous ablation of *Epac1* and *Epac2* at presynaptic sites prominently affected the synaptic potentiation induced by forskolin application (162 ± 18% at 48-50 min; n = 12; *Figure 4A-C*). Next, we incubated *Epac1*^{cKO};*Epac2*^{cKO} PCs along with PKA antagonist KT5720 and again examined forskolin-induced EPSC potentiation. In this case, we found that combined blockade of EPAC and PKA completely eliminated the action of forskolin on EPSC potentiation (106 ± 4% at 48-50 min;

255 n = 12; *Figure 4A-C*). We continued to examine the effect of PKCε on cAMP-triggered EPSC
256 potentiation using *Prkce*^{cKO} mice. Similar to *Epac1*^{cKO};*Epac2*^{cKO} mice, the forskolin-induced
257 potentiation in *Prkce*^{cKO} PCs was significantly attenuated (198 ± 5% at 48-50 min; n = 12; *Figure*
258 *4A-C*). Again, the remaining potentiation was further blocked by the addition of KT5720 (101 ± 3%
259 at 48-50 min; n = 12; *Figure 4A-C*). Thus, these results indicate that EPAC, PKCε and PKA all
260 mediate cAMP-induced potentiation of transmitter release. In parallel with the observation of
261 EPSC amplitude, PPF was monitored during the whole cell recordings. Forskolin application led
262 to a significant reduction in PPF ratio of PF-EPSCs in *Math1*-Cre mice (*Figure 4C*). However, this
263 reduction was significantly less when presynaptic of both types of EPAC as well as PKCε were
264 ablated and KT5720 was added (*Figure 4C*), further highlighting that EPAC and PKCε work
265 synergically on the synaptic release at PF-PC synapses.

266 We next assessed the impact of the EPAC-PKCε module on the strength of PF-EPSCs by
267 directly applying EPAC agonist 8-pCPT. In line with previous work (*Kaneko and Takahashi, 2004*;
268 *Gekel and Neher, 2008*), the administration of 8-pCPT was sufficient to potentiate PF-EPSCs by
269 179 ± 18% and reduce their PPF ratio by 17 ± 3 % in WT PCs (n = 6; at 18-20 min) (*Figure 4D*).
270 Two lines of evidence confirm that the potentiation of PF-EPSCs by EPAC is mediated by PKCε.
271 First, 8-pCPT-induced potentiation of PF-EPSCs was diminished in *Prkce*^{cKO} mice, as shown by
272 unchanged PF-EPSCs and PPF (*Figure 4E*). Second, co-application of εV1-2 effectively prevented
273 the 8-pCPT-induced synaptic potentiation and change in PPF (*Figure 4F*).

274 In summary, we conclude that EPAC-PKCε module and PKA are both downstream effectors
275 of cAMP, but the EPAC-PKCε module plays the most prominent role in cAMP-triggered EPSC
276 potentiation.

Presynaptic EPAC and PKCε are not involved in postsynaptic forms of plasticity

The mechanisms for postsynaptic LTP and LTD at PF-PC synapses can be complicated, in that they may depend not only on postsynaptic processes, but sometimes also on presynaptic events (*Le Guen and De Zeeuw, 2010*; *Wang et al., 2014*; *Schonewille et al., 2021*). For example, an endocannabinoid-triggered reduction of synaptic release is required by the induction of postsynaptic LTD (*Kreitzer et al., 2002*). As both EPAC and PKCε regulate Pr of PF-PC synapses, we wondered whether the EPAC-PKCε module also regulates postsynaptic LTP and LTD.

After acquiring stable EPSCs in voltage-clamp mode (-70 mV), we induced postsynaptic LTP by stimulating PFs at 1 Hz for 5 min in current-clamp mode (*Figure 5A*). In WT mice, this tetanus stimulation induced an increase of PF-EPSCs (131 ± 5% of baseline at t = 38-40 min; $n = 13$; $p < 0.001$) (*Figure 5B and C*), while PPF was not changed (*Figure 5D*). When this protocol was applied at PF-PC synapses in *Epac*^{dKO} mice, we did not find any sign of potentiation of PF-EPSCs (106 ± 6% of baseline at t = 38-40 min; $n = 13$; $p = 0.26$) (*Figure 5B-D*). While these results were consistent with our previous observation that EPAC is required for postsynaptic LTP (*Gutierrez-Castellanos et al., 2017*), we had yet to specify the cellular site of action for EPAC. Therefore, we repeated the induction protocol for postsynaptic LTP in *Math1*-Cre and *Epac1*^{cKO};*Epac2*^{cKO} mice. In this case, the protocol successfully induced PF-PC LTP in both types of mice (*Figure 5E and F*), while PPF was not altered (*Figure 5G*), suggesting that this is a postsynaptic form of LTP. We continued to examine the expression of postsynaptic PF-PC LTP in *Prkce*$^{f/f}$ and *Prkce*^{cKO} mice. Similar to *Epac1*^{cKO};*Epac2*^{cKO} mice, *Prkce*$^{f/f}$ and *Prkce*^{cKO} PCs exhibited robust PF-PC LTP when 1 Hz stimulation was delivered to PFs (*Figure 5H and I*) with

unaltered PPF (*Figure 5J*), confirming the postsynaptic site of LTP.

Next, we investigated whether the expression of postsynaptic PF-PC LTD is affected by ablation of EPAC and PKCε. PF-PC LTD was induced by giving repetitive PF stimulation at 100 Hz for 100 ms paired with a depolarization of the PCs involved (*Figure 6A*) (*Steinberg et al., 2006*; *Zhou et al., 2015*). As shown by example responses (*Figure 6B*), *Epac*^{dKO} PCs showed robust PF-PC LTD (t = 38-40 min: 59 ± 4% of baseline; n = 13; *Figure 6C*), while the PPF ratio was not changed (p = 0.26 at t = 38-40 min; n = 13; *Figure 6D*). Likewise, PF-PC LTD could be successfully induced in *Math1*-Cre and *Epac1*^{cKO};*Epac2*^{cKO} mice (*Figure 6E and F*), while PPF was not altered (*Figure 6G*). Moreover, we found that the same protocol could induce PF-PC LTD in *Prkce*$^{f/f}$ and *Prkce*^{cKO} mice (*Figure 6H and I*) without affecting PPF (*Figure 6J*).

Overall, our results suggest that presynaptic EPAC and PKCε are not required for the induction of postsynaptic forms of LTP and LTD.

The EPAC-PKCε module is essential for motor performance and motor learning

Even though plastic changes in the granular layer of the cerebellum have been suggested to contribute to procedural memory formation (*Le Guen and De Zeeuw, 2010*), the evidence thus far is limited (*Andreescu et al., 2011*; *Galliano et al., 2013*). Therefore, we investigated whether the EPAC-PKCε module, which is critical to presynaptic PF-PC LTP, contributes to performance and adaptation of compensatory eye movements mediated by the vestibulo-cerebellum (*Schonewille et al., 2010*; *Grasselli et al., 2020*).

Basic performance parameters included amplitude (gain) and timing (phase) of the optokinetic response (OKR), vestibulo-ocular reflex (VOR), and visually enhanced VOR (VVOR)

(*Figure 7A*). We found that basic motor performance was impaired in *Epac*^{dKO} mice in that they showed significant deficits in the amplitude and timing of their OKR (p = 0.009 and p = 0.004, respectively; ANOVA for repeated measurements) and VOR (p = 0.001 and p = 0.02, respectively; ANOVA for repeated measurements) (*Figure 7–figure supplement 1A and B*). In contrast, no significant differences were observed in the VVOR (p = 0.66 and p = 0.68 for gain and phase values, respectively; *Figure 7–figure supplement 1C*).

The same compensatory eye movements were also tested in *Epac1*^{cKO};*Epac2*^{cKO} and *Prkce*^{cKO} mice as well as their littermate controls. Basic eye movement performance was also affected in *Epac1*^{cKO};*Epac2*^{cKO} mice in that their OKR gains were significantly lower than those of *Math1*-Cre littermates (p = 0.003; ANOVA for repeated measurements) (*Figure 7B*), that their VOR gains were significantly greater than those of *Math1*-Cre littermates (VOR: p = 0.027; ANOVA for repeated measurements) (*Figure 7C*), and that the phase values during both OKR and VOR were significantly lagging those of the *Math1*-Cre littermates (OKR: p = 0.001; VOR: p = 0.047; ANOVA for repeated measurements) (*Figure 7B and C*). No significant differences were observed between *Epac1*^{cKO};*Epac2*^{cKO} and *Math1*-Cre mice in the VVOR (p = 0.69 and p = 0.75 for gain and phase values, respectively) (*Figure 7D*). Moreover, *Prkce*^{cKO} mice shared the same defects with *Epac1*^{cKO};*Epac2*^{cKO} mice in their basic motor performance. OKR gain values of *Prkce*^{cKO} mice were significantly lower than those of *Prkce*$^{f/f}$ littermates (p = 0.013; ANOVA for repeated measurements) (*Figure 7E*), whereas their VOR gain values were greater than those of control littermates (p = 0.034; ANOVA for repeated measurements) (*Figure 7F*). Meanwhile, OKR and VOR phase values of *Prkce*^{cKO} mice were both significantly lagging those of the *Math1*-Cre littermates (OKR: p = 0.015; VOR: p = 0.044; ANOVA for repeated measurements) (*Figure 7E*

343 *and F*). No significant differences were observed between *Prkce*$^{f/f}$ and *Prkce*^{cKO} mice in the
344 VVOR (p = 0.93 and p = 0.50 for gain and phase values, respectively) (*Figure 7G*). Altogether,
345 our data suggest that presynaptic ablation of EPAC and/or PKCε mice profoundly influences
346 motor performance when visual and vestibular systems are separated, but not when they are
347 engaged simultaneously, as occurs under natural conditions or during visuo-vestibular training.

348 Next, we tested the VOR phase-reversal protocol, which is considered the type of motor
349 learning sensitive to the perturbation to the vestibulo-cerebellum (*Wulff et al., 2009*; *Badura et al.,*
350 *2016*; *Peter et al., 2016*). VOR phase reversal aims to reverse the direction of the VOR using
351 retinal slip caused by a screen rotation in the same direction (i.e., in phase) as head rotation and
352 with increasing amplitude as the training progresses (*Figure 7H*). During the initial days of
353 gain-decrease training, all three control mouse lines (WT, *Math1*-Cre and *Prkce*$^{f/f}$) exhibited gain
354 reductions similar to previous work (*Wulff et al., 2009*; *Badura et al., 2016*; *Gutierrez-Castellanos*
355 *et al., 2017*). Gain reductions were smaller in *Epac*^{dKO} (*Figure 7–figure supplement 1D*),
356 *Epac1*^{cKO};*Epac2*^{cKO} (*Figure 7I*), as well as *Prkce*^{cKO} (*Figure 7J*) mice, but the deficit varied across
357 days between the different mouse lines (in *Epac*^{dKO} mice, Day 1: p = 0.043; Day 2: p = 0.008; Day
358 3: p = 0.002; Day 4: p = 0.007; Day 5: p = 0.004; in *Epac1*^{cKO};*Epac2*^{cKO} mice, Day 1: p = 0.079;
359 Day 2: p = 0.036; Day 3: p = 0.011; Day 4: p = 0.22; Day 5: p = 0.061; and in *Prkce*^{cKO} mice, Day
360 1: p = 0.047; Day 2: p = 0.004; Day 3: p = 0.004; Day 4: p = 0.084; Day 5: p = 0.15). WT (*Figure*
361 *7–figure supplement 1D*), *Math1*-Cre (*Figure 7I*) as well as *Prkce*$^{f/f}$ (*Figure 7J*) mice showed a
362 proper reversal of the phase of their VOR, highlighting their ability to invert the direction of an
363 innate reflex (*Wulff et al., 2009*; *Badura et al., 2016*; *Peter et al., 2016*; *Grasselli et al., 2020*).
364 Whereas the VOR phase values were not significantly affected in the *Epac*^{dKO},

365 *Epac1*^{cKO};*Epac2*^{cKO}, and *Prkce*^{cKO} mouse lines during the first day (WT versus *Epac*^{dKO}, $p = 0.15$;

366 *Math1*-Cre versus *Epac1*^{cKO};*Epac2*^{cKO}, $p = 0.087$; *Prkce*$^{f/f}$ versus *Prkce*^{cKO}, $p = 0.52$), they were so

367 during sessions on days 2-5 (WT versus *Epac*^{dKO}: Day 2, $p = 0.003$; Day 3, $p = 0.002$; Day 4, $p <$

368 0.001; Day 5, $p < 0.001$; *Math1*-Cre versus *Epac1*^{cKO};*Epac2*^{cKO}: Day 2, $p < 0.001$; Day 3, $p <$

369 0.001; Day 4, $p < 0.001$; Day 5, $p < 0.001$; *Prkce*$^{f/f}$ versus *Prkce*^{cKO}: Day 2, $p = 0.01$; Day 3, $p =$

370 0.048; Day 4, $p < 0.001$; Day 5, $p < 0.001$). Therefore, we conclude that *Epac*^{dKO},

371 *Epac1*^{cKO};*Epac2*^{cKO} and *Prkce*^{cKO} mice had prominent deficits in phase-reversal learning of their

372 VOR.

Discussion

In the current study we demonstrate that triggering EPAC induces PKCε activation and threonine phosphorylation of RIM1α, which in turn facilitates the assembly of the Rab3A-RIM1α-Munc13-1 tripartite complex and thereby docking and release of synaptic vesicles at active zones of PF-PC synapses (*Figure 7–figure supplement 2*). The form of presynaptic LTP at these synapses that requires activation of the EPAC-PKCε module can be induced by either tetanic stimulation or forskolin at PF terminals (*Figure 7–figure supplement 2*). Via its presynaptic actions, the EPAC-PKCε module contributes to adaptation of compensatory eye movements, a motor learning task that depends on the vestibule-cerebellum.

Threonine phosphorylation of RIM1α by the EPAC-PKCε module

Our finding that the EPAC-PKCε module can phosphorylate RIM1α raises a simple but fascinating mechanistic concept that the phosphorylation level of RIM1α determines presynaptic release. RIM1α specifically interacts with a number of presynaptic proteins, such as Munc13-1, liprin-α and ELKS, so as to form a scaffold complex regulating homeostatic release of synaptic vesicles (*Südhof, 2004*). RIM1α can be phosphorylated at two serine residues by PKA and CaMKII (*Lonart et al., 2003*; *Sun et al., 2003*), which promotes its interaction with 14-3-3 protein (*Sun et al., 2003*). The current work advances on this concept by showing that RIM1α can also be phosphorylated at its threonine sites by PKCε. Moreover, our data demonstrate the functional implication consequence of threonine phosphorylation of RIM1α at PF-PC synapses: it promotes the assembly of the Rab3A-RIM1α-Munc13-1 complex and is essential for the induction of presynaptic PF-PC LTP, suggesting that a fast switch between phosphorylation and

dephosphorylation of RIM1α may regulate presynaptic potentials during dynamic synaptic events. This new mechanistic concept is in line with the notion that synaptic vesicle proteins, such as RIM1α, often exhibit stimulation-dependent changes in phosphorylation (*Kohansal-Nodehi et al., 2016*). It remains to be elucidated how threonine and serine phosphorylations of RIM1α may exert distinct downstream effects. For instance, one could speculate that the threonine loci of RIM1α lead to more prominent conformational changes, allowing RIM1α to bind to active zone proteins.

Distinct roles of EPAC and PKA at synapses

cAMP-mediated signaling pathways that are mediated by EPAC and PKA regulate a multitude of physiological and pathological processes (*Cheng et al., 2008*). EPAC shares homologous cAMP-binding domains with PKA, but also possesses domains absent in PKA, such as the Ras exchange motif, the Ras association domain, and the CDC25-homology domain (*Cheng et al., 2008*). Indeed, the specific domains endow EPAC and PKA with different and even opposite functions. For example, in contrast to PKA, EPAC can activate small GTPase Rap1 (*de Rooij et al., 1998*) and increase PKB phosphorylation (*Mei et al., 2002*). Our current work bolsters the differences, showing that EPAC can phosphorylate PKCε and RIM1α threonine sites at synapses. This highlights the question as to how EPAC and PKA operate in an integrated manner to control the net physiological effect of cAMP-signaling pathways at synapses. Some studies indicate that presynaptic potentiation depends predominantly on PKA (*Salin et al., 1996*; *Linden and Ahn, 1999*; *Lev-Ram et al., 2002*), whereas others advocate a more critical role for EPAC *(Kaneko and Takahashi, 2004*; *Fernandes et al., 2015*; *Martín et al., 2020*). Our results highlight that ablation of either EPAC or PKCε by itself is not sufficient to block forskolin-induced synaptic potentiation,

417 but that supplementing this with a blockage of PKA causes a complete blockage. These results
418 demonstrate that EPAC and PKA can conjunctively regulate synaptic potentiation. Even so, our
419 results clarify that the impact of EPAC on cAMP-induced EPSC potentiation is dominant, as it has
420 the strongest contribution to the forskolin-induced increase of EPSC amplitude. Alternatively,
421 PKA warrants a minimum level of potentiation that may be required under particular
422 circumstances when EPAC is not active.
423
424 **The EPAC-PKCε module is required for synaptic release and presynaptic LTP**
425 Our EM analysis shows that the number of docked vesicles at the PF terminals of *Epac*^{dKO} and
426 *Prkce*^{cKO} mutants is reduced, whereas the general structure of PF-PC synapses is unchanged. As
427 the ablation of either EPAC or PKCε attenuated protein interactions in the
428 Rab3A-RIM1α-Munc13-1 complex, which is required for the docking and priming of presynaptic
429 vesicles (*Schoch et al. 2002*; *Südhof, 2004*; *Ferrero et al., 2013*), the reduction in docked vesicles
430 in *Epac*^{dKO} and *Prkce*^{cKO} mice can be readily explained. In parallel with our observations at the
431 ultrastructural level, we found that mice with presynaptic deletion of *Epac* and *Prkce*^{cKO} displayed
432 obvious defects in synaptic release at the electrophysiological level. Although EPAC1 and EPAC2
433 have been shown to be involved in synaptic release in the hippocampus and cerebellum (*Yang et*
434 *al., 2012*; *Zhao et al., 2013*; *Martín et al., 2020*), our finding that PKCε acts as the downstream
435 effector of EPAC and regulates presynaptic release is novel. Furthermore, we demonstrate for the
436 first time that presynaptic PKCε is required for presynaptic LTP at PF-PC synapses. These
437 findings expand the repertoire of forms of PC plasticity that are driven by cAMP signaling.
438 The role of the cAMP-PKA cascade in presynaptic LTP has been extensively debated. Early

studies claimed that PKA and RIM1α serine phosphorylation are critical for the induction of presynaptic LTP at PF-PC synapses (*Salin et al., 1996*; *Lonart et al., 2003*). However, this conclusion was challenged by follow-up studies, demonstrating that RIM1α S413A mutant mice exhibit normal presynaptic LTP in both cerebellum and hippocampus (*Kaeser et al., 2008*; *Yang and Calakos, 2010*). In our opinion, a couple of caveats must be considered regarding the function of PKA in presynaptic LTP. First, cAMP analogs (Rp-8-CPT-cAMP-S and Sp-8CPT-cAMP-S) used in two studies advocating that PKA mediates presynaptic PF-PC LTP (*Salin et al., 1996*; *Lonart et al., 2003*) are able to regulate Rap1 (*Roscioni et al., 2009*), which is a direct substrate of EPAC (*de Rooij et al., 1998*). Therefore, these cAMP analogs may also act through the EPAC-PKCε module. Second, KT5720 at 10 μm, a concentration used by Lonart et al. (*Lonart et al., 2003*), can alter a range of protein kinases, including phosphorylase kinase, mitogen-activated protein kinase kinase, PKBα, glycogen synthase kinase 3β, as well as AMP-activated protein kinase (*Brushia and Walsh, 1999*; *Davies et al., 2000*; *Murray, 2008*). Thus, KT5720 at this concentration has numerous side-effects next to its ability to inhibit PKA. In contrast, our results derived from cell-specific mouse lines consistently converge on the concept that presynaptic PF-PC LTP depends on the EPAC-PKCε module. More specifically, our data demonstrate that repetitive 8-Hz PF stimulation increases the level of cAMP and consequently activates EPAC and PKCε, which in turn induces threonine phosphorylation of RIM1α, suggesting a phospho-switch machinery that can tune presynaptic PF-PC LTP.

Our finding that the EPAC-PKCε module is a central component for synaptic release and presynaptic LTP may not stand on its own. In fact, EPAC is involved in cellular processes like cell adhesion, cell-cell junction formation, exocytosis and secretion, cell differentiation, as well as cell

proliferation (*Cheng et al., 2008*), while PKCε is necessary for sperm exocytosis in the testis (*Lucchesi et al., 2016*). Together, these lines of evidence suggest that the EPAC-PKCε module might be a widespread mechanism controlling not only synaptic release in nerve cells, but also granule secretion in endocrine or proliferating cells.

Role of presynaptic LTP in motor behavior

Many studies have explored the potential functional role of postsynaptic plasticity at PC synapses, in particular that of PF-PC LTP and PF-PC LTD (*Gao et al., 2012*; *Raymond and Medina, 2018*). The picture emerging from these studies is that postsynaptic PF-PC LTP and PF-PC LTD play an important role in forms of learning that are mediated by the so-called upbound and downbound modules (*De Zeeuw, 2021*). Whereas VOR adaptation is mainly mediated by upbound microzones in the vestibulo-cerebellum that increase the simple spike frequency during learning (*Gutierrez-Castellanos et al., 2017*; *Voges et al., 2017*), eyeblink conditioning is predominantly regulated by downbound microzones in lobule simplex that decrease simple spikes during learning (*Ten Brinke et al., 2015*; *Wu et al., 2019*). Yet, what is the role of presynaptic LTP at PF to PC synapses? Even though it has been suggested more than a decade ago that the functional role of presynaptic plasticity at PF-PC synapses during learning can be expected to align with that of postsynaptic plasticity (*Le Guen and De Zeeuw, 2010*), evidence has been largely lacking.

Here, we found that *Epac1*^{cKO};*Epac2*^{cKO} and *Prkce*^{cKO} mice, which showed reduced PF-PC transmission and lack presynaptic LTP, exhibit deficits in basic motor performance, in the form of an affected OKR and VOR, as well as in gain-decrease and phase reversal learning of their VOR (*Figure 7–figure supplement 2*). Similarly, presynaptic ablation of EPACs or PKCε results in

483 altered gain and phase values of their OKR and VOR. Interestingly, the impairments in OKR and
484 VOR caused by deletion of *Epac1/Epac2* or *Prkce* in granule cells were similar to those caused by
485 global deletion of *Epac*. This finding raises the possibility that presynaptic EPAC is in fact more
486 critical for basic motor performance than postsynaptic EPAC. This possibility is compatible with
487 previous work showing that mice with a PC-specific deletion of GluA3, which leads to a lack of
488 postsynaptic LTP mediated by EPAC, have hardly any significant deficit in basic motor
489 performance (*Gutierrez-Castellanos et al., 2017*). By the same argument, the contribution of
490 presynaptic LTP to phase reversal learning might be more in line with that of postsynaptic PF-PC
491 LTP in that *Epac1*^{cKO};*Epac2*^{cKO} and *Prkce*^{cKO} mice showed similar deficits as PC-specific GluA3
492 knockouts. The prediction that the impact of presynaptic plasticity at PF-PC synapses during
493 learning operates in a synergistic fashion with that of postsynaptic plasticity (*Le Guen and De*
494 *Zeeuw, 2010*), does in this respect hold.

Materials and Methods

Animals

Original breeding pairs of *Epac*^{dKO} and *Math1*-Cre mice were obtained from Youmin Lu (Huazhong University of Science and Technology, Wuhan, China) and Wei Mo (Xiamen University, Xiamen, China), respectively. *Epac1*$^{f/f}$, *Epac2*$^{f/f}$ and *Prkce*$^{f/f}$ mice were made by us with the assistance of GemPharmatech (Soochow, Jiangsu, China) and Nanjing Biomedical Research Institute (Nanjing, Jiangsu, China). The resulting offspring were genotyped using PCR of genomic DNA. Mice were kept at the Experimental Animal Center of Zhejiang University under temperature-controlled condition on a 12:12 h light/dark cycle. All experiments were performed blind to genotypes in age-matched littermates of either sex.

Antibodies and Reagents

Antibodies against RIM1 (Cat# 140013, RRID:AB_2238250 and Cat# 140023, RRID:AB_2177807), Rab3 (Cat# 107011, RRID:AB_887768) and Munc13-1 (Cat# 126102, RRID:AB_887734) were from Synaptic Systems (Gottingen, Germany). Antibodies against phosphor-threonine (Cat# 9381, RRID:AB_330301), EPAC1 (Cat# 4155, RRID:AB_1903962) and EPAC2 (Cat# 4156, RRID:AB_1904112) were from Cell Signaling (Danvers, MA). The antibody to phosphor-serine (Cat# AB1603, RRID:AB_390205) was from Millipore (Billerica, MA). Antibodies against HA (Cat# M20003, RRID:AB_2864345), Flag (Cat# M20008, RRID:AB_2713960) and His (Cat# M30111, RRID:AB_2889874) were from Abmart (Shanghai, China). Antibody against PKCα (Cat# P4334, RRID:AB_477345) was from sigma (St. Louis, MO). Antibodies against PKCα-pS657 (ab23513, RRID:AB_2237450), PKCα-pT638 (Cat#

ab32502, RRID:AB_777295), PKCε-pSer729 (Cat# ab63387, RRID:AB_1142277), EPAC1 (Cat# ab21236, RRID:AB_2177464, for immunostaining), EPAC2 (Cat# ab124189, RRID:AB_10974926, for immunostaining), anti-mouse IgG for IP (HRP) (Cat# ab131368, RRID:AB_2895114) and VeriBlot for IP Detection Reagent (HRP) (Cat# ab131366, RRID:AB_2892718) were from Abcam (Cambridge, UK). Antibody against β-tubulin (Cat# sc-5274, RRID:AB_2288090) was from Santa Cruz (Dallas, TX). Antibody against PKCε (Cat# MA5-14908, RRID:AB_10985232), Goat anti-mouse IgG horseradish peroxidase (HRP)-conjugated (Cat# 31446, RRID:AB_228318), Goat anti-rabbit IgG horseradish peroxidase (HRP)-conjugated (Cat# 31460, RRID:AB_228341) were from Thermo Fisher Scientific (Waltham, MA). Anti-vGluT1 antibody was a gift from Dr. Masahiko Watanabe (Hokkaido University, Sapporo, Japan). The antibody against PKCε (Cat# 20877-1-AP, RRID:AB_10697812, for immunostaining) was from Proteintech (Rosemont, IL). Mouse IgG (Cat# A7028, RRID:AB_2909433) and rabbit IgG (Cat# A7016, RRID:AB_2905533) were from Beyotime (Shanghai, China). Protease inhibitor cocktail (04693132001) was from Roche (Mannheim, Germany). Gö6976 (2253), 8-pCPT (4853) and FR236924 (3091) were from Tocris (Bristol, UK). Dulbecco's modified Eagle's medium (DMEM, 11885-084), Penicillin-Streptomycin (15140-122), Sodium Pyruvate (11360-070), Fetal Bovine Serum (FBS, 10099-133), lipofectamine 2000 (11668-019), OPTI-MEM (31985-062), and Alexa Fluor-conjugated secondary antibodies were from Invitrogen (Carlsbad, CA). GammaBind Plus Sepharose (17-0886-01) was from GE healthcare. Other chemicals were from Sigma (St. Louis, MO) unless stated otherwise.

Plasmid construction

539 The construction of plasmids was performed according to previous work (*Wang et al., 2015*).
540 HA-RIM1α, Flag-EPAC1, Flag-EPAC2, and His-PKCε, were constructed based on the coding
541 sequence of rat *RIM1α* gene (GenBank# NM_052829.1), rat *EPAC1* gene (GenBank#
542 NM_021690.1), rat *EPAC2* gene (GenBank# XM_017592164.1), and rat *Prkce* gene (GenBank#
543 NM_017171.1), respectively. All constructs were verified by DNA sequencing.
544
545 **RT-PCR**
546 RT-PCR was used to determine the mRNA level of EPAC1, EPAC2 and PKCε in granule cells.
547 The contents of individual granule cells (P21) were harvested as described in previous work (*Zhou*
548 *et al., 2017*). The harvested contents were subjected to RT-PCR using OneStep Kit (210212,
549 Qiagen, Hilden, Germany). Forward (F) and reverse (R) primers used for amplification were as
550 follows: *Epac1*, F: 5'- GCT TGT TGA GGC TAT GGC-3'; R: 5'- ACA CAG TTC CTG CCT
551 TGC-3'. *Epac2*, F: 5'- CAT TCT CTC TCG AGC TCC-3'; R: 5' TGG TTG AGG ACA CCA
552 TCT-3'. *Prkce*, F: 5'- ATT GAC CTG GAG CCA GAA -3'; R: 5'- CTT GTG GCC ATT GAC
553 CTG-3'. *Gapdh*, F: 5'-GGT GAA GGT CGG TGT GAA CG-3'; R: 5'-CTC GCT CCT GGA AGA
554 TGG TG-3'.
555
556 **HEK cell culture**
557 HEK cells were cultured in DMEM supplemented with 10% FBS, 1 mM sodium pyruvate, 100
558 U/ml penicillin, and 10 μg/ml streptomycin and stored in an incubator (95% O_2/5% CO_2; 37°C).
559 The plasmids were transfected to HEK cells in OPTI-MEM using lipofectamine 2000 (Invitrogen)
560 at 70-80% confluency.

561

562 **Purification of synaptosomes**

563 Synaptosomes were purified according to previous work (*Ferrero et al., 2013*). Cerebellar tissues
564 from mice (P21) were homogenized in a medium (pH7.4) containing sucrose (320 mM) and
565 protease inhibitors. The homogenate was centrifuged 2,000× *g* (4°C for 2 min) and the supernatant
566 was spun again at 9,500× *g* (4°C for 12 min). The compacted white layer containing the majority
567 of synaptosomes was gently resuspended in sucrose (320 mM) supplemented with protease
568 inhibitors, and an aliquot of synaptosomal suspension (2 ml) was placed onto a 3-ml Percoll
569 discontinuous gradient (GE Healthcare) containing (in mM) 320 sucrose, 1 EDTA, 0.25
570 DL-dithiothreitol, and 3, 10, or 23% Percoll. After centrifugation at 25,000× *g* (4°C for 10 min),
571 synaptosomes were recovered from between 10% and 23% bands and diluted in a medium (in mM)
572 (140 NaCl, 5 KCl, 5 $NaHCO_3$, 1.2 NaH_2PO_4, 1 $MgCl_2$, 10 glucose, 10 HEPES; pH 7.4)
573 supplemented with protease inhibitors. The synaptosomes good for experiments were harvested
574 from the pellet after the final centrifugation at 22,000× *g* (4°C for 10 min).

575

576 **Immunocytochemistry**

577 For immunocytochemistry, synaptosomes were added to a medium containing 0.32 M sucrose (pH
578 7.4), allowed to attach to polylysine-coated coverslips for 1 h, and fixed for 10 min in 4%
579 paraformaldehyde in 0.1 M phosphate buffer (PB) (pH 7.4) at room temperature. Following
580 several washes with PB (pH 7.4), synaptosomes were incubated for 1 h in 10% normal goat serum
581 diluted in PBS (pH 7.4) containing 0.2% Triton X-100. Subsequently, they were incubated for 24
582 h with primary antiserum for EPAC1 (1:500), EPAC2 (1:500), PKCε (1:500) and vGluT1 (1:500).

After washing in PBS, synaptosomes were incubated with secondary antibodies for 2 h. Coverslips were mounted with Prolong Antifade Kit (Molecular Probes) and synaptosomes were viewed using a confocal microscope (Nikon A1R) with a ×100 objective.

Co-immunoprecipitation

After measuring protein concentration using the BCA assay, a tenth of lysis supernatant derived from synaptosomes or cultured cells was used for input and the remainder were incubated with anti-RIM1 or anti-HA antibody, which was precoupled to GammaBind Plus Sepharose at 5-10 μg antibody/1 ml beads for 3 h. Proteins on the beads were extracted with 2× SDS sample buffer plus protease inhibitors and boiled for 5 min before Western blot.

Western blotting

The protein concentration was determined using BCA protein assay. Equal quantities of proteins were loaded and fractionated on SDS-PAGE, transferred to PVDF membrane (Immobilon-P, Millipore), immunoblotted with antibodies, and visualized by enhanced chemiluminescence (Thermo). The dilutions of primary antibodies were 1:1,000 for RIM1, Munc13-1, PKCα-pS657, EPAC1, EPAC2, p-Thr, p-Ser, β-tubulin, and PKCε-pSer729; 1:2,000 for Rab3A and PKCε; 1:5,000 for PKCα-pT638; 1:10,000 for HA, His, Flag, GAPDH, and PKCα. Secondary antibodies were goat anti-rabbit (1:10,000), goat anti-mouse (1:10,000), anti-mouse IgG for IP (HRP) (1:1,000), VeriBlot for IP Detection Reagent (HRP) (1:1,000). Film signals were digitally scanned and quantified using ImageJ 1.42q (NIH, Bethesda, MD).

Electron microscopy

After anesthetic mice (P21) were transcardially perfused with saline and ice-cold fixative, brains were removed and stored at 4°C for 2.5 h in fixative. Sagittal slices of vermis (200 μm) were prepared and rectangular molecular layer sections from lobules IV-V were dissected. The samples were dehydrated and embedded in an epoxy resin. Ultrathin sections (90 nm) were cut using an ultra-microtome (Leica), stained with 2% uranyl acetate and lead solution, and mounted on grids. EM images were captured at 30,000× magnification using a Tecnai transmission electron microscope (FEI, Hillsboro, OR). PF-PC synapses were identified by asymmetrical and short contacts, which were distinct from GABAergic or climbing fiber synapses (*Ichikawa et al., 2016*). ImageJ was used to count the numbers of total and docked vesicles per bouton.

Golgi staining and spine density analysis

Golgi staining was performed using Rapid Golgi Stain Kit (FD NeuroTech Inc., Ellicott, MD) according to the manufactory's instruction. PCs at the apical region were imaged using a bright field microscope (Zeiss, Germany). ImageJ was used to count the spine number and dendrites length of PCs with manual assistant.

Electrophysiology

Sagittal slices of cerebellar vermis (250 μm) were prepared from anesthetic mice (P21) using a vibrating tissue slicer (Leica VT1000S) and ice-cold standard artificial cerebrospinal fluid (aCSF) containing (in mM): 125 NaCl, 2.5 KCl, 1.25 NaH_2PO_4, 1 $MgCl_2$, 2 $CaCl_2$, 26 $NaHCO_3$ and 25 D-glucose, bubbled with 95% O_2/5% CO_2. After recovery for 30 min at 37°C, slices were placed

in a submerged chamber that was perfused at 2 ml/min with aCSF supplemented with GABAzine (10 μM) during recordings.

PCs were visualized under an upright microscope (BX51, Olympus) equipped with a 40× water-immersion objective and infrared differential interference contrast enhancement. Whole-cell recordings were made on PCs from lobules IV-V with a MultiClamp 700B amplifier (Molecular Devices). Currents were digitized at 10 kHz and filtered at 3 kHz. Patch electrodes (3-5 MΩ) were filled with an intracellular solution containing (in mM) 135 Cs-methanesulfonate, 10 CsCl, 10 HEPES, 0.2 EGTA, 4 Na_2ATP, and 0.4 Na_3GTP (pH 7.3, OSM 290). PCs were held at -70 mV to prevent spontaneous spikes that might escape clamp. For PF stimulation, standard patch pipettes were filled with aCSF and placed in middle third of molecular layer. Presynaptic PF-PC LTP was induced by stimulating PF input 120 times at 8 Hz (*Salin et al., 1996*; *Kaeser et al., 2008*). Postsynaptic PF-PC LTP was obtained when PFs were stimulated at 1 Hz for 5 min in parallel with current-clamp of recording PC (*Wang et al., 2014*). PF-LTD was induced by a conjunction of 5 PF-pulses at 100 Hz and a 100-ms long depolarization of PC to 0 mV, which was repeated 30 times with an interval of 2 s (*Zhou et al., 2015*). mEPSCs were recorded in whole-cell configuration in the presence of tetrodotoxin (0.5 μM) and an offline analysis was conducted using a sliding template algorithm (ClampFit 10, Molecular Device) according to previous work (*Zhou et al., 2017*). To estimate the RRP size and release Pr, a repeated 20 Hz train stimulation protocol was used to evoke 40 EPSCs. The RRP size was calculated by linear interpolating the linear portion of the cumulative EPSC amplitude plot to virtual stimulus 0. The release Pr was calculated as the mean amplitude of the 1st EPSC during the repeated train stimulations divided by the RRP size (*He et al., 2019*).

649

650 **Compensatory eye movement test**

651 Mice (P60) were surgically prepared for head-restrained recordings of compensatory eye
652 movements. A pedestal was attached to the skull after shaving and opening the skin overlaying it,
653 using Optibond primer and adhesive (Kerr, Bioggio, Switzerland) and under isoflurane anesthesia
654 in O2 (induction with 4% and maintained at 1.5% concentration). Mice were administered
655 xylocaine and an injection with bupivacaine hydrochloride (2.5 mg/ml, bupivacaine actavis) to
656 locally block sensation. The pedestal consisted of a brass holder (7 × 4 mm base plate) with a
657 neodymium magnet (4 × 4 × 2 mm) and a screw hole for fixation. After a recovery period of at
658 least 3 days, mice were placed in a mouse holder, using the magnet and a screw to fix the pedestal
659 to a custom-made restrainer, and the mouse was placed with the head in the center on a turntable
660 (diameter 60 cm) in the experimental setup. A drum (diameter 63 cm) surrounded the mouse
661 during the experiment. The recording camera was calibrated by moving the camera left–right by
662 20˚ peak to peak at different light levels. Compensatory eye movement performance was
663 examined by recording the OKR, VOR, and VVOR using a sinusoidal rotation of the drum in light
664 (OKR), rotation of the table in the dark (VOR), or rotation of the table (VVOR) in the light. These
665 reflexes were evoked by rotating the table and/or drum at 0.1 to 1 Hz (20 to 8 cycles, each
666 recorded twice) with a fixed 5º amplitude. In order to evaluate motor learning, a mismatch
667 between visual and vestibular input was used to adapt the VOR. The ability to perform VOR phase
668 reversal was tested using a 5-day paradigm, consisting of six 5-minute training sessions every day
669 with VOR recordings before, between, and after the training sessions. On the first day during
670 training, the visual and vestibular stimuli rotated in phase at 0.6 Hz and at the same amplitude,

inducing a decrease of gain. On the subsequent days, the drum amplitude was increased relative to the table and induced the phase reversal of the VOR, resulting in a compensatory eye movement in the same direction as the head rotation instead of the normal compensatory opposite direction (all days vestibular 5º rotation, visual day 2: 5º; day 3, 7.5º; days 4–5, 10º). Between recording sessions, mice were kept in the dark to avoid unlearning of the adapted responses.

Eye movements were recorded with a video-based eye-tracking system (hard- and software, ETL-200; ISCAN systems, Burlington, MA). Recordings were always taken from the left eye. The eye was illuminated during the experiments using two table-fixed infrared emitters (output 600 mW, dispersion angle 7º, peak wavelength 880 nm) and a third emitter that was mounted to the camera, aligned horizontally with the optical axis of the camera, which produced the tracked corneal reflection. Pupil size and corrected (with corneal reflection) vertical and horizontal pupil positions were determined by the ISCAN system, filtered (CyberAmp; Molecular Devices, San Jose, CA), digitized (CED, Cambridge, UK) and stored for offline analysis. All eye movement signals were calibrated, differentiated to obtain velocity signals, and high-pass–filtered to eliminate fast phases, and then cycles were averaged. Gain—the ratio of eye movement amplitude to stimulus amplitude—and phase values—time difference between eye and stimulus expressed in degrees—of eye movements were calculated using custom-made MATLAB routines (The MathWorks, Natick, MA).

Statistical analysis

Experimenters who performed experiments and analyses were blinded to the genotypes until all data were integrated. Data were analyzed using Igor Pro 6.0 (Wavemetrics, Lake Oswego, OR),

693 Graphpad Prism (San Diego, CA), SPSS 16.0 (IBM, Chicago, IL), and MATLAB. No statistical
694 methods were used to pre-determine sample sizes, which were based on our previous studies. All
695 data sets were tested for the assumptions of normality of distribution. No data were excluded
696 except electrophysiological recordings with ≥15% variance in series resistance, input resistance,
697 or holding current. Standard deviations for control were calculated from the average of all control
698 data. Statistical differences were determined using unpaired two-sided Student's *t* test for
699 two-group comparison, or one-way ANOVA followed by Tukey's post hoc post hoc test for
700 multiple comparisons, or repeated measures ANOVA for repeated measures. The accepted level of
701 significance was $p < 0.05$. "*n*" represents the number of preparations or cells. Data in the text and
702 figures are presented as mean ± SEM.

References

Acuna C, Liu X, Südhof TC. 2016. How to make an active zone: unexpected universal functional redundancy between RIMs and RIM-BPs. *Neuron* **91**:792–807. DOI: 10.1016/j.neuron.2016.07.042, PMID: 27537484.

Andreescu CE, Prestori F, Brandalise F, D'Errico A, De Jeu MT, Rossi P, Botta L, Kohr G, Perin P, D'Angelo E, et al. 2011. NR2A subunit of the N-methyl D-aspartate receptors are required for potentiation at the mossy fiber to granule cell synapse and vestibulo-cerebellar motor learning. *Neuroscience* **176**:274–283. DOI: 10.1016/j.neuroscience.2010.12.024, PMID: 21185357

Badura A, Clopath C, Schonewille M, De Zeeuw CI. 2016. Modeled changes of cerebellar activity in mutant mice are predictive of their learning impairments. *Scientific Reports* **6**:36131. DOI: 10.1038/srep36131, PMID: 27805050.

Betz A, Thakur P, Junge HJ, Ashery U, Rhee JS, Scheuss V, Rosenmund C, Rettig J, Brose N. 2001. Functional interaction of the active zone proteins Munc13-1 and RIM1 in synaptic vesicle priming. *Neuron* **30**:183–196. DOI: 10.1016/s0896-6273(01)00272-0, PMID: 11343654.

Brushia RJ, Walsh DA. 1999. Phosphorylase kinase: the complexity of its regulation is reflected in the complexity of its structure. *Frontiers in Bioscience* **4**:D618–641. DOI: 10.2741/brushia, PMID: 10487978.

Cheng X, Ji Z, Tsalkova T, Mei F. 2008. Epac and PKA: a tale of two intracellular cAMP receptors. *Acta Biochim Biophys Sin* **40**:651–662. DOI: 10.1111/j.1745-7270.2008.00438.x, PMID: 18604457.

Davies MS, Cox JW, Berners-Price SJ, Barklage W, Qu Y, Farrell N. 2000. Equilibrium and kinetic studies of the aquation of the dinuclear platinum complex [[trans-PtCl(NH3)2]2(mu-NH2(CH2)6NH2)]2+: pKa determinations of aqua ligands via [1H,15N] NMR spectroscopy. *Inorganic Chemistry* **39**:1710–1715. DOI: 10.1021/ic991104h, PMID: 12526558.

de Rooij J, Zwartkruis FJ, Verheijen MH, Cool RH, Nijman SM, Wittinghofer A, Bos JL. 1998. Epac is a Rap1 guanine-nucleotide-exchange factor directly activated by cyclic AMP. *Nature* **396**:474–477. DOI: 10.1038/24884, PMID: 9853756.

De ZeeuW CI. 2021. Bidirectional learning in upbound and downbound microzones of the cerebellum. *Nature Reviews Neuroscience* **22**, 92–110. DOI: 10.1038/s41583-020-00392-x, PMID: 33203932.

Dulubova I, Lou X, Lu J, Huryeva I, Alam A, Schneggenburger R, Südhof TC, Rizo J. 2005. A Munc13/RIM/Rab3 tripartite complex: from priming to plasticity? *EMBO Journal* **24**:2839–2850. DOI: 10.1038/sj.emboj.7600753, PMID: 16052212.

Fernandes HB, Riordan S, Nomura T, Remmers CL, Kraniotis S, Marshall JJ, Kukreja L, Vassar R, Contractor A. 2015. Epac2 mediates cAMP-dependent potentiation of neurotransmission in the hippocampus. *Journal of Neuroscience* ***35***:6544–6553. DOI: 10.1523/JNEUROSCI.0314-14.2015, PMID: 25904804.

Ferrero JJ, Alvarez AM, Ramírez-Franco J, Godino MC, Bartolomé-Martín D, Aguado C, Torres M, Luján R, Ciruela F, Sánchez-Prieto J. 2013. β-Adrenergic receptors activate exchange protein directly activated by cAMP (Epac), translocate Munc13-1, and enhance the Rab3A-RIM1α interaction to potentiate glutamate release at cerebrocortical nerve terminals.

Journal of Biological Chemistry **288**:31370–31385. DOI: 10.1074/jbc.M113.463877, PMID: 24036110.

Galliano E, Gao Z, Schonewille M, Todorov B, Simons E, Pop AS, D'Angelo E, van den Maagdenberg AM, Hoebeek FE, De Zeeuw CI. 2013. Silencing the majority of cerebellar granule cells uncovers their essential role in motor learning and consolidation. *Cell Reports* **3**:1239–1251. DOI: 10.1016/j.celrep.2013.03.023, PMID: 23583179.

Gao Z, van Beugen BJ, De Zeeuw CI. 2012. Distributed synergistic plasticity and cerebellar learning. *Nature Reviews Neuroscience* **13**:619–635. DOI: 10.1038/nrn3312, PMID: 22895474.

Gekel I, Neher E. 2008. Application of an Epac activator enhances neurotransmitter release at excitatory central synapses. *Journal of Neuroscience* **28**:7991–8002. DOI: 10.1523/JNEUROSCI.0268-08.2008, PMID: 18685024.

Grasselli G, Boele HJ, Titley HK, Bradford N, van Beers L, Jay L, Beekhof GC, Busch SE, De Zeeuw CI, Schonewille M, et al. 2020. SK2 channels in cerebellar Purkinje cells contribute to excitability modulation in motor-learning-specific memory traces. *PLoS Biology* **18**:e3000596. DOI: 10.1371/journal.pbio.3000596, PMID: 31905212.

Gutierrez-Castellanos N, Da Silva-Matos CM, Zhou K, Canto CB, Renner MC, Koene LMC, Ozyildirim O, Sprengel R, Kessels HW, De Zeeuw CI. 2017. Motor learning requires Purkinje cell synaptic potentiation through activation of AMPA-receptor subunit GluA3. *Neuron* **93**:409–424. DOI: 10.1016/j.neuron.2016.11.046, PMID: 28103481.

Han Y, Kaeser PS, Südhof TC, Schneggenburger R. 2011. RIM determines Ca^{2+} channel density and vesicle docking at the presynaptic active zone. *Neuron* **69**:304–316. DOI:

10.1016/j.neuron.2010.12.014, PMID: 21262468.

He Y, Wei M, Wu Y, Qin H, Li W, Ma X, Cheng J, Ren J, Shen Y, Chen Z, et al. 2019. Amyloid β oligomers suppress excitatory transmitter release via presynaptic depletion of phosphatidylinositol-4,5-bisphosphate. *Nature Communication* **10**:1193. DOI: 10.1038/s41467-019-09114-z, PMID: 30867420.

Hioki H, Fujiyama F, Taki K, Tomioka R, Furuta T, Tamamaki N, Kaneko T. 2003. Differential distribution of vesicular glutamate transporters in the rat cerebellar cortex. *Neuroscience* **117**:1–6. DOI: 10.1016/s0306-4522(02)00943-0, PMID: 12605886.

Hirano T, Yamazaki Y, Nakamura Y. 2016. LTD, RP, and motor learning. *Cerebellum* **15**:51–53. DOI: 10.1007/s12311-015-0698-0, PMID: 26160222.

Hucho TB, Dina OA, Levine JD. 2005. Epac mediates a cAMP-to-PKC signaling in inflammatory pain: an isolectin B4(+) neuron-specific mechanism. *Journal of Neuroscience* **25**:6119–6126. DOI: 10.1523/JNEUROSCI.0285-05.2005, PMID: 15987941.

Ichikawa R, Hashimoto K, Miyazaki T, Uchigashima M, Yamasaki M, Aiba A, Kano M, Watanabe M. 2016. Territories of heterologous inputs onto Purkinje cell dendrites are segregated by mGluR1-dependent parallel fiber synapse elimination. *Proc. Natl. Acad. Sci. U.S.A. 113*:2282–2287. DOI: 10.1073/pnas.1511513113, PMID: 26858447.

Ito M. 2005. Bases and implications of learning in the cerebellum-adaptive control and internal model mechanism. *Progress in Brain Research* **148**:95–109. DOI: 10.1016/S0079-6123(04)48009-1, PMID: 15661184.

Kaeser PS, Deng L, Wang Y, Dulubova I, Liu X, Rizo J, Südhof TC. 2011. RIM proteins tether Ca^{2+} channels to presynaptic active zones via a direct PDZ-domain interaction. *Cell*

144:282–295. DOI: 10.1016/j.cell.2010.12.029, PMID: 21241895.

Kaeser PS, Kwon HB, Blundell J, Chevaleyre V, Morishita W, Malenka RC, Powell CM, Castillo PE, Südhof TC. 2008. RIM1alpha phosphorylation at serine-413 by protein kinase A is not required for presynaptic long-term plasticity or learning. *Proc. Natl. Acad. Sci. U.S.A.* **105**:14680–14685. DOI: 10.1073/pnas.0806679105, PMID: 18799741.

Kaneko M, Takahashi T. 2004. Presynaptic mechanism underlying cAMP-dependent synaptic potentiation. *Journal of Neuroscience* **24**:5202–5208. DOI: 10.1523/JNEUROSCI.0999-04.2004, PMID: 15175390.

Kawasaki H, Springett GM, Mochizuki N, Toki S, Nakaya M, Matsuda M, Housman DE, Graybiel AM. 1998. A family of cAMP-binding proteins that directly activate Rap1. *Science* **282**:2275–2279. DOI: 10.1126/science.282.5397.2275, PMID: 9856955.

Kimura S, Uchiyama S, Takahashi HE, Shibuki K. 1998. cAMP-dependent long-term potentiation of nitric oxide release from cerebellar parallel fibers in rats. *Journal of Neuroscience* **18**:8551–8558. DOI: 10.1523/JNEUROSCI.18-21-08551.1998, PMID: 9786963.

Kohansal-Nodehi M, Chua JJ, Urlaub H, Jahn R, Czernik D. 2016. Analysis of protein phosphorylation in nerve terminal reveals extensive changes in active zone proteins upon exocytosis. *Elife* **5**:e14530. DOI: 10.7554/eLife.14530, PMID: 27115346.

Kreitzer AC, Carter AG, Regehr WG. 2002. Inhibition of interneuron firing extends the spread of endocannabinoid signaling in the cerebellum. *Neuron* **34**:787–796. DOI: 10.1016/s0896-6273(02)00695-5, PMID: 12062024.

Le Guen M-C, De Zeeuw CI. 2010. Presynaptic plasticity at cerebellar parallel fiber terminals.

Functional Neurology **25**:141–151. PMID: 21232210.

Lev-Ram V, Wong ST, Storm DR, Tsien RY. 2002. A new form of cerebellar long-term potentiation is postsynaptic and depends on nitric oxide but not cAMP. *Proc. Natl. Acad. Sci. U.S.A.* **99**:8389–8393. DOI: 10.1073/pnas.122206399, PMID: 12048250.

Linden DJ, Ahn S. 1999. Activation of presynaptic cAMP-dependent protein kinase is required for induction of cerebellar long-term potentiation. *Journal of Neuroscience* **19**:10221–10227. DOI: 10.1523/JNEUROSCI.19-23-10221.1999, PMID: 10575019.

Lonart G, Schoch S, Kaeser PS, Larkin CJ, Südhof TC, Linden DJ. 2003. Phosphorylation of RIM1alpha by PKA triggers presynaptic long-term potentiation at cerebellar parallel fiber synapses. *Cell* **115**:49–60. DOI: 10.1016/s0092-8674(03)00727-x, PMID: 14532002.

Lucchesi O, Ruete MC, Bustos MA, Quevedo MF, Tomes CN. 2016. The signaling module cAMP/Epac/Rap1/PLCε/IP3 mobilizes acrosomal calcium during sperm exocytosis. *Biochimica Biophysica Acta* **1863**:544–561. DOI: 10.1016/j.bbamcr.2015.12.007, PMID: 26704387.

Martín R, Garcia-Font N, Suarez-Pinilla AS, Bartolome-Martin D, Ferrero JJ, Lujan R, Torres M, Sanchez-Prieto J. 2020. beta-adrenergic receptors/Epac signaling increases the size of the readily releasable pool of synaptic vesicles required for parallel fiber LTP. *Journal of Neuroscience* **40**:8604–8617. DOI: 10.1523/JNEUROSCI.0716-20.2020, PMID: 33046543.

Mei FC, Qiao J, Tsygankova OM, Meinkoth JL, Quilliam LA, Cheng X. 2002. Differential signaling of cyclic AMP: opposing effects of exchange protein directly activated by cyclic AMP and cAMP-dependent protein kinase on protein kinase B activation. *Journal of Biological Chemistry* **277**:11497–11504. DOI: 10.1074/jbc.M110856200, PMID: 11801596.

Murray AJ. 2008. Pharmacological PKA inhibition: all may not be what it seems. *Science Signaling* **1**:re4. DOI: 10.1126/scisignal.122re4, PMID: 18523239.

Oestreich EA, Malik S, Goonasekera SA, Blaxall BC, Kelley GG, Dirksen RT, Smrcka AV. 2009. Epac and phospholipase Cepsilon regulate Ca^{2+} release in the heart by activation of protein kinase Cepsilon and calcium-calmodulin kinase II. *Journal of Biological Chemistry* **284**:1514–1522. DOI: 10.1074/jbc.M806994200, PMID: 18957419.

Persoon CM, Hoogstraaten RI, Nassal JP, van Weering JRT, Kaeser PS, Toonen RF, Verhage M. 2019. The RAB3-RIM pathway is essential for the release of neuromodulators. *Neuron* **104**:1065–1080. DOI: 10.1016/j.neuron.2019.09.015, PMID: 31679900.

Peter S, Ten Brinke MM, Stedehouder J, Reinelt CM, Wu B, Zhou H, Zhou K, Boele HJ, Kushner SA, Lee MG, et al. 2016. Dysfunctional cerebellar Purkinje cells contribute to autism-like behaviour in Shank2-deficient mice. *Nature Communication* **7**:12627. DOI: 10.1038/ncomms12627, PMID: 27581745.

Raymond JL, Medina JF. 2018. Computational principles of supervised learning in the cerebellum. *Annual Review of Neuroscience* **41**:233–253. DOI: 10.1146/annurev-neuro-080317-061948, PMID: 29986160.

Roscioni SS, Kistemaker LEM, Menzen MH, Elzinga CRS, Gosens R, Halayko AJ, Meurs H, Schmidt, M. 2009. PKA and Epac cooperate to augment bradykinin-induced interleukin-8 release from human airway smooth muscle cells. *Respiratory Research* **10**:88. DOI: 10.1186/1465-9921-10-88, PMID: 19788733.

Salin PA, Malenka RC, Nicoll RA. 1996. Cyclic AMP mediates a presynaptic form of LTP at cerebellar parallel fiber synapses. *Neuron* **16**:797–803. DOI:

10.1016/s0896-6273(00)80099-9, PMID: 8607997.

Schmahmann JD, Guell X, Stoodley CJ, Halko MA. 2019. The theory and neuroscience of cerebellar cognition. *Annual Review of Neuroscience* **42**:337–364. DOI: 10.1146/annurev-neuro-070918-050258, PMID: 30939101.

Schmidt M, Evellin S, Weernink PA, von Dorp F, Rehmann H, Lomasney JW, Jakobs KH. 2001. A new phospholipase-C-calcium signalling pathway mediated by cyclic AMP and a Rap GTPase. *Nature Cell Biology* **3**:1020–1024. DOI: 10.1038/ncb1101-1020, PMID: 11715024.

Schoch S, Castillo PE, Jo T, Mukherjee K, Geppert M, Wang Y, Schmitz F, Malenka RC, Südhof TC. 2002. RIM1alpha forms a protein scaffold for regulating neurotransmitter release at the active zone. *Nature* **415**:321–326. DOI: 10.1038/415321a, PMID: 11797009.

Schonewille M, Belmeguenai A, Koekkoek SK, Houtman SH, Boele HJ, van Beugen BJ, Gao Z, Badura A, Ohtsuki G, Amerika WE, et al. 2010. Purkinje cell-specific knockout of the protein phosphatase PP2B impairs potentiation and cerebellar motor learning. *Neuron* **67**:618–628. DOI: 10.1016/j.neuron.2010.07.009, PMID: 20797538.

Schonewille M, Girasole AE, Rostaing P, Mailhes-Hamon C, Ayon A, Nelson AB, Triller A, Casado M, De Zeeuw CI, Bouvier G. 2021. NMDARs in granule cells contribute to parallel fiber-Purkinje cell synaptic plasticity and motor learning. Proc. *Natl. Acad. Sci. U.S.A.* **118**:e2102635118. DOI: 10.1073/pnas.2102635118, PMID: 34507990.

Steinberg JP, Takamiya K, Shen Y, Xia J, Rubio ME, Yu S, Jin W, Thomas GM, Linden DJ, Huganir RL. 2006. Targeted in vivo mutations of the AMPA receptor subunit GluR2 and its interacting protein PICK1 eliminate cerebellar long-term depression. *Neuron* **49**:845–860. DOI: 10.1016/j.neuron.2006.02.025, PMID: 16543133.

879 **Südhof TC**. 2004. The synaptic vesicle cycle. *Annual Review of Neuroscience* **27**:509–547. DOI:
880 10.1146/annurev.neuro.26.041002.131412, PMID: 15217342.

881 **Sun L**, Bittner MA, Holz RW. 2003. Rim, a component of the presynaptic active zone and
882 modulator of exocytosis, binds 14-3-3 through its N terminus. *Journal of Biological*
883 *Chemistry* **278**:38301–38309. DOI: 10.1074/jbc.M212801200, PMID: 12871946.

884 **ten Brinke MM**, Boele HJ, Spanke JK, Potters JW, Kornysheva K, Wulff P, IJpelaar AC,
885 Koekkoek SK, De Zeeuw CI. 2015. Evolving models of Pavlovian conditioning: cerebellar
886 cortical dynamics in awake behaving mice. *Cell Reports* **13**:1977–1988. DOI:
887 10.1016/j.celrep.2015.10.057, PMID: 26655909.

888 **van Beugen BJ**, Gao Z, Boele HJ, Hoebeek F, De Zeeuw CI. 2013. High frequency burst firing of
889 granule cells ensures transmission at the parallel fiber to purkinje cell synapse at the cost of
890 temporal coding. *Frontiers in Neural Circuits* **7**:95. DOI: 10.3389/fncir.2013.00095, PMID:
891 23734102.

892 **Voges K,** Wu B, Post L, Schonewille M, De Zeeuw CI. 2017. Mechanisms underlying
893 vestibulo-cerebellar motor learning in mice depend on movement direction. *Journal of*
894 *Physiology* **595**:5301–5326. DOI: 10.1113/JP274346, PMID: 28586131.

895 **Wagner MJ**, Luo L. 2020. Neocortex-cerebellum circuits for cognitive processing. *Trends in*
896 *Neuroscience* **43**, 42–54. DOI: 10.1016/j.tins.2019.11.002, PMID: 31787351.

897 **Wang CC**, Weyrer C, Fioravante D, Kaeser PS, Regehr WG. 2021a. Presynaptic short-term
898 plasticity persists in the absence of PKC phosphorylation of Munc18-1. *Journal of*
899 *Neuroscience* **41**:7329–7339. DOI: 10.1523/JNEUROSCI.0347-21.2021, PMID: 34290081.

900 **Wang DJ**, Su LD, Wang YN, Yang D, Sun CL, Zhou L, Wang XX, Shen Y. 2014. Long-term

potentiation at cerebellar parallel fiber-Purkinje cell synapses requires pre- and postsynaptic signaling cascades. *Journal of Neuroscience* **34**:2355–2364. DOI: 10.1152/jn.00175.2018, PMID: 29668384.

Wang X, Hu B, Zimmermann B, Kilimann MW. 2001. Rim1 and rabphilin-3 bind Rab3-GTP by composite determinants partially related through N-terminal alpha-helix motifs. *Journal of Biological Chemistry* **276**:32480–32488. DOI: 10.1074/jbc.M103337200, PMID: 11431472.

Wang XT, Zhou L, Cai XY, Xu FX, Xu ZH, Li XY, Shen Y. 2021b. Deletion of Mea6 in cerebellar granule cells impairs synaptic development and motor performance. *Frontiers in Cell & Development Biology* **8**:627146. DOI: 10.3389/fcell.2020.627146, PMID: 33718348.

Weisskopf MG, Castillo PE, Zalutsky RA, Nicoll RA. 1994. Mediation of hippocampal mossy fiber long-term potentiation by cyclic AMP. *Science* **265**:1878–1882. DOI: 10.1126/science.7916482, PMID: 7916482.

Wu B, Blot FG, Wong AB, Osório C, Adolfs Y, Pasterkamp RJ, Hartmann J, Becker EB, Boele H J, De Zeeuw CI, Schonewille M. 2019. TRPC3 is a major contributor to functional heterogeneity of cerebellar Purkinje cells. *eLife* **8**:e45590. DOI: 10.7554/eLife.45590, PMID: 31486767.

Wulff P, Schonewille M, Renzi M, Viltono L, Sassoè-Pognetto M, Badura A, Gao Z, Hoebeek FE, van Dorp S, Wisden W, et al. 2009. Synaptic inhibition of Purkinje cells mediates consolidation of vestibulo-cerebellar motor learning. *Nature Neuroscience* **12**:1042–1049. DOI: 10.1038/nn.2348, PMID: 19578381.

Yang Y, Calakos N. 2010. Acute in vivo genetic rescue demonstrates that phosphorylation of RIM1alpha serine 413 is not required for mossy fiber long-term potentiation. *Journal of Neuroscience* **30**:2542–2546. DOI: 10.1523/JNEUROSCI.4285-09.2010, PMID: 20164339.

924 **Yang Y**, Shu X, Liu D, Shang Y, Wu Y, Pei L, Xu X, Tian Q, Zhang J, Qian K, et al. 2012. EPAC
925 null mutation impairs learning and social interactions via aberrant regulation of miR-124 and
926 Zif268 translation. *Neuron* **73**:774–788. DOI: 10.1016/j.neuron.2012.02.003, PMID:
927 22365550.

928 **Zhao K**, Wen R, Wang X, Pei L, Yang Y, Shang Y, Bazan N, Zhu LQ, Tian Q, Lu Y. 2013.
929 EPAC inhibition of SUR1 receptor increases glutamate release and seizure vulnerability.
930 *Journal of Neuroscience* **33**:8861–8865. DOI: 10.1523/JNEUROSCI.5686-12.2013, PMID:
931 23678128.

932 **Zhou JH**, Wang XT, Zhou L, Zhou L, Xu FX, Su LD, Wang H, Jia F, Xu FQ, Chen GQ, et al.
933 2017. Ablation of TFR1 in Purkinje cells inhibits mGlu1 trafficking and impairs motor
934 coordination, but not autistic-like behaviors. *Journal of Neuroscience* **37**:11335–11352. DOI:
935 10.1523/JNEUROSCI.1223-17.2017, PMID: 29054881.

936 **Zhou L**, Yang D, Wang DJ, Xie YJ, Zhou JH, Zhou L, Huang H, Han S, Shao CY, Li HS, et al.
937 2015. Numb deficiency in cerebellar Purkinje cells impairs synaptic expression of
938 metabotropic glutamate receptor and motor coordination. *Proc. Natl. Acad. Sci. U.S.A.*
939 **112**:15474–15479. DOI: 10.1073/pnas.1512915112, PMID: 26621723.

Acknowledgements

We thank Drs. Jia-Dong Chen and Yan Gu for their comments on this work, Drs. You-Min Lu and Wei Mo for providing *Epac*^{dKO} and *Math1*-Cre mice, Dr. Lan Bao for providing assistance in electron microscopy, Drs. Min Wu and Jun Xia for their participation at the beginning of this work, and the Core Facilities of Zhejiang University Institute of Neuroscience for technical assistance. This work was supported by grants from National Natural Science Foundation of China (81625006 to Y.S., 31820103005 to Y.S., 32000692 to X.T.W., 32160192 to Y.W., 32100791 to F.X.X., 31900741 to L.Z., 32170976 to L.Z.), National Key Research and Development Program of the Ministry of Science and Technology of China (2020YFB1313500 to L.Z.), Science and Technology Innovation Commission of Shenzhen Municipal Government (JCYJ20160331115633182 to S.J.J.), Ningxia Key Research and Development Program (2021BEG03097 to Y.W.), ERC-Stg (680235 to M.S.), the Dutch Organization for Medical Sciences (C.I.D.Z.), Life Sciences (C.I.D.Z.), and ERC-adv and ERC-POC of the EU (C.I.D.Z.), INTENSE (C.I.D.Z.), and the NIN Vriendenfonds for albinism (C.I.D.Z.).

Ethics

All of the animals were handled according to approved protocol of the Animal Experimentation Ethics Committee of Zhejiang University (ZJU17067).

Figure legends

Figure 1. Threonine phosphorylation of RIM1 by EPAC and PKCε. (A) Schematic showing purification of cerebellar synaptosomes and phophorylation assay of RIM1. (B) Immunostaining of EPAC1 or EPAC2 along with vGluT1 (arrowheads) in cerebellar synaptosomes. Scale bars, 5 μm. (C) Precleared synaptosomes (WT) were immunoprecipitated with anti-RIM1 antibody and probed with antibodies to EPAC1, EPAC2 and RIM1. Rabbit IgG was negative control. $n = 4$. (D) WT synaptosomes were treated with control buffer (Ctrl) or 8-pCPT (20 μM, 30 min) and p-Thr and p-Ser of RIM1 were analyzed. Arrowheads mark non-RIM1 proteins. p-Thr and p-Ser were normalized to corresponding RIM1 and percentage changes relative to Ctrl are plotted. p-Thr: 100 ± 8% (Ctrl) and 179 ± 18% (8-pCPT; $p = 0.0019$). p-Ser: 100 ± 6% (Ctrl) and 97 ± 11% (8-pCPT; $p = 0.77$). Unpaired *t* test. $n = 5$ for all groups. $^{**}p < 0.01$. (E) p-Thr and p-Ser of RIM1 in WT synaptosomes treated with control buffer, forskolin (FSK; 20 μM, 30 min), or FSK+ESI-09 (50 μM, 30 min) (FSK+ESI). Arrowhead marks nonspecific protein. p-Thr: 100 ± 8% (Ctrl), 205 ± 18% (FSK; $p < 0.001$ *vs.* Ctrl), and 101 ± 14% (FSK+ESI; $p = 0.98$ *vs.* Ctrl; $p < 0.001$ *vs.* FSK). One-way ANOVA test. $n = 5$ for all groups. $^{***}p < 0.001$. (F) Phosphorylation of synaptosomal RIM1 from WT and *Epac*^{dKO} mice. RIM1: 100 ± 4% (WT) and 95 ± 4% (*Epac*^{dKO}; $p = 0.41$). p-Thr: 100 ± 3% (WT) and 65 ± 6% (*Epac*^{dKO}; $p = 0.0003$). p-Ser: 100 ± 5% (WT) and 95 ± 9% (*Epac*^{dKO}; $p = 0.67$). Unpaired *t* test. $n = 6$ for all groups. $^{***}p < 0.001$. (G) Schematic depiction of proposed working model. (H) Immunostaining of PKCε and vGluT1 (arrowheads) in cerebellar synaptosomes. Scale bar, 5 μm. (I) WT synaptosomes were treated with control buffer or 8-pCPT (20 μM, 30 min). The phosphorylations of PKCε and PKCα were normalized to β-tubulin and

980 percentage changes relative to control are plotted. pPKCε: 100 ± 5% (Ctrl) and 142 ± 7% (8-pCPT;
981 $p = 0.0007$). PKCα-pSer: 100 ± 8% (Ctrl) and 113 ± 11% (8-pCPT; $p = 0.31$). PKCα-pThr: 100 ±
982 7% (Ctrl) and 93 ± 10% (8-pCPT; $p = 0.54$). Unpaired *t* test. $n = 5$ for all groups. ***$p < 0.001$. (J)
983 Phosphorylation of synaptosomal PKCε and PKCα in WT and *Epac*^{dKO} mice. pPKCε, PKCα-pSer
984 and PKCα-pThr were normalized to β-tubulin and their percentage changes relative to WT are
985 plotted. pPKCε: 100 ± 5% (WT) and 64 ± 7% (*Epac*^{dKO}; $p = 0.0013$). PKCα-pSer: 100 ± 4% (WT)
986 and 103 ± 8% (*Epac*^{dKO}; $p = 0.70$). PKCα-pThr: 100 ± 6% (WT) and 103 ± 7% (*Epac*^{dKO}; $p =$
987 0.73). Unpaired *t* test. $n = 6$ for all groups. **$p < 0.01$. (K) Phosphorylation of synaptosomal
988 RIM1 in *Prkce*$^{f/f}$ and *Prkce*^{cKO} mice. RIM1: 100 ± 6% (WT) and 99 ± 6% (*Epac*^{dKO}; $p = 0.88$).
989 p-Thr: 100 ± 3% (*Prkce*$^{f/f}$) and 65 ± 6% (*Prkce*^{cKO}; $p = 0.0028$). p-Ser: 100 ± 5% (*Prkce*$^{f/f}$) and 95
990 ± 9% (*Prkce*^{cKO}; $p = 0.57$). Unpaired *t* test. $n = 6$ for all groups. **$p < 0.01$. (L) Synaptosomes
991 (*Prkce*^{cKO}) were treated wi/wo 8-pCPT (20 μM, 30 min) and RIM1 phosphorylation was analyzed.
992 p-Thr: 100 ± 8%(*Prkce*^{cKO}) and 108 ± 10% (*Prkce*^{cKO}+8-pCPT; $p = 0.55$). p-Ser: 100 ± 7%
993 (*Prkce*^{cKO}) and 106 ± 6% (*Prkce*^{cKO}+8-pCPT; $p = 0.57$). Unpaired *t* test. $n = 6$ for all groups.

Figure 2. EPAC and PKCε act on vesicle docking, synaptic release, and Rab3-RIM1-Munc13 complex. (A) Representative EM (23,000×) of PF-PC synapses of WT and *Epac*^{dKO} mice. Scale bars: 200 nm. The inserts show docked vesicles. Unpaired *t* test. ****$p < 0.0001$. (B) Representative EM of PF-PC synapses of *Prkce*$^{f/f}$ and *Prkce*^{cKO} mice. Scale bars: 200 nm. Unpaired *t* test. ****$p < 0.0001$. (C) Example PC mEPSCs in *Math1*-Cre and *Epac1*^{cKO};*Epac2*^{cKO} mice. Lower: statistics of inter-event interval and amplitude. Grey dots indicate individual data points. Frequency: 2.0 ± 0.2 Hz (*Math1*-Cre) and 1.4 ± 0.2 Hz (*Epac1*^{cKO};*Epac2*^{cKO}; $p = 0.0036$). Amplitude: 18.3 ± 1.3 pA (*Math1*-Cre) and 18.5 ± 1.3 pA (*Epac1*^{cKO};*Epac2*^{cKO}; $p = 0.46$). Unpaired *t* test. n = for all groups. **$p < 0.01$. (D) Example PC mEPSCs from *Prkce*$^{f/f}$ and *Prkce*^{cKO} mice. Frequency: 1.9 ± 0.1 Hz (*Prkce*$^{f/f}$; $n = 19$) and 1.3 ± 0.1 Hz (*Prkce*^{cKO}; $n = 20$; $p = 0.00059$). Amplitude: 17.9 ± 1.2 pA (*Prkce*$^{f/f}$; $n = 19$) and 17.5 ± 1.1 pA (*Prkce*^{cKO}; $n = 20$; $p = 0.39$). Unpaired *t* test. ***$p < 0.001$. (E) Representative responses of *Math1*-Cre and *Epac1*^{cKO};*Epac2*^{cKO} PCs to 20-Hz PF stimulation. RRP size was defined as the y-intercept of the linear portion of cumulative amplitude curve. For cumulative amplitude, *Math1*-Cre: 5617 ± 358 pA; *Epac1*^{cKO};*Epac2*^{cKO}: 4971 ± 424 pA; $p = 0.037$, unpaired *t* test. Pr was calculated as mean EPSC amplitude (mean value of 1st EPSCs) divided by RRP size (*Math1*-Cre: 0.068 ± 0.015; *Epac1*^{cKO};*Epac2*^{cKO}: 0.044 ± 0.010; $p = 0.048$, unpaired *t* test). $n = 10$ for all groups. *$p < 0.05$. (F) Representative responses of *Prkce*$^{f/f}$ and *Prkce*^{cKO} PCs to 20-Hz PF stimulation. Cumulative amplitude: *Prkce*$^{f/f}$, 5125 ± 461 pA, $n = 11$; *Prkce*^{cKO}, 3996 ± 316 pA, $n = 12$; $p = 0.041$; Unpaired *t* test. Pr: *Prkce*$^{f/f}$, 0.077 ± 0.011, $n = 11$; *Prkce*^{cKO}, 0.048 ± 0.006, $n = 12$; $p = 0.02$; Unpaired *t* test. *$p < 0.05$. (G) Cerebellar synaptosomes from WT and *Epac*^{dKO} mice were immunoprecipitated by anti-RIM1 antibody, and the immunoprecipitates were probed with antibodies to Munc13-1,

Rab3A, and RIM1. Rabbit IgG was negative control. Ratios of immunoprecipitated Munc13-1 or Rab3A *vs.* RIM1 were normalized to WT. Munc13-1: 100 ± 6% (WT) and 62 ± 8% (*Epac*^{dKO}; p = 0.0081, n = 4). Rab3A: 100 ± 5% (WT) and 63 ± 10% (*Epac*^{dKO}; p = 0.019, n = 4). Total Rab3A and RIM1 were normalized to WT. Munc13-1: 100 ± 2% (WT) and 98 ± 4% (*Epac*^{dKO}; p = 0.73, n = 6). Rab3A: 100 ± 5% (WT) and 98 ± 4% (*Epac*^{dKO}; p = 0.77, n = 6). Unpaired t test. *p < 0.05. **p < 0.01. (H) Immunoprecipitation of Munc13-1 and Rab3A with RIM1 in cerebellar synaptosomes from *Prkce*$^{f/f}$ and *Prkce*^{cKO} mice. Ratios of immunoprecipitated Munc13-1 or Rab3A *vs.* RIM1 were normalized to WT. Munc13-1: 100 ± 2% (*Prkce*$^{f/f}$) and 70 ± 8% (*Prkce*^{cKO}; p = 0.0030). Rab3A: 100 ± 2% (*Prkce*$^{f/f}$) and 89 ± 4% (*Prkce*^{cKO}; p = 0.019). Total Rab3A and RIM1 were normalized to *Prkce*$^{f/f}$. Munc13-1: 100 ± 3% (*Prkce*$^{f/f}$) and 96 ± 5% (*Prkce*^{cKO}; p = 0.46). Rab3A: 100 ± 7% (*Prkce*$^{f/f}$) and 106 ± 5% (*Prkce*^{cKO}; p = 0.52). n = 6 for all groups. Unpaired t test. *p < 0.05. **p < 0.01. (I) Cerebellar synaptosomes (WT) mice were incubated in control buffer or 8-pCPT (20 μM, 30 min) and εV1-2 (5 μM, 30min) and immunoprecipitated. Ratios of immunoprecipitated Munc13-1 or Rab3A *vs.* RIM1 were normalized to control. Munc13-1: 100 ± 8% (Ctrl); 138 ± 12% (8-pCPT; p = 0.041 *vs.* Ctrl); 96 ± 12% (8-pCPT+εV1-2; p = 0.97 *vs.* Ctrl; p = 0.029 *vs.* 8-pCPT). Rab3A: 100 ± 5% (Ctrl); 168 ± 12% (8-pCPT; p = 0.0011 *vs.* Ctrl); 133 ± 12% (8-pCPT+εV1-2; p = 0.069 *vs.* Ctrl; p = 0.046 *vs.* 8-pCPT). One-way ANOVA test. n = 4 for all groups. *p < 0.05. **p < 0.01. (J) Cerebellar synaptosomes (WT) were treated with control buffer or FR236924 (FR) (200 nM, 30 min) and immunoprecipitated. Ratios of immunoprecipitated Munc13-1 or Rab3A *vs.* RIM1 were normalized to Ctrl. Munc13-1: 100 ± 4% (Ctrl) and 144 ± 16% (FR; p = 0.041). Rab3A: 100 ± 4% (Ctrl) and 175 ± 13% (FR; p = 0.0016). Unpaired t test. n = 4 for all groups. *p < 0.05. **p < 0.01. (K) Cerebellar synaptosomes

1038 (*Prkce*^{cKO}) were treated with control buffer or FR236924 and immunoprecipitated. Ratios of

1039 immunoprecipitated Munc13-1 or Rab3A *vs.* RIM1 were normalized to *Prkce*^{cKO}. Munc13-1: 100

1040 ± 3% (*Prkce*^{cKO}; $n = 4$) and 100 ± 12% (*Prkce*^{cKO}+FR; $p = 0.99$; $n = 4$). Rab3A: 100 ± 2%

1041 (*Prkce*^{cKO}; $n = 8$) and 108 ± 9% (*Prkce*^{cKO}+FR; $p = 0.37$; $n = 8$). Unpaired *t* test.

Figure 3. EPAC and PKCε are required for presynaptic PF-PC LTP. (A) Schematic showing the induction of presynaptic LTP. (B, D, F, H, J) Example PF-EPSCs for baseline (1) and after LTP induction (2) in WT (B), *Math1*-Cre (D), *Epac1*^{cKO};*Epac2*^{cKO} (F), *Prkce*$^{f/f}$ (H), and *Prkce*^{cKO} (J) mice. (C) Percentage changes of PF-EPSC amplitudes (WT). (1): 101 ± 4%; (2): 131 ± 6%; $n = 13$; $p < 0.001$. Percentage changes of PPF ratios from cells shown above. (1): 101 ± 3%; (2): 84 ± 4%; $n = 13$; $p < 0.001$. Unpaired *t* test. ***$p < 0.001$. (E) Left: percentage changes of PF-EPSC amplitudes (*Math1*-Cre). (1): 100 ± 2%; (2): 120 ± 5%; $n = 10$; $p = 0.004$. Right: percentage changes of PPF ratios. (1): 102 ± 2%; (2): 83 ± 2%; $n = 10$; $p < 0.001$. Unpaired *t* test. **$p < 0.01$. ***$p < 0.001$. (G) Left: percentage changes of PF-EPSC amplitudes (*Epac1*^{cKO};*Epac2*^{cKO}). (1): 99 ± 2%; (2): 93 ± 4%; $n = 9$; $p = 0.059$. Right: percentage changes of PPF ratios. (1): 101 ± 3%; (2): 101 ± 5%; $n = 9$; $p = 0.07$. Unpaired *t* test. (I) Left: percentage changes of PF-EPSC amplitudes (*Prkce*$^{f/f}$). (1): 99 ± 4%; (2): 120 ± 3%; $n = 7$; $p = 0.004$. Right: percentage changes of PPF ratios. (1): 100 ± 5%; (2): 86 ± 4%; $n = 7$; $p < 0.001$. Unpaired *t* test. **$p < 0.01$. ***$p < 0.001$. (K) Left: percentage changes of PF-EPSC amplitudes (*Prkce*^{cKO}). (1): 101 ± 4%; (2): 99 ± 5%; $n = 10$; $p = 0.065$. Right: percentage changes of PPF ratios. (1): 101 ± 3%; (2): 100 ± 2%; $n = 10$; $p = 0.77$. Unpaired *t* test.

Figure 4. cAMP-triggered PF facilitation is dependent on EPAC and PKCε. (A) The facilitation of PF-EPSCs by forskolin (FSK) (20 μM) in *Math1*-Cre, *Epac1*^{cKO};*Epac2*^{cKO} and *Prkce*^{cKO} mice. (B) Example traces for baseline (1) and after potentiation (2) shown in (A). (C) Left: percent changes of EPSC amplitude. *Math1*-Cre: 366 ± 25% (n = 15); *Epac1*^{cKO};*Epac2*^{cKO}: 162 ± 18% (n = 12; p < 0.001 *vs. Math1*-Cre); *Epac1*^{cKO};*Epac2*^{cKO}+KT: 106 ± 4% (n = 12; p < 0.001 *vs. Math1*-Cre; p = 0.046 *vs. Epac1*^{cKO};*Epac2*^{cKO}); *Prkce*^{cKO}: 198 ± 5% (n = 12; p < 0.001 *vs. Math1*-Cre); *Prkce*^{cKO}+KT: 101 ± 3% (n = 12; p < 0.001 *vs. Math1*-Cre; p = 0.0034 *vs. Prkce*^{cKO}). Right: percent changes of PPF. *Math1*-Cre: 77 ± 2% (n = 15); *Epac1*^{cKO};*Epac2*^{cKO}: 90 ± 1% (n = 12; p < 0.001 *vs. Math1*-Cre); *Epac1*^{cKO};*Epac2*^{cKO}+KT: 94 ± 1% (n = 12; p < 0.001 *vs. Math1*-Cre; p = 0.049 *vs. Epac1*^{cKO};*Epac2*^{cKO}); *Prkce*^{cKO}: 85 ± 2% (n = 12; p < 0.001 *vs. Math1*-Cre); *Prkce*^{cKO}+KT: 95 ± 1% (n = 12; p < 0.001 *vs. Math1*-Cre; p = 0.025 *vs. Prkce*^{cKO}). One-way ANOVA test. *p < 0.05. ***p < 0.001. (D) Bath application of 8-pCPT (20 μM) caused PF-EPSC potentiation in WT mice. Left: example traces before (1) and after potentiation (2). Middle: time course of PF facilitation. Right: percent changes of EPSC amplitude (179 ± 18%; n = 6; p < 0.001) and PPF (83 ± 3%; n = 6; p < 0.001) at 18-20 min *vs.* baseline (0-2 min). Unpaired t test. ***p < 0.001. (E) 8-pCPT failed to induce PF-EPSC potentiation in *Prkce*^{cKO} mice. Left: example traces for baseline (1) and after potentiation (2). Middle: time course of PF facilitation. Right: percent changes of EPSC amplitude (101 ± 6%; n = 6; p = 0.35) and PPF (98 ± 4%; n = 6; p = 0.45) at 18-20 min *vs.* baseline (0-2 min). Unpaired t test. (F) Co-application of 8-pCPT and εV1-2 (5 μM) failed to produce PF potentiation in WT mice. Left: example traces for baseline (1) and after potentiation (2). Middle: time course of PF-EPSCs. Right: percent changes of EPSC amplitude (101 ± 4%; n = 6; p = 0.78) and PPF (101 ± 3%; n = 6; p = 0.67) at 18-20 min *vs.* baseline (0-2

1080 min). Unpaired *t* test.

Figure 5. Postsynaptic PF-PC LTP is intact upon presynaptic deletion of EPAC or PKCε. (A) Schematic showing the induction of postsynaptic LTP. (B, E, H) Example PF-EPSCs for baseline (1) and after induction (2) in WT and *Epac*^{dKO} PCs (B), *Math1*-Cre and *Epac1*^{cKO};*Epac2*^{cKO} PCs (E), and *Prkce*$^{f/f}$ and *Prkce*^{cKO} PCs (H). (C) Percentage changes of PF-EPSC amplitude. In WT, 101 ± 5% for (1) and 131 ± 5% for (2) ($p < 0.001$). In *Epac*^{dKO}, 100 ± 5% for (1) and 106 ± 6% for (2) ($p = 0.26$). Unpaired *t* test. $n = 13$ for both groups. ***$p < 0.001$. (D) Percentage changes of PPF ratios of cells shown in (C). In WT, 100 ± 2% for (1) and 100 ± 3% for (2) ($p = 0.63$). In *Epac*^{dKO}, 101 ± 3% for (1) and 99 ± 4% for (2) ($p = 0.74$). Unpaired *t* test. $n = 13$ for both groups. (F) Percentage changes of PF-EPSC amplitudes. In *Math1*-Cre, 100 ± 5% for (1) and 123 ± 3% for (2) ($p < 0.001$). In *Epac1*^{cKO};*Epac2*^{cKO}, 98 ± 5% for (1) and 119 ± 4% for (2) ($p < 0.001$). Unpaired *t* test. $n = 7$ for both groups. ***$p < 0.001$. (G) Percentage changes of PPF ratios of cells shown in (C). In *Math1*-Cre: 100 ± 2% for (1) and 96 ± 3% for (2) ($p = 0.26$). In *Epac1*^{cKO};*Epac2*^{cKO}: 98 ± 3% for (1) and 95 ± 3% for (2) ($p = 0.28$). Unpaired *t* test. $n = 7$ for both groups. (I) Percentage changes of PF-EPSC amplitude. In *Prkce*$^{f/f}$, 99 ± 4% for (1) and 121 ± 4% for (2) ($p < 0.0001$). In *Prkce*^{cKO}: 97 ± 5% for (1) and 118 ± 5% for (2) ($p < 0.0001$). Unpaired *t* test. $n = 7$ for both groups. ****$p < 0.0001$. (J) Percentage changes of PPF ratios from cells shown in (I). In *Prkce*$^{f/f}$, 102 ± 2% for (1) and 101 ± 2% for (2) ($p = 0.73$). In *Prkce*^{cKO}, 98 ± 2% and 100 ± 2% for (2) ($p = 0.78$). Unpaired *t* test. $n = 7$ for both groups.

Figure 6. PF-LTD is unaltered by presynaptic deletion of EPAC or PKCε. (A) A scheme showing the induction of postsynaptic LTD. (B, E, H) Example PF-EPSCs for baseline (1) and after LTD induction (2) in WT and EPAC^{dKO} PCs (B), *Math1*-Cre and *Epac1*^{cKO};*Epac2*^{cKO} PCs (E), and *Prkce*$^{f/f}$ and *Prkce*^{cKO} PCs (H). (C) Percentage changes of PF-EPSC amplitude. In WT, 101 ± 3% for (1) and 59 ± 5% for (2) ($p < 0.001$). In EPAC^{dKO}, 100 ± 3% for (1) and 59 ± 4% for (2) (< 0.001). Unpaired *t* test. $n = 13$ for both groups. ***$p < 0.001$. (D) Percentage changes of PPF ratios of cells shown in (C). In WT, 100 ± 3% for (1) and 100 ± 5% for (2) ($p = 0.49$). In EPAC^{dKO}, 100 ± 5% for (1) and 100 ± 5% for (2) ($p = 0.26$). Unpaired *t* test. $n = 13$ for both groups. (F) Percentage changes of PF-EPSC amplitude. In *Math1*-Cre, 100 ± 4% for (1) and 61 ± 3% for (2) ($p < 0.0001$). In *Epac1*^{cKO};*Epac2*^{cKO}, 101 ± 3% for (1) and 65 ± 4% for (2) ($p < 0.0001$). Unpaired *t* test. $n = 7$ for both groups. ****$p < 0.0001$. (G) Percentage changes of PPF ratios of cells shown in (F). In *Math1*-Cre, 100 ± 2% for (2) and 100 ± 3% for (2) ($p = 0.40$). In *Epac1*^{cKO};*Epac2*^{cKO}, 101 ± 3% for (2) and 99 ± 4% for (2) ($p = 0.61$). Unpaired *t* test. $n = 7$ for both groups. (I) Percentage changes of PF-EPSC amplitude. In *Prkce*$^{f/f}$, 99 ± 2% for (1) and 66 ± 4% for (2) ($p <$ 0.0001). In *Prkce*^{cKO}, baseline: 101 ± 2% for (1) and 64 ± 6% for (2) ($p < 0.0001$). Unpaired *t* test. $n = 7$ for both groups. ****$p < 0.0001$. (J) Percentage changes of PPF ratios of cells shown in (I). In *Prkce*$^{f/f}$, 101 ± 2% for (1) and 101 ± 2% for (2) ($p = 0.56$). In *Prkce*^{cKO}, 100 ± 2% for (1) and 102 ± 2% for (2) ($p = 0.54$). Unpaired *t* test. $n = 7$ for both groups.

Figure 7. VOR baseline and adaptation in *Math1*-Cre, *Epac1*^{cKO};*Epac2*^{cKO}, *Prkce*$^{f/f}$ and *Prkce*^{cKO} mice. (A) Pictograms depicted compensatory eye movements driven by visual stimulus (OKR), vestibular stimulus (VOR) or both (VVOR). (B) OKR gain (measure of eye movement amplitude) and phase (measure of timing) were smaller in *Epac1*^{cKO};*Epac2*^{cKO} (n = 16) mice compared to *Math1*-Cre (n = 10) mice. (C) VOR was affected in *Epac1*^{cKO};*Epac2*^{cKO} mice. (D) The combination of vestibular and visual input by rotation of the mouse in the light evoked the VVOR in *Math1*-Cre and *Epac1*^{cKO};*Epac2*^{cKO} mice. (E) OKR gain and phase were smaller in *Prkce*^{cKO} (n = 11) mice compared to *Prkce*$^{f/f}$ (n = 10) mice. (F) VOR was affected in *Prkce*^{cKO} mice. (G) VVOR gain and phase in *Prkce*$^{f/f}$ and *Prkce*^{cKO} mice. (H) Mismatched visual and vestibular input was used to trigger adaptation of the eye movements in order to test motor learning ability. This training induced a reversal of VOR phase probed by VOR recordings in the dark. (I) Both gain-decrease learning and phase learning of *Epac1*^{cKO};*Epac2*^{cKO} were impaired. *$p < 0.05$. ***$p < 0.001$. (J) Both gain-decrease learning and phase learning of *Prkce*^{cKO} were impaired. *$p < 0.05$. **$p < 0.01$. ***$p < 0.001$.

Figure 1–figure supplement 1. Threonine phosphorylation of RIM1 by EPAC *in vitro*. (A) Co-transfection of HA-RIM1α with Flag-EPAC1 or Flag-EPAC2 in HEK cells. Arrowheads show the co-localization of RIM1α and EPACs. Scale bars: 100 μm. (B) HA-RIM1α (Ctrl) or HA-RIM1α with Flag-EPACs was transfected into HEK cells and p-Thr and p-Ser of RIM1α were measured. Arrowhead marks non-RIM1 protein. p-Thr: 100 ± 7 (Ctrl), 179 ± 17% (EPAC1; p = 0.0011 *vs.* Ctrl), and 160 ± 13% (EPAC2; p = 0.010 *vs.* Ctrl). p-Ser: 100 ± 5 (Ctrl), 111 ± 12% (EPAC1; p = 0.69 *vs.* Ctrl), and 107 ± 10% (EPAC2; p = 0.87 *vs.* Ctrl). One-way ANOVA test. n = 6 for all groups. *p < 0.05. **p < 0.01. (C) Potential theronine phosphorylation sites by PKC in RIM1α were determined using the NetPhos 3.1 server (Technical University of Denmark; http://www.cbs.dtu.dk/services/NetPhos/). Dashed line: threshold for phosphorylation potential.

Figure 1–figure supplement 2. Generation of *Prkce*^{cKO} and *Epac1*^{cKO};*Epac2*^{cKO} mice and cerebellar cytology. (A) Nissl staining in the cerebellum from WT and *Epac*^{dKO} mice. Scale bars, 100 μm. (B) Golgi staining showing apical PC spines. Scale bars, 2 μm. Average numbers of spines per 10 μm were 15.5 ± 0.6 (WT; n = 19 cells) and 14.3 ± 0.5 (*Epac*^{dKO}; n = 19 cells). p = 0.13. Unpaired t test. (C) The construction of *Prkce*$^{f/f}$ mice. LoxP sites were inserted before and after exon 2 and further excised by *Math1*-Cre. (D) Native tdTomato fluorescence in the brain of *Math1*-Cre;Ai9 mouse. Scale bars: 1 mm. (E) Granule cell contents of *Prkce*$^{f/f}$ and *Prkce*^{cKO} mice were harvested using glass micropipettes and subjected to RT-PCR. *Prkce* (165 bp) was absent in *Prkce*^{cKO} granule cells. ****p < 0.0001. (F) PKCε expression in the cerebellum from *Prkce*$^{f/f}$ and *Prkce*^{cKO} mice. Percentage changes of PKCε: 100 ± 2% (*Prkce*$^{f/f}$; n = 6) and 34 ± 4% (*Prkce*^{cKO}; n = 6). Unpaired t test. ****p < 0.001. (G) Nissl staining in the cerebellum. Scale bars, 100 μm. GCL thickness: 111.0 ± 4.9 μm (*Prkce*$^{f/f}$) and 111.6 ± 5.4 μm (*Prkce*^{cKO}), p = 0.93, unpaired t test. ML thickness: 151.7 ± 5.3 μm (*Prkce*$^{f/f}$) and 148.4 ± 5.3 μm (*Prkce*^{cKO}), p = 0.64, unpaired t test. n = 7 for all groups. (H) Golgi staining showing apical PC spines in *Prkce*$^{f/f}$ and *Prkce*^{cKO} mice. Scale bars, 2 μm. Average numbers of spines per 10 μm: 15.8 ± 0.6 (*Prkce*$^{f/f}$; n = 29 cells) and 15.7 ± 0.6 (*Prkce*^{cKO}; n = 28 cells), p = 0.88, unpaired t test. (I) The construction of *Epac2*$^{f/f}$ mice. LoxP sites were inserted between exons 6 and 9 and further excised by *Math1*-Cre. (J) Granule cell contents of *Epac2*$^{f/f}$ and *Epac2*^{cKO} mice were harvested and subjected to RT-PCR. *Epac2* (180 bp) was absent in *Epac2*^{cKO} granule cells. ****p < 0.001. (K) The construction of *Epac1*$^{f/f}$ mice. LoxP sites were inserted between exons 3 and 18 and further excised by *Math1*-Cre. (L) Granule cell contents of *Epac1*$^{f/f}$ and *Epac1*^{cKO} mice were harvested and subjected to RT-PCR. *Epac1* (218 bp) was absent in *Epac1*^{cKO} granule cells. ****p < 0.001.

Figure 1–figure supplement 3. 8-pCPT-induced RIM1 phosphorylation is blocked by PKCε inhibitor. (A) Flag-RIM1α (Ctrl) or Flag-RIM1α with HA-EPACs was transfected into HEK cells, and the phosphorylation and expression of PKCε and PKCα were normalized to β-actin. For percentage change, pPKCε was 100 ± 5% (Ctrl), 179 ± 13% (EPAC1; p = 0.0003 *vs.* Ctrl), and 160 ± 12% (EPAC2; p = 0.003 *vs.* Ctrl); PKCε was 100 ± 6% (Ctrl), 99 ± 8% (EPAC1; p = 0.96 *vs.* Ctrl), and 101 ± 8% (EPAC2; p = 0.92 *vs.* Ctrl); PKCα-pS was 100 ± 7% (Ctrl), 101 ± 10% (EPAC1; p = 0.94 *vs.* Ctrl), and 96 ± 8% (EPAC2; p = 0.67 *vs.* Ctrl); and PKCα-pT was 100 ± 6% (Ctrl), 97 ± 10% (EPAC1; p = 0.81 *vs.* Ctrl), and 101 ± 8% (EPAC2; p = 0.90 *vs.* Ctrl). One-way ANOVA test. n = 6 for all groups. **p < 0.01. ***p < 0.001. (B) Precleared synaptosomes from WT mice were immunoprecipitated with anti-RIM1 antibody and probed with antibodies to PKCε and RIM1. n = 4. (C) HA-RIM1α (Ctrl) or HA-RIM1α with His-PKCε was transfected into HEK cells and p-Thr and p-Ser of RIM1α were analyzed. p-Thr and p-Ser were normalized to HA and percentage changes relative to Ctrl are plotted. p-Thr was 100 ± 8% (Ctrl) and 179 ± 18% (PKCε; p = 0.0021). p-Ser was 100 ± 11% (Ctrl) and 118 ± 13% (PKCε; p = 0.26). n = 5 for all groups. Unpaired t test. **p < 0.01. (D) Synaptosomes (WT) were treated with control buffer, 8-pCPT (20 μM, 30 min), 8-pCPT+εV1-2 (5 μM, 30min) and 8-pCPT+Gö (10 μM, 30 min). p-Thr was normalized to RIM1 and percentage changes relative to Ctrl are plotted. Ctrl: 100 ± 8%. 8-pCPT: 280 ± 35% (p = 0.0016 *vs.* Ctrl). 8-pCPT+εV1-2: 147 ± 19% (p = 0.58 *vs.* Ctrl; p = 0.015 *vs.* 8-pCPT). 8-pCPT+Gö: 276 ± 31 (p = 0.0019 *vs.* Ctrl; p = 0.99 *vs.* 8-pCPT; p = 0.017 *vs.* 8-pCPT+εV1-2). One-way ANOVA test. n = 4 for all groups. *p < 0.05. **p < 0.01. (E) Synaptosomes (WT) were treated with control buffer, PMA (1 μM, 30 min), PMA+εV1-2 (5 μM, 30min) and PMA+Gö (10 μM, 30 min). RIM1 p-Thr was normalized to RIM1, and percentage

1186 changes relative to Ctrl are plotted. Ctrl: 100 ± 8%. PMA: 208 ± 19% (p = 0.0041 *vs.* Ctrl).

1187 PMA+εV1-2: 134 ± 13% (p = 0.55 *vs.* Ctrl; p = 0.043 *vs.* PMA). PMA+Gö: 214 ± 24% (p =

1188 0.0029 *vs.* Ctrl; p = 0.99 *vs.* PMA; p = 0.030 *vs.* PMA+εV1-2). One-way ANOVA test. n = 4 for

1189 all groups. *$p < 0.05$. **$p < 0.01$.

Figure 3–figure supplement 1. Presynaptic PF-PC LTP is blocked by forskolin incubation, EPAC ablation, or εV1-2 application. (A) Example PF-EPSCs for baseline (1) and after LTP induction (2) in a WT PC perfused with forskolin (20 μM). (B) Percentage changes of PF-EPSC amplitude with forskolin treatment in WT mice: 99 ± 3% (1) and 101 ± 5% (2); n = 11; p = 0.63. PPF ratios from cells shown in the left panel: 100 ± 5% (1) and 102 ± 4% (2); n = 11; p = 0.72. Unpaired t test. (C) Example PF-EPSCs for baseline and after LTP induction in an *Epac*^{dKO} PC. (D) Percentage changes of PF-EPSC amplitude in *Epac*^{dKO} mice: 100 ± 3% (1) and 104 ± 5% (2); n = 11; p = 0.66. PPF ratios from cells shown in the left panel: 99 ± 5% (1) and 104 ± 5% (2); n = 11; p = 0.58. Unpaired t test. (E) Example PF-EPSCs for baseline and after LTP induction in a WT PC perfused with εV1-2 (5 μM). (F) Percentage changes of PF-EPSC amplitude in WT mice: 100 ± 3% (1) and 101 ± 4% (2); n = 9; p = 0.59. PPF ratios from cells shown in the left panel: 101 ± 4% (1) and 102 ± 5% (2); n = 9; p = 0.22. Unpaired t test.

Figure 7–figure supplement 1. Impaired VOR learning in *Epac*^{dKO} mice. (A) Gain and phase values of WT (n = 10) and *Epac*^{dKO} (n = 10) mice during OKR evoked by visual stimulation. **p < 0.01. (B) Gain and phase values of WT and *Epac*^{dKO} mice evoked by vestibular stimulation in the dark. *p < 0.05. **p < 0.01. (C) Gain and phase values of WT and *Epac*^{dKO} mice during VVOR in the light. With visual input, the VOR deficits in *Epac*^{dKO} were no longer present. (D) VOR recordings in the dark revealed a reversal of VOR phase in WT and *Epac*^{dKO} mice. *p < 0.05. **p < 0.01. ***p < 0.001.

Figure 7–figure supplement 2. Proposed schematic model for the function of EPAC-PKCε module in presynaptic LTP and motor learning. In this model, EPAC activation by forskolin or presynaptic tetanus stimulation promotes PKCε activation and phosphorylation threonine of RIM1, which further facilitates the assembly of Rab3A-RIM1-Munc13-1 tripartite complex and the docking of vesicles at active zones. All these events are required for the induction of presynaptic LTP. Importantly, presynaptic LTP is essential to VOR phase adaptation learning.

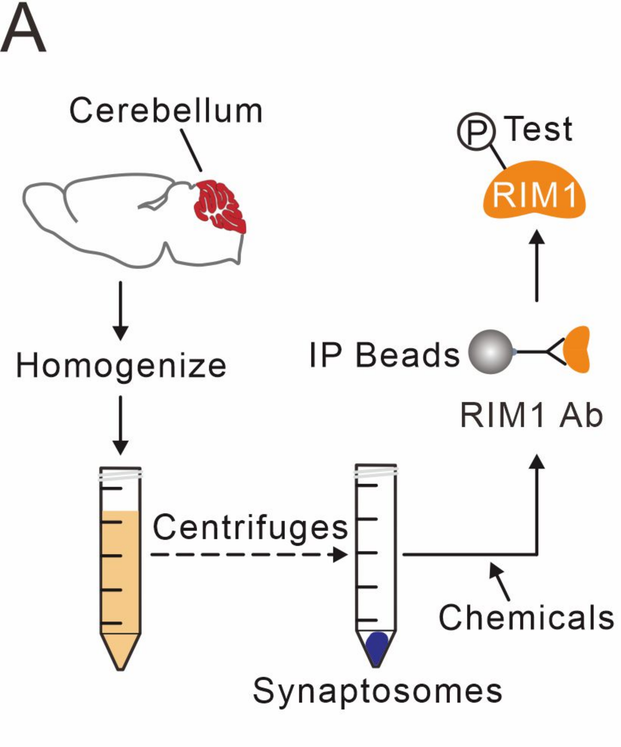
A
Cerebellum
Homogenize
Centrifuges
Synaptosomes
Chemicals
RIM1 Ab
IP Beads
Test
RIM1

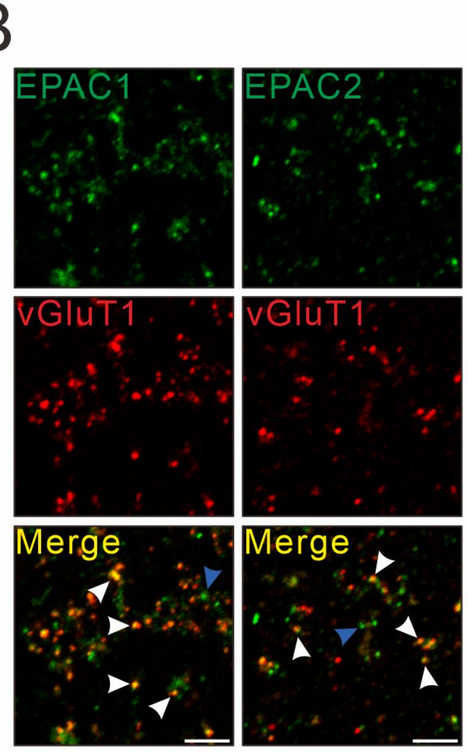
B
EPAC1
EPAC2
vGluT1
vGluT1
Merge
Merge

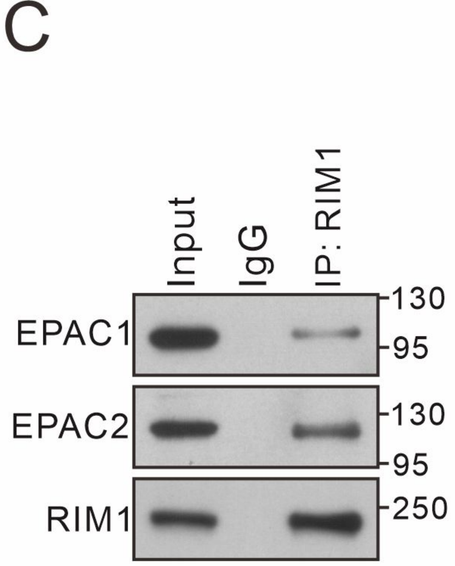
C
Input
IgG
IP: RIM1
EPAC1
EPAC2
RIM1
130
95
130
95
250

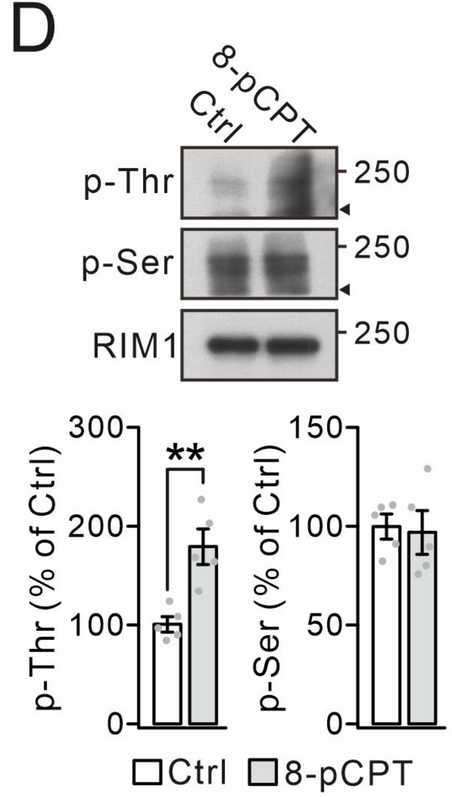
D
Ctrl
8-pCPT
p-Thr
p-Ser
RIM1
250
250
250
p-Thr (% of Ctrl)
p-Ser (% of Ctrl)
**
Ctrl
8-pCPT

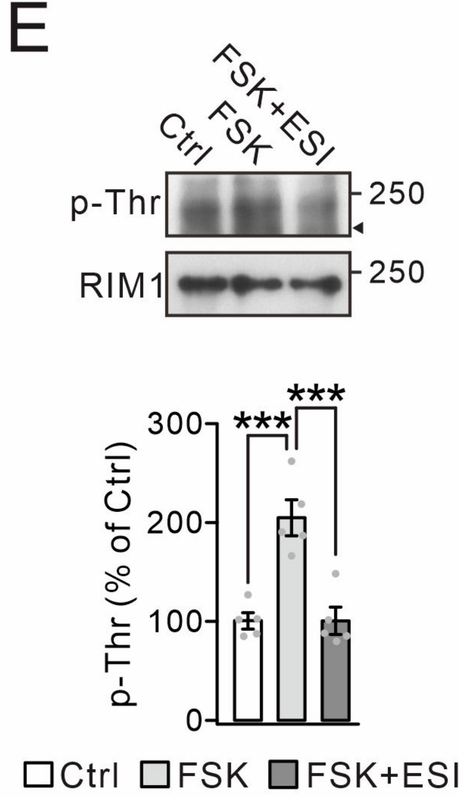
E
Ctrl
FSK
FSK+ESI
p-Thr
RIM1
250
250
p-Thr (% of Ctrl)
***
***
Ctrl
FSK
FSK+ESI

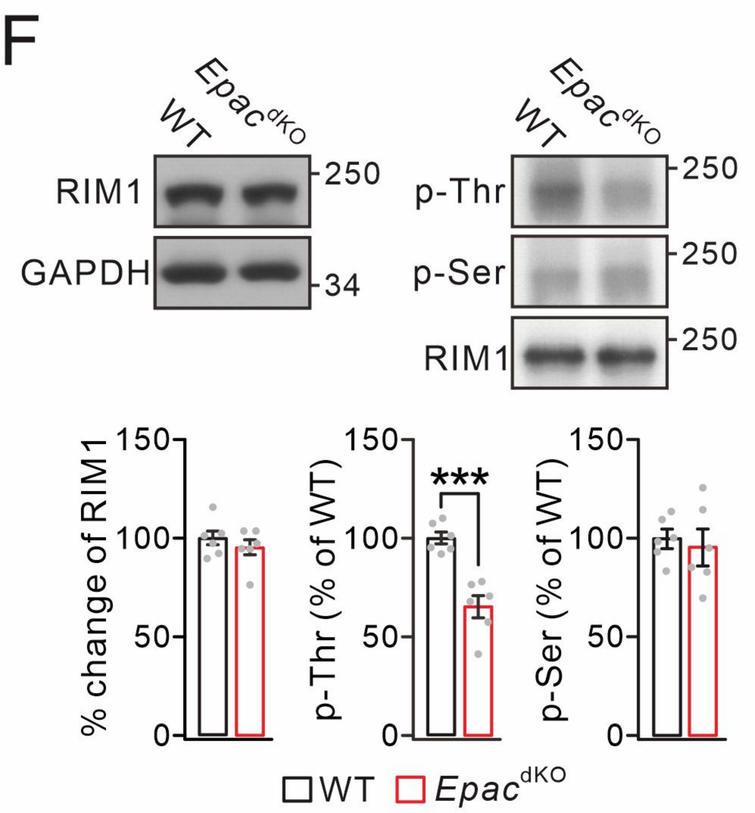
F
WT
Epac dKO
RIM1
GAPDH
250
34
p-Thr
p-Ser
RIM1
250
250
250
% change of RIM1
p-Thr (% of WT)
p-Ser (% of WT)
***
WT
Epac dKO

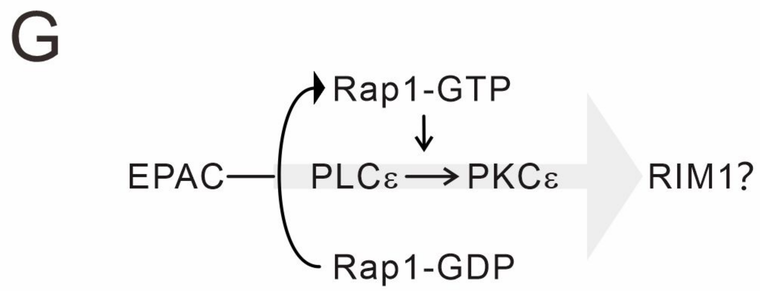
G
EPAC
Rap1-GTP
PLCε
PKCε
Rap1-GDP
RIM1?

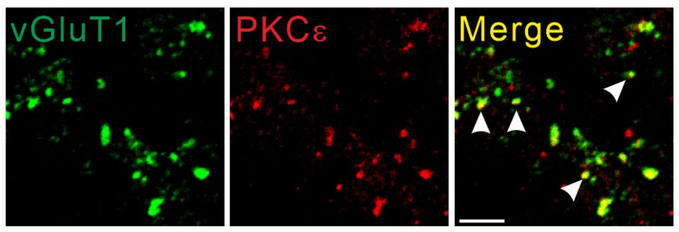
H
vGluT1
PKCε
Merge

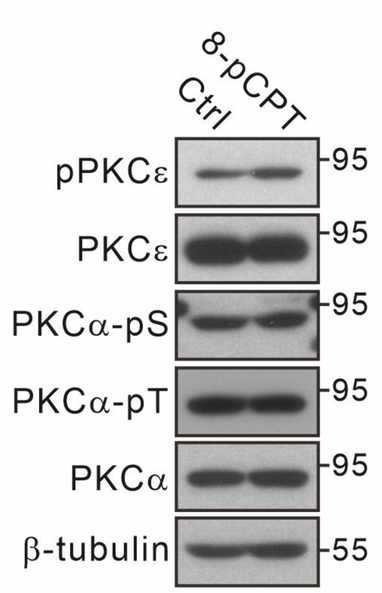
I
8-pCPT
Ctrl
pPKCε
PKCε
PKCα-pS
PKCα-pT
PKCα
β-tubulin
95
95
95
95
95
55
Ctrl
8-pCPT
% Change of Ctrl
***
pPKCε
PKCα-pS
PKCα-pT

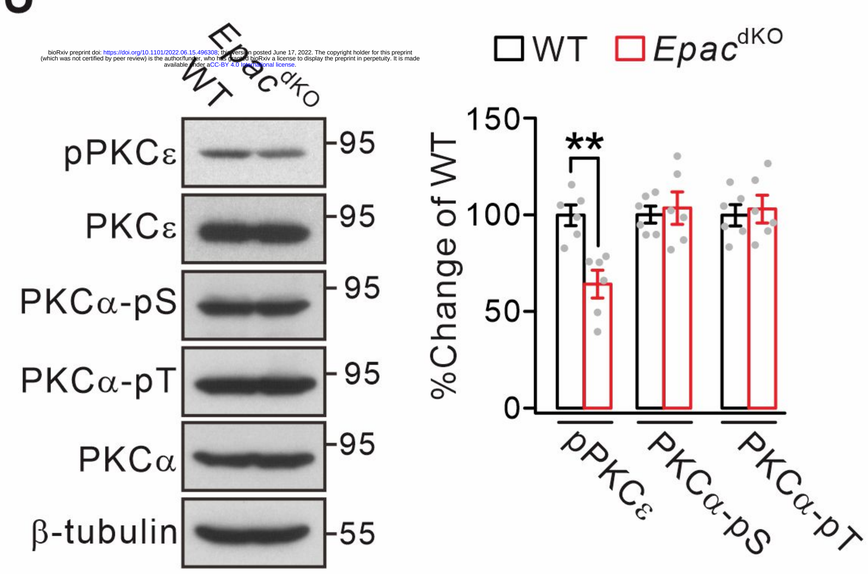
J
WT
Epac dKO
pPKCε
PKCε
PKCα-pS
PKCα-pT
PKCα
β-tubulin
95
95
95
95
95
55
WT
Epac dKO
%Change of WT
**
pPKCε
PKCα-pS
PKCα-pT

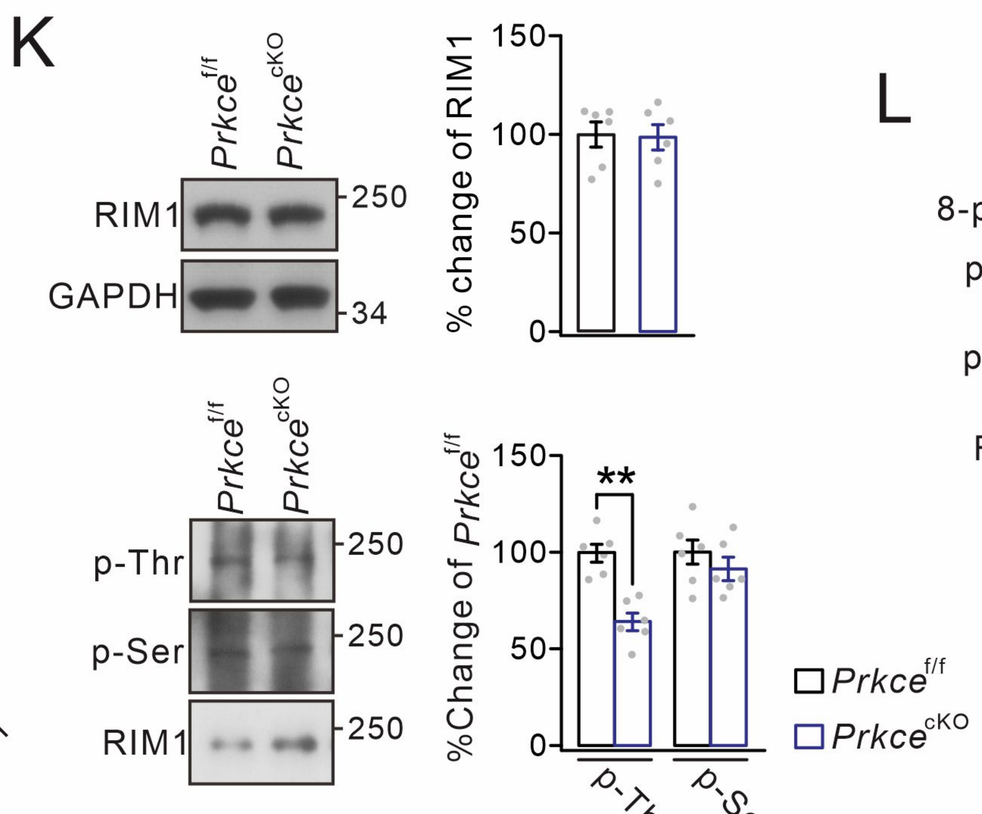
K
Prkce f/f
Prkce cKO
RIM1
GAPDH
250
34
% change of RIM1
p-Thr
p-Ser
RIM1
250
250
250
%Change of Prkce f/f
**
p-Thr
p-Ser
Prkce f/f
Prkce cKO

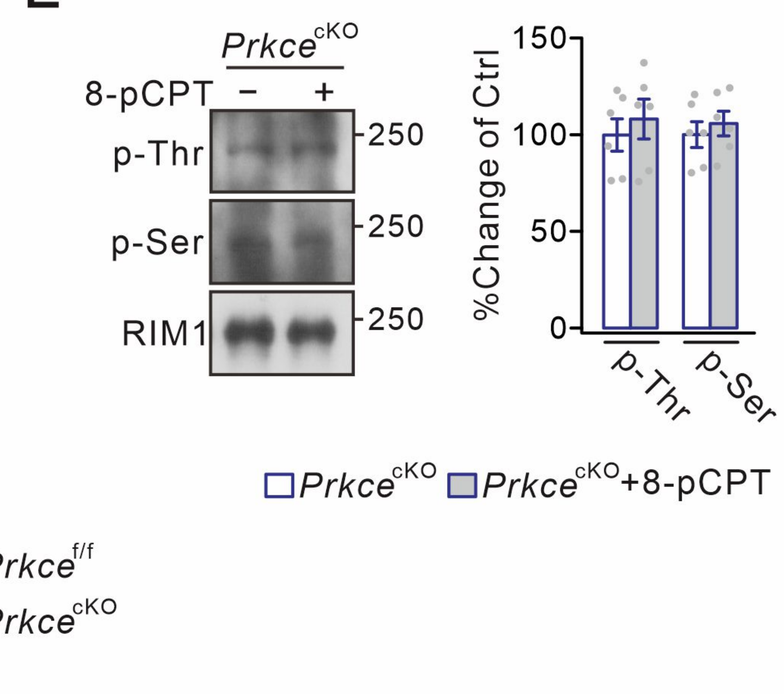
L
Prkce cKO
8-pCPT
–
+
p-Thr
p-Ser
RIM1
250
250
250
%Change of Ctrl
p-Thr
p-Ser
Prkce cKO
Prkce cKO+8-pCPT

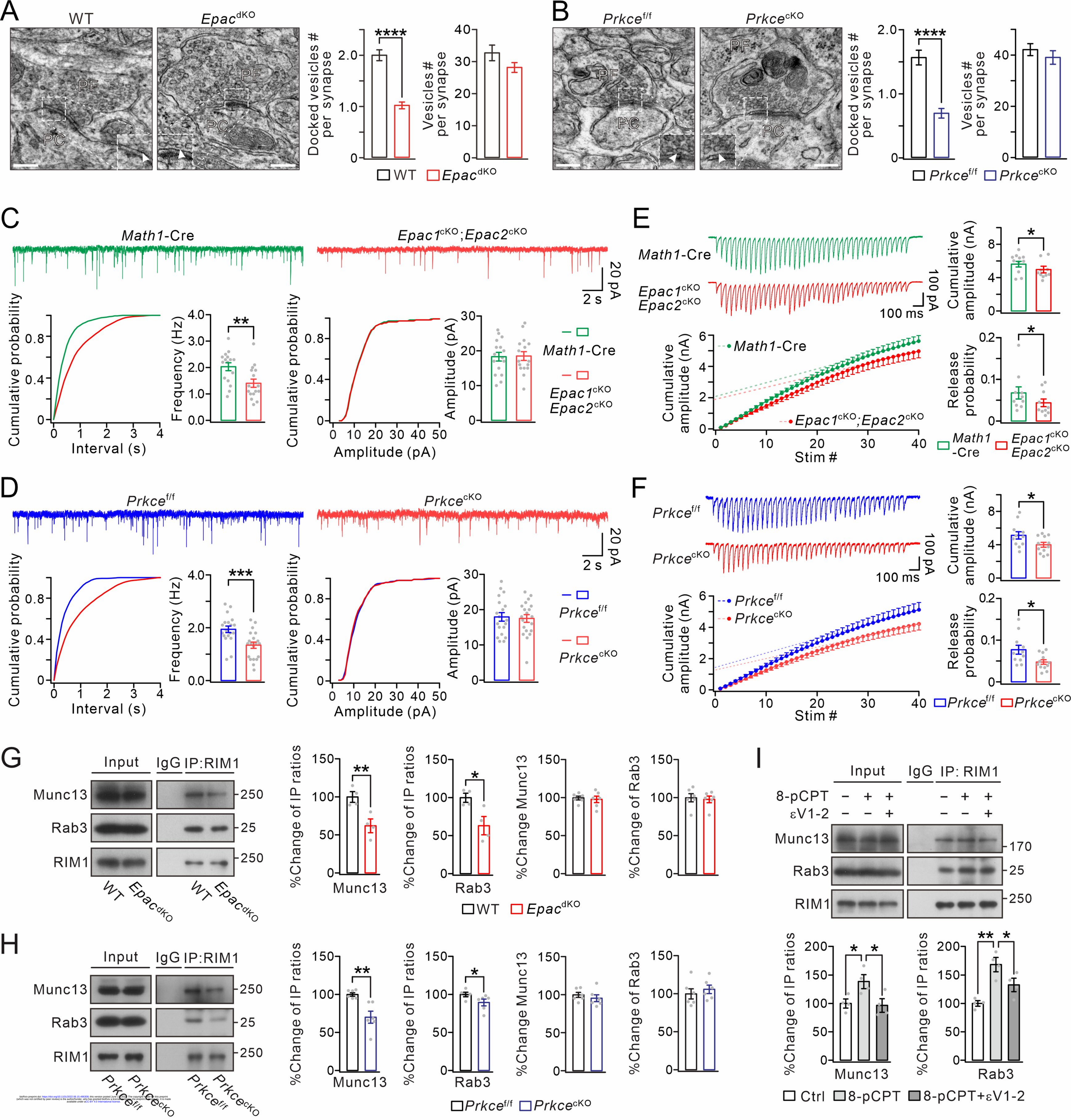

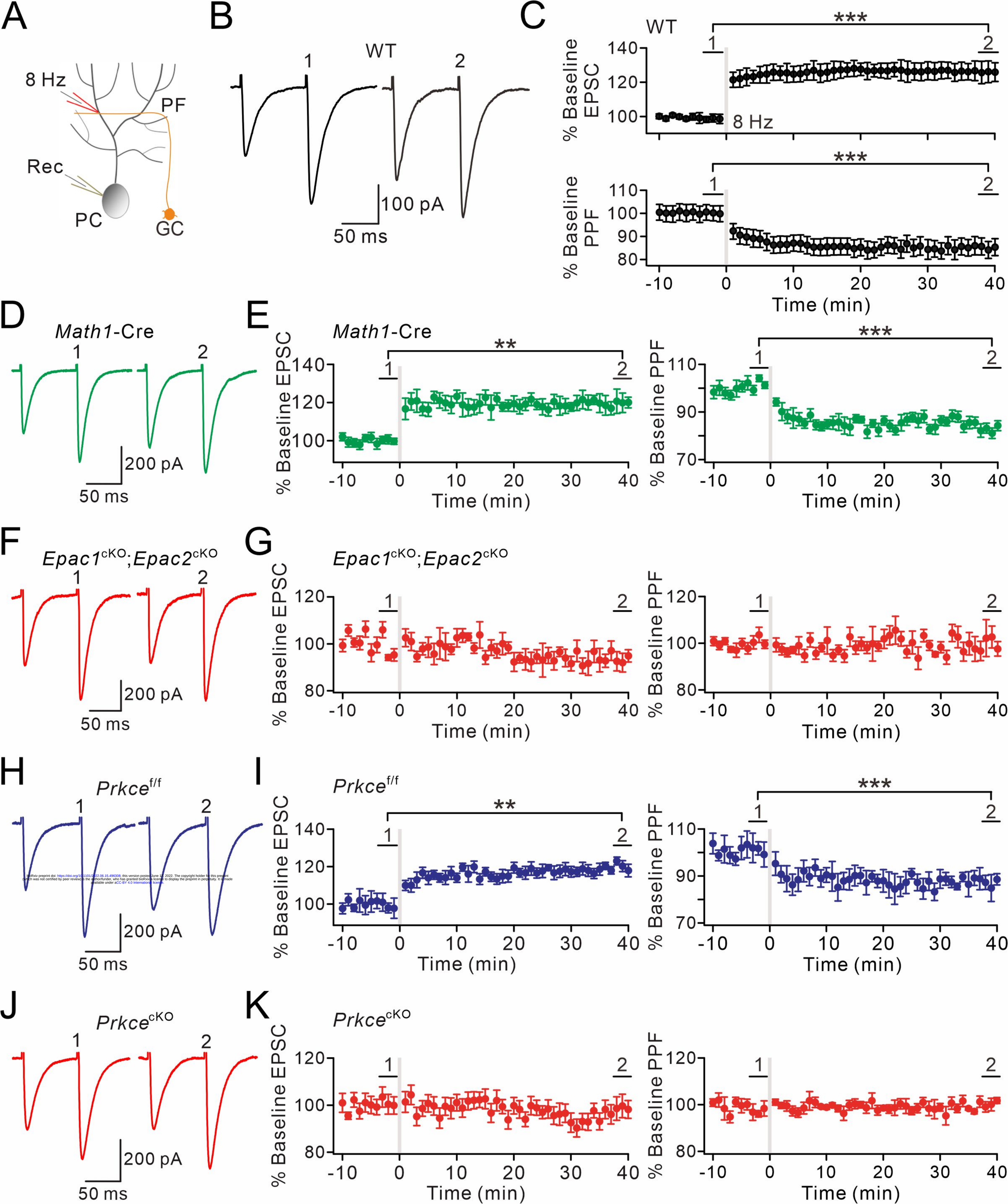

A

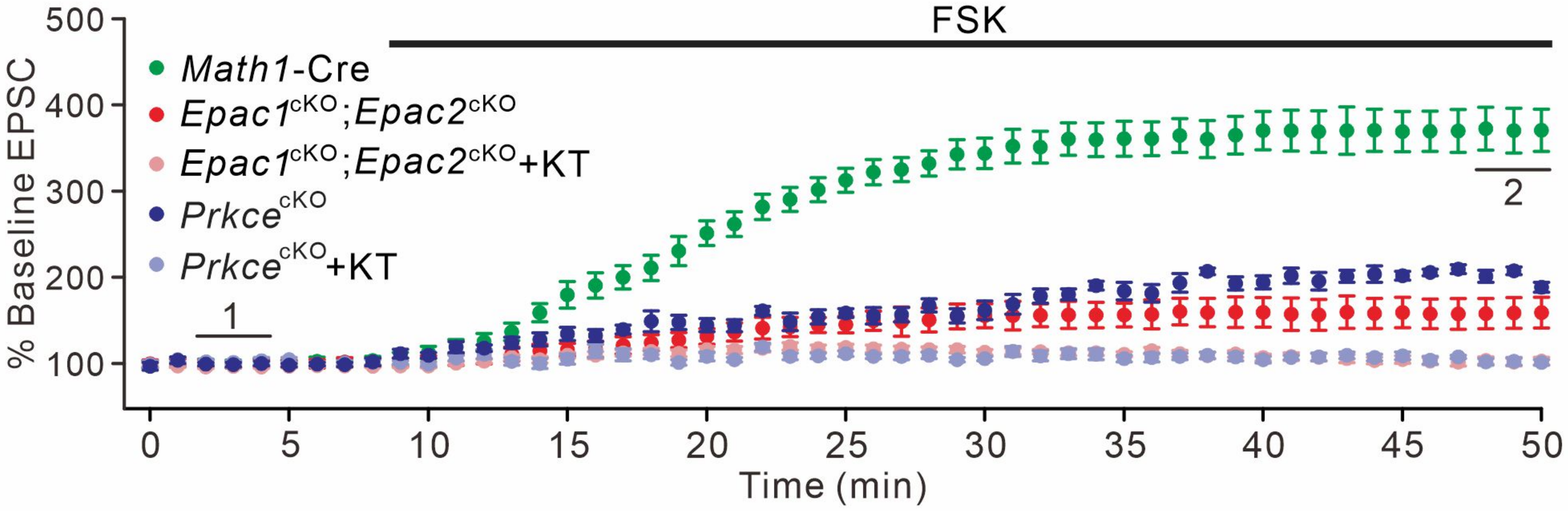

B

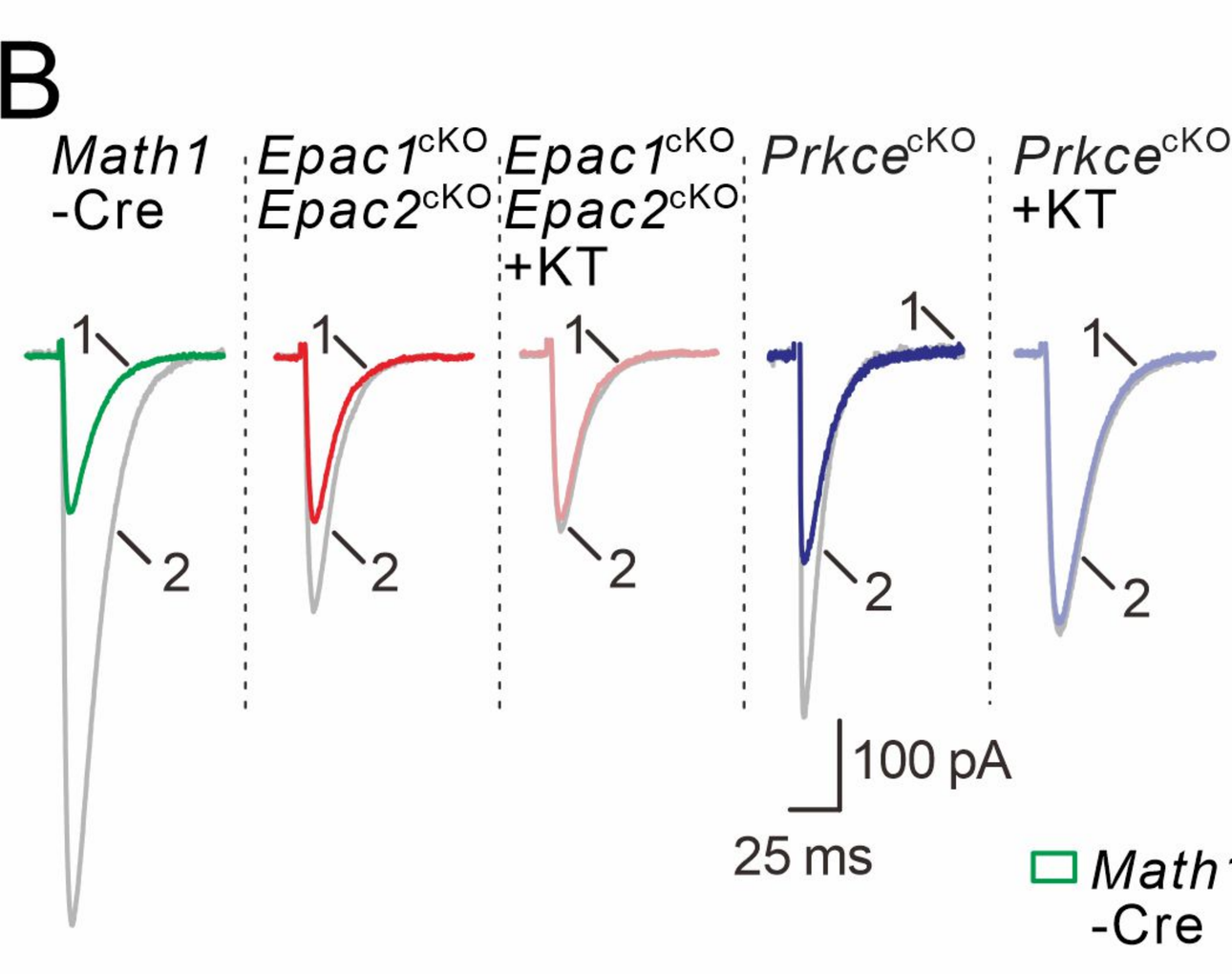

C

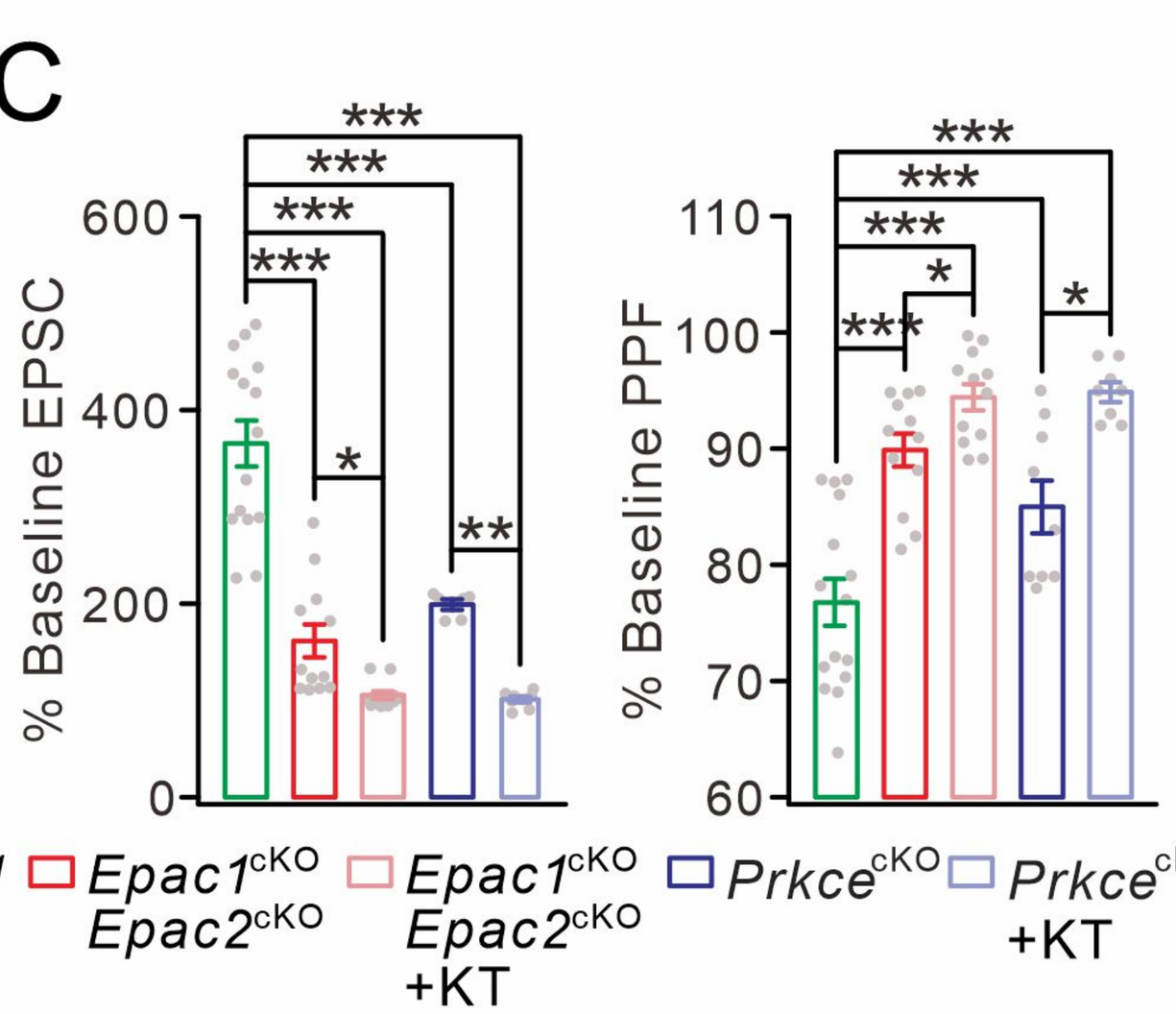

D

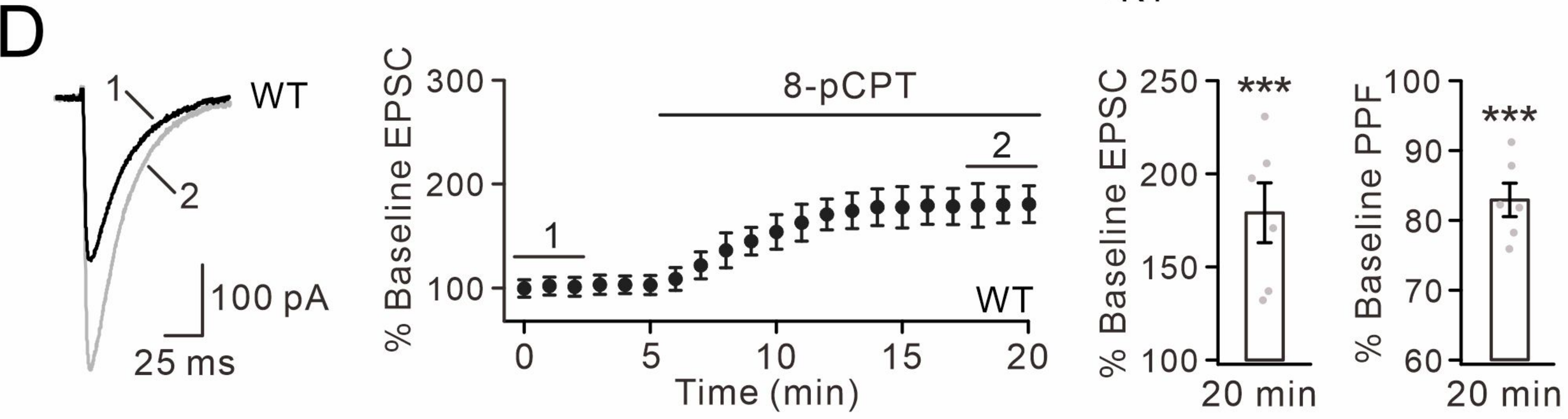

E

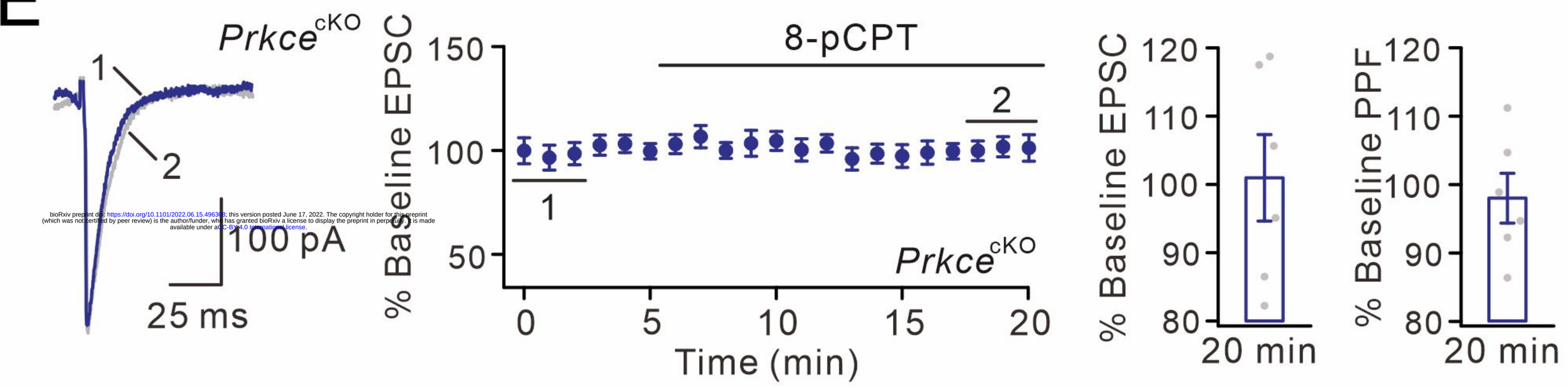

F

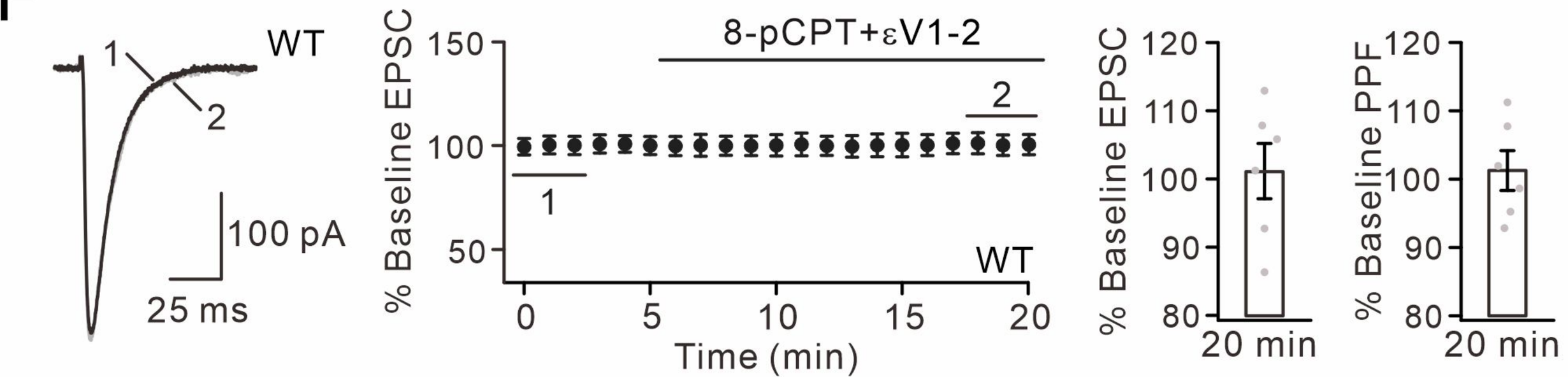

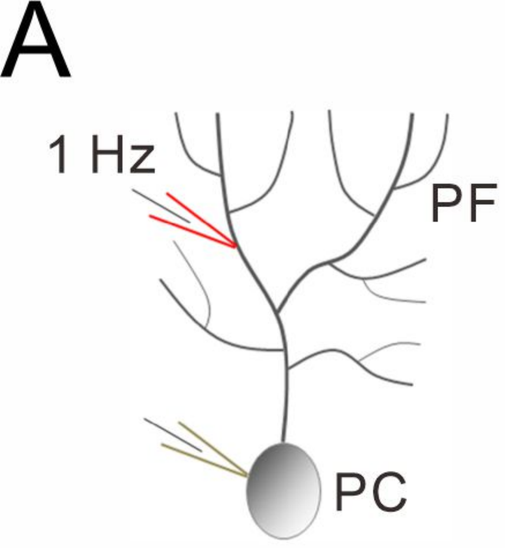

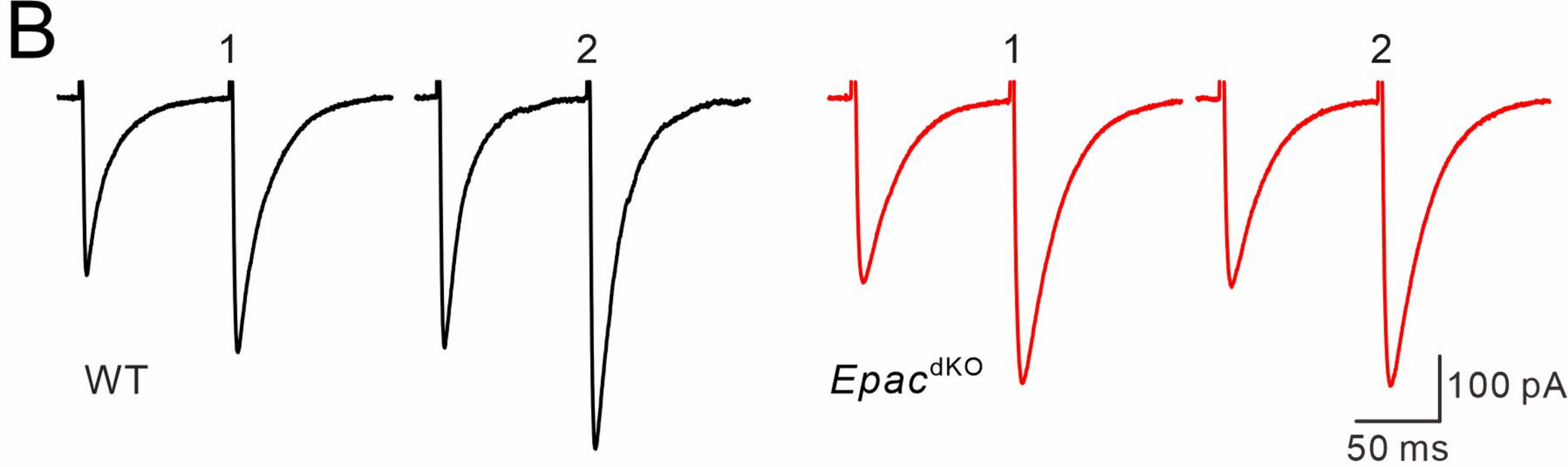

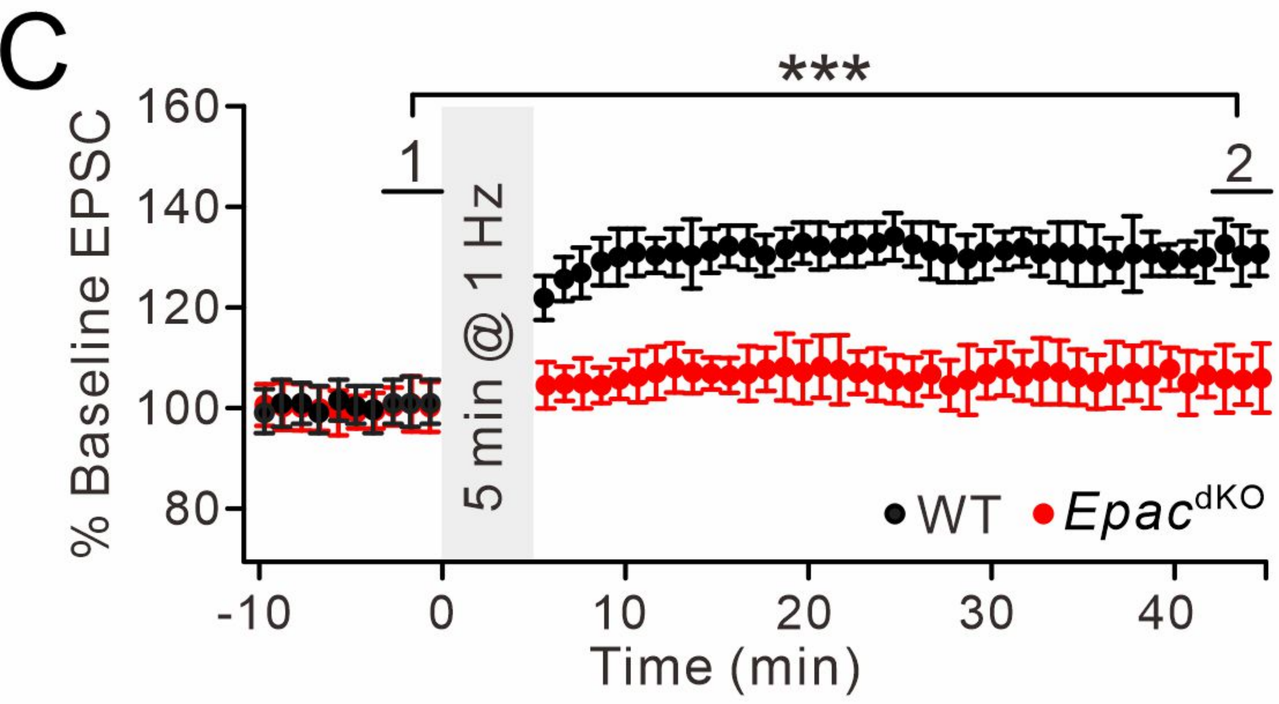

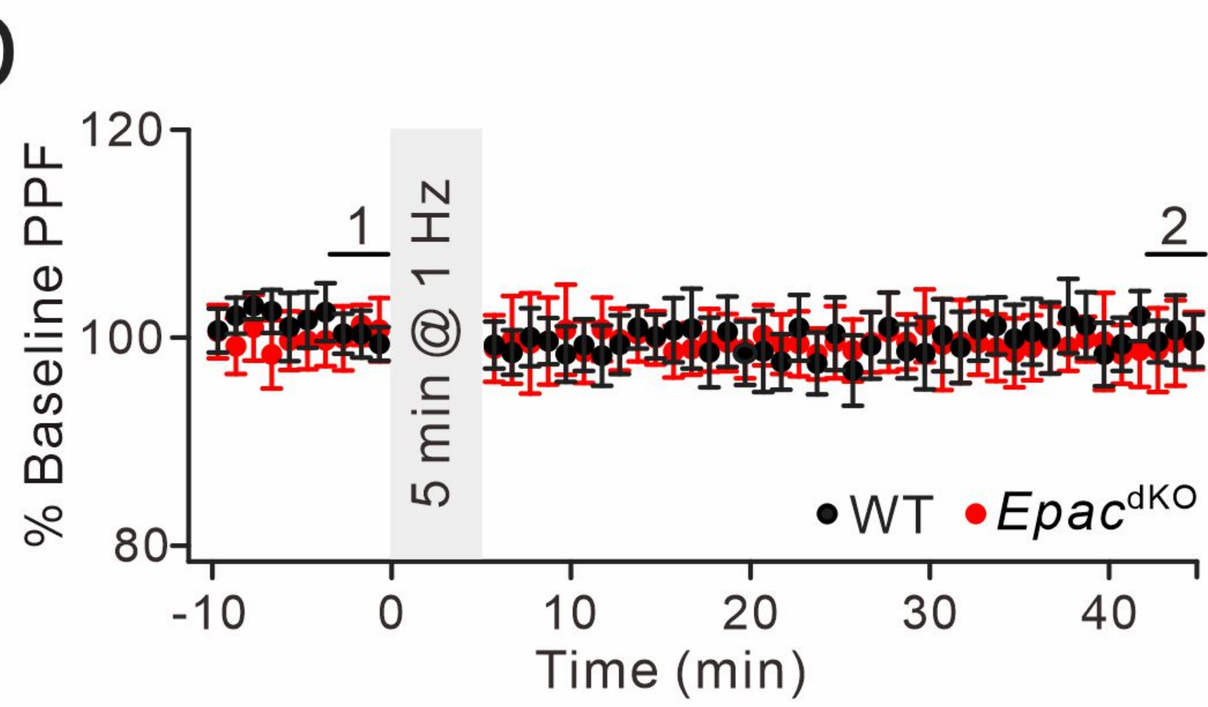

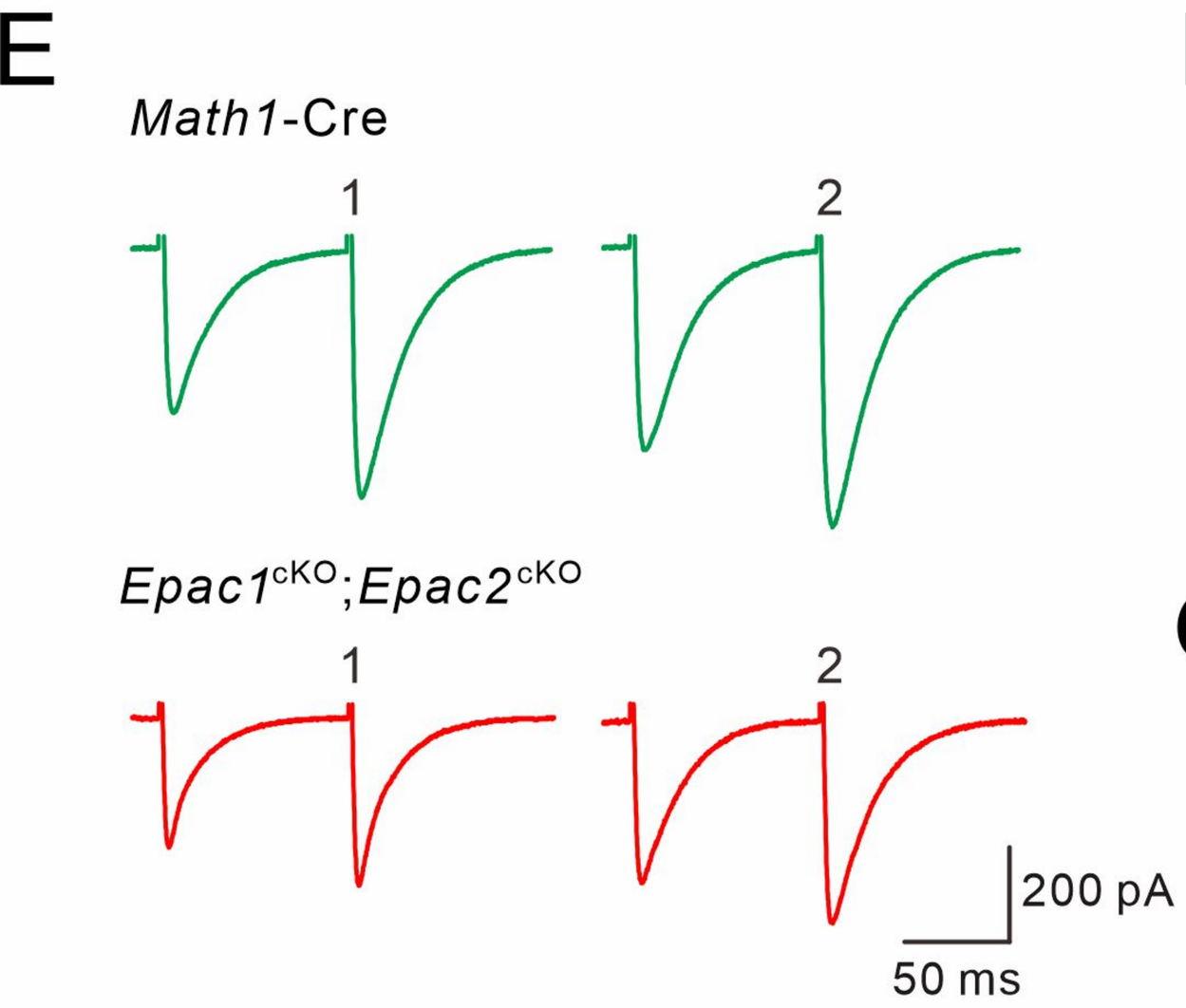

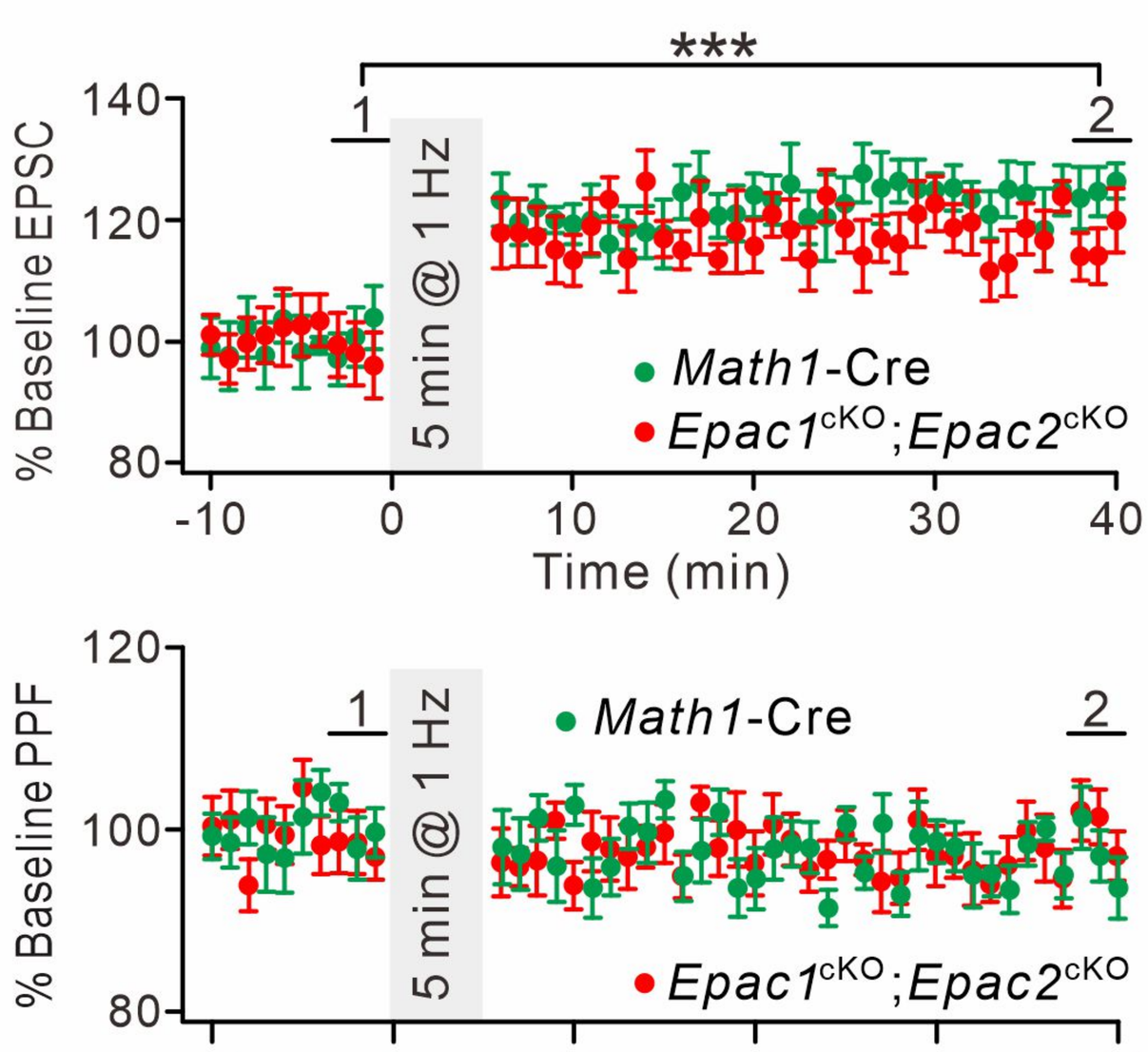

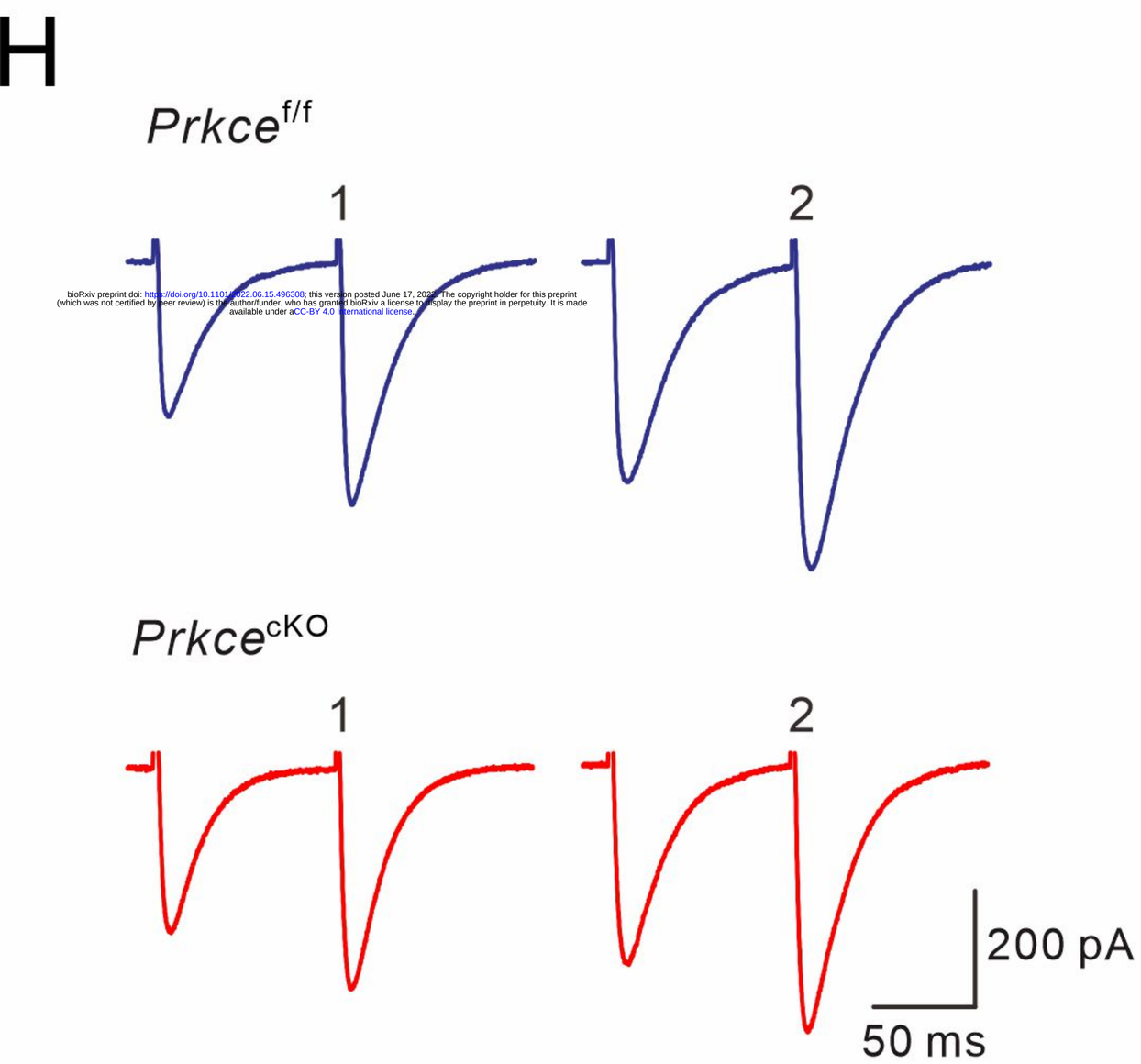

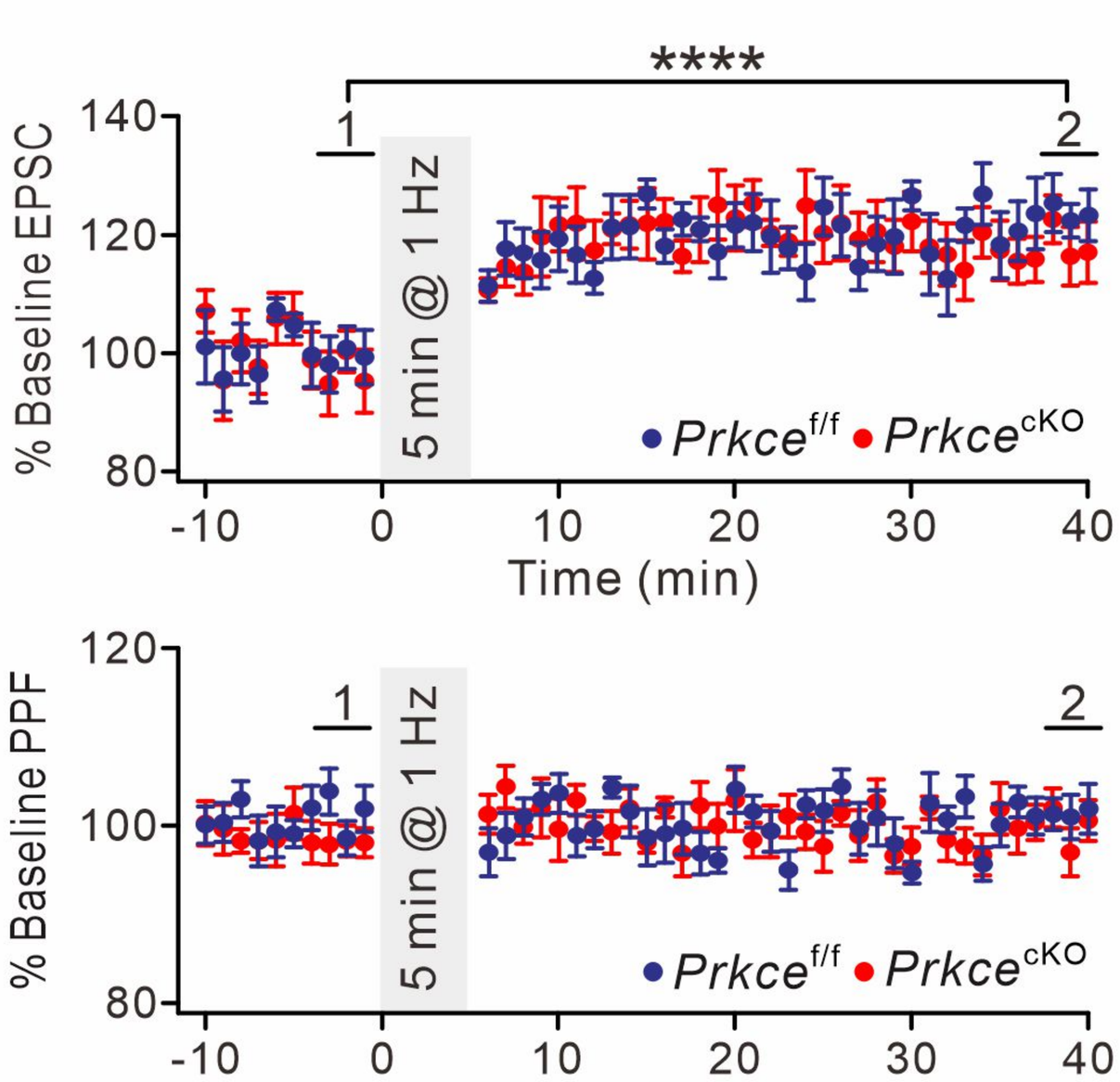

A

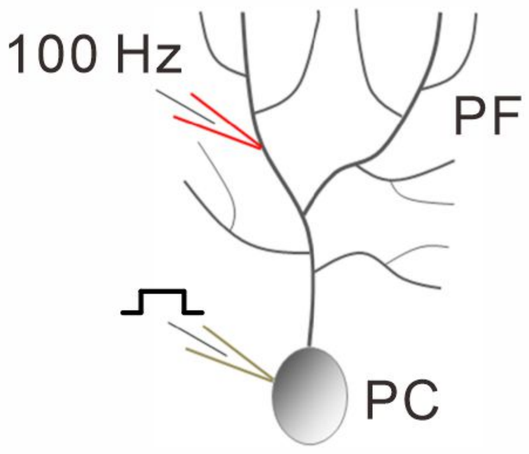

B

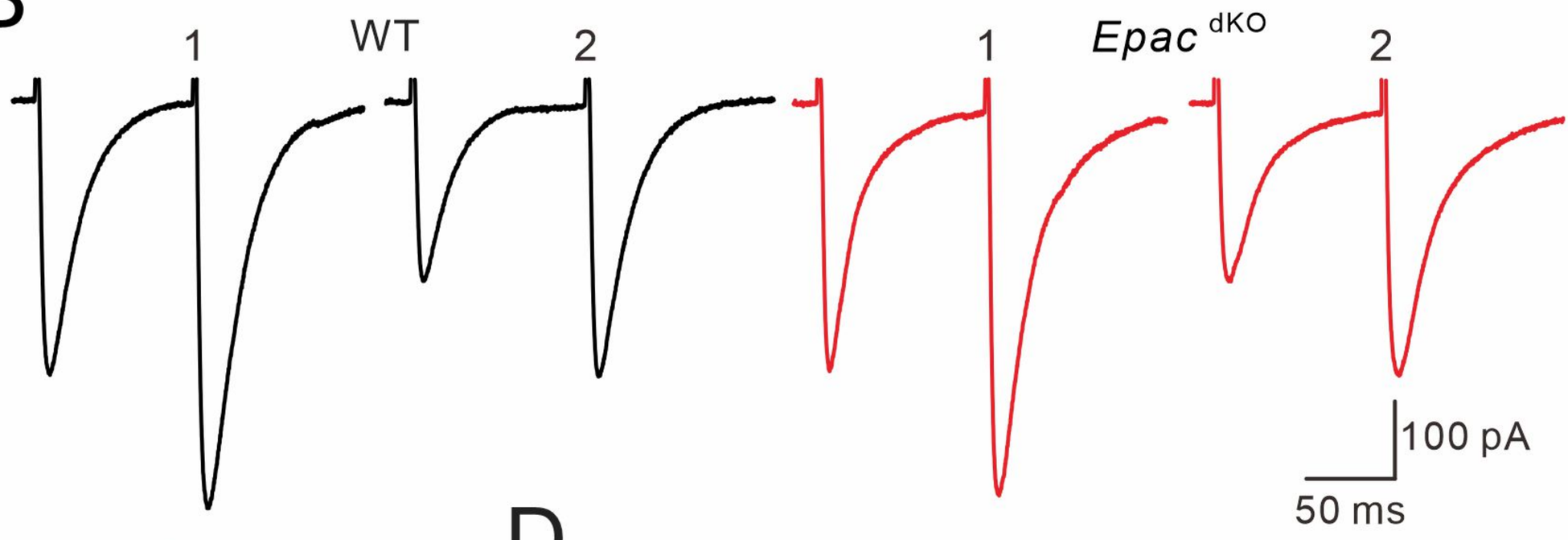

C

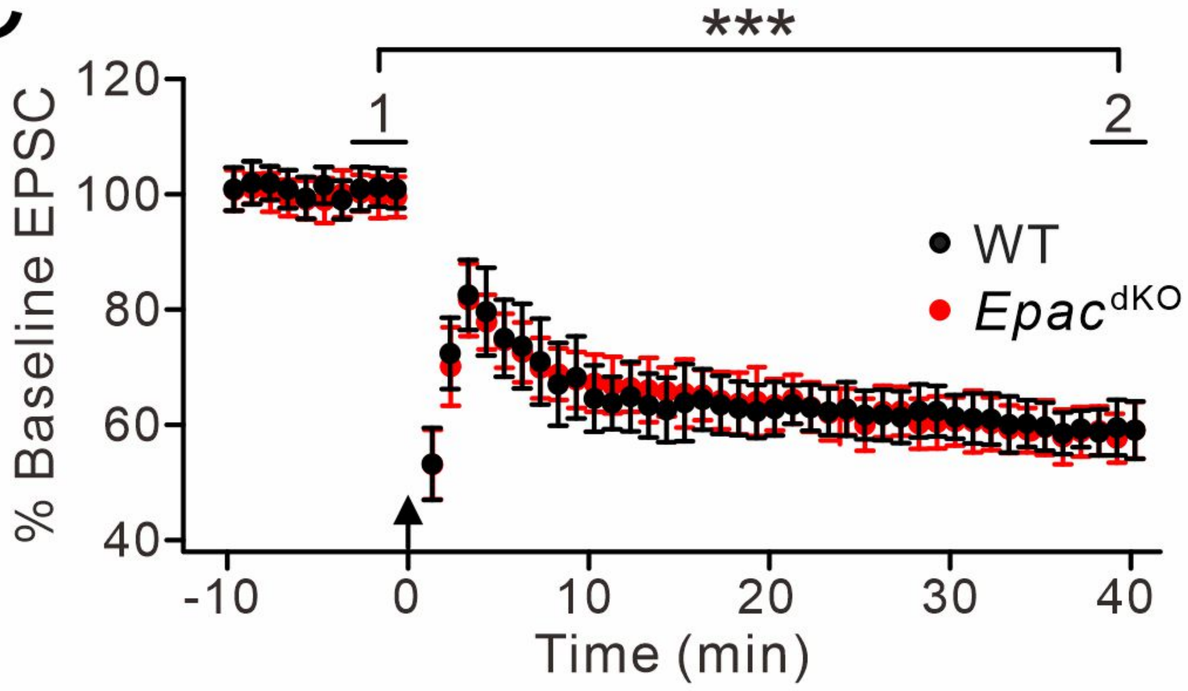

D

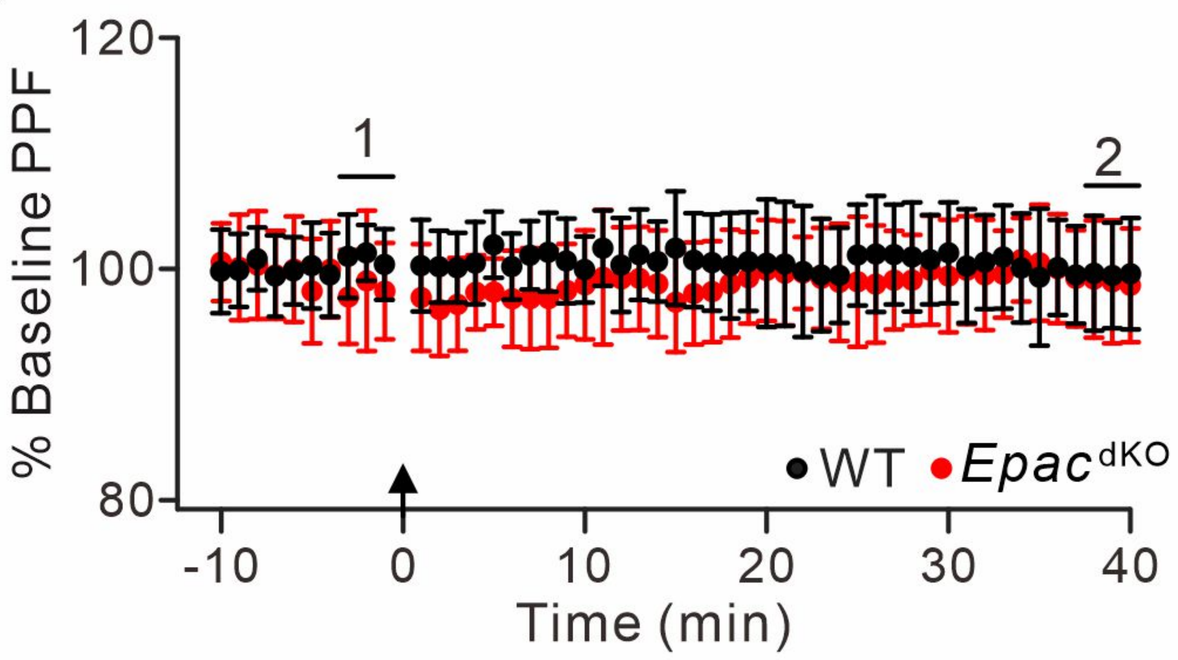

E

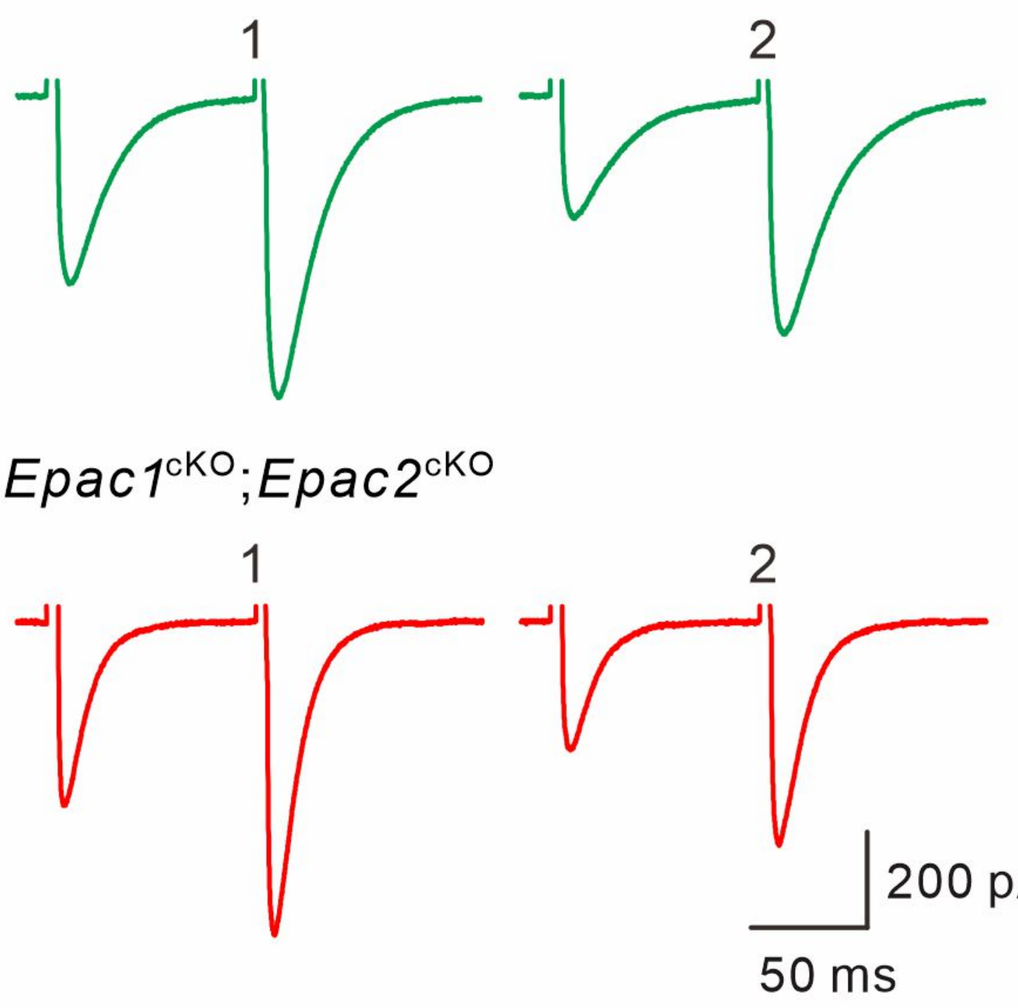

F

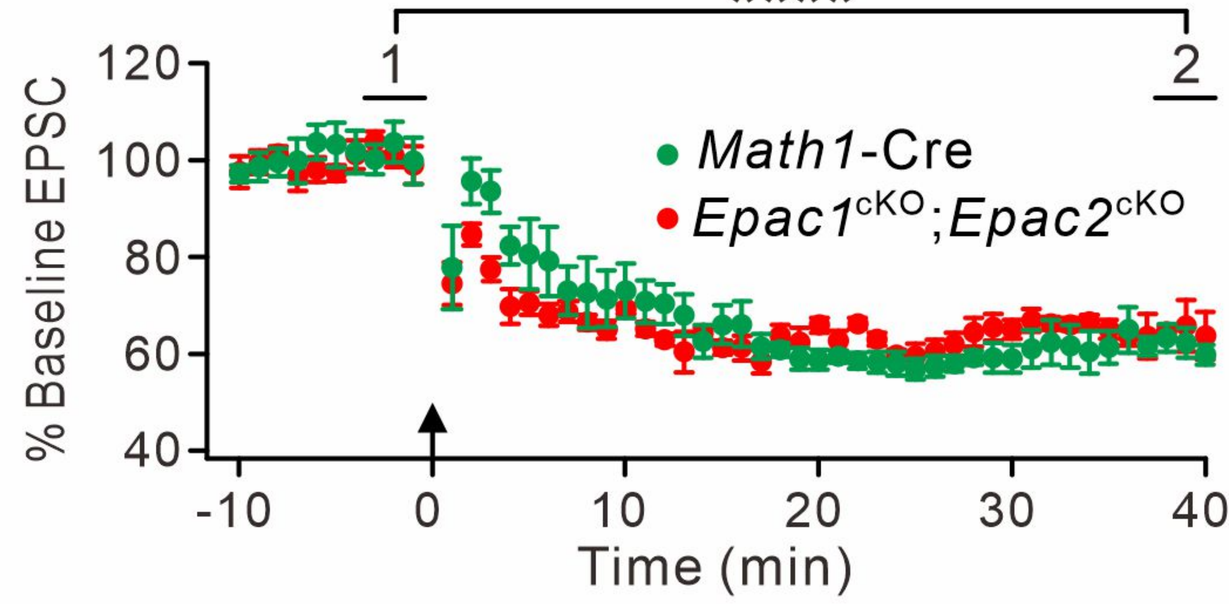

G

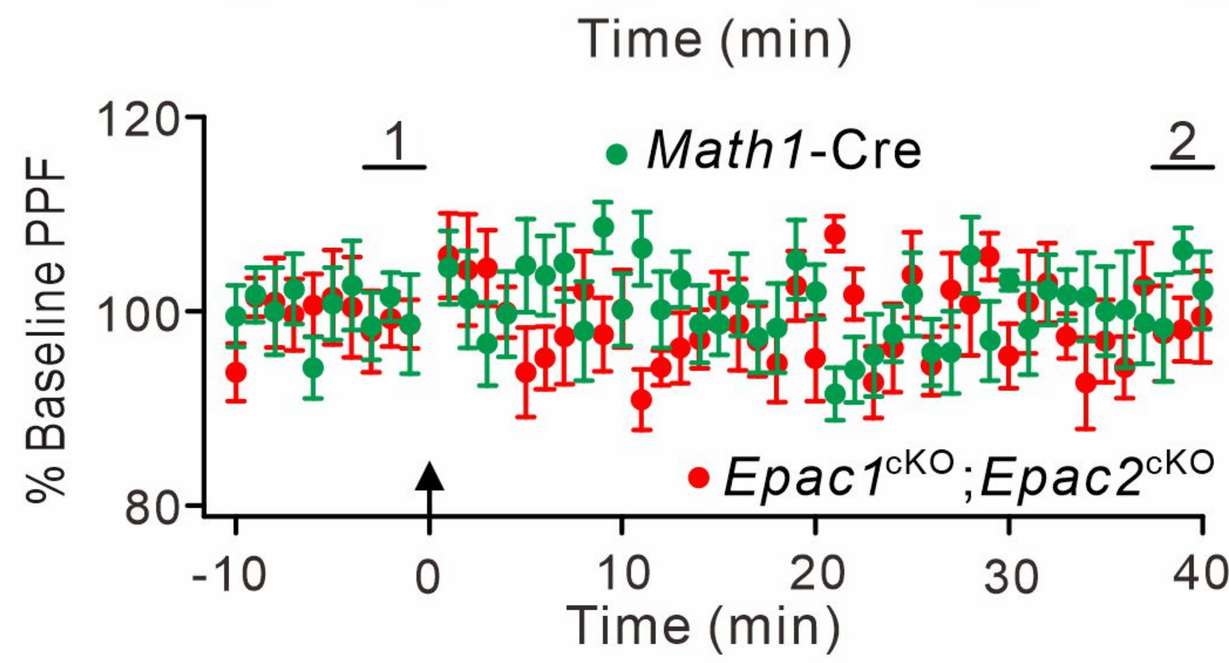

H

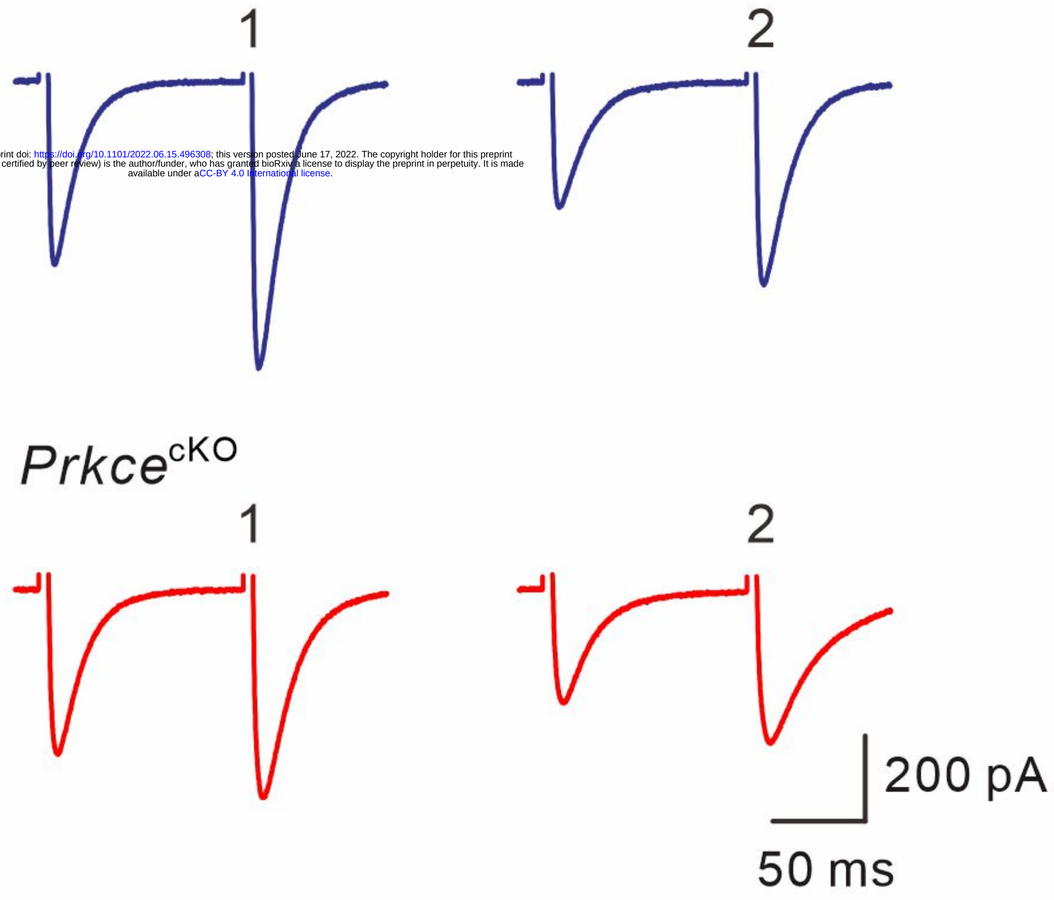

I

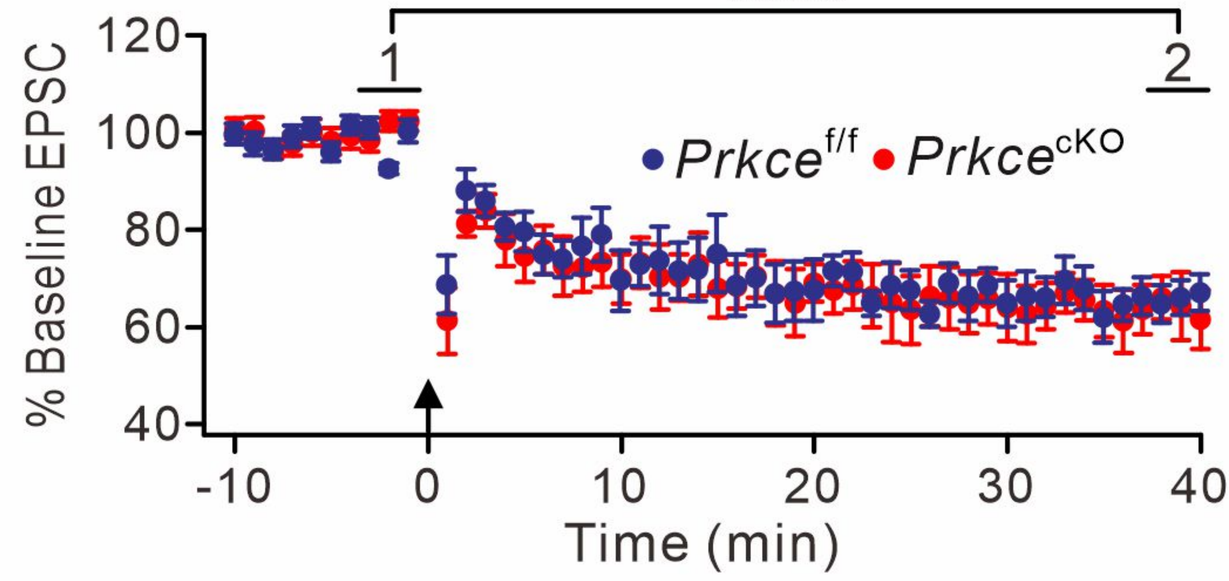

J

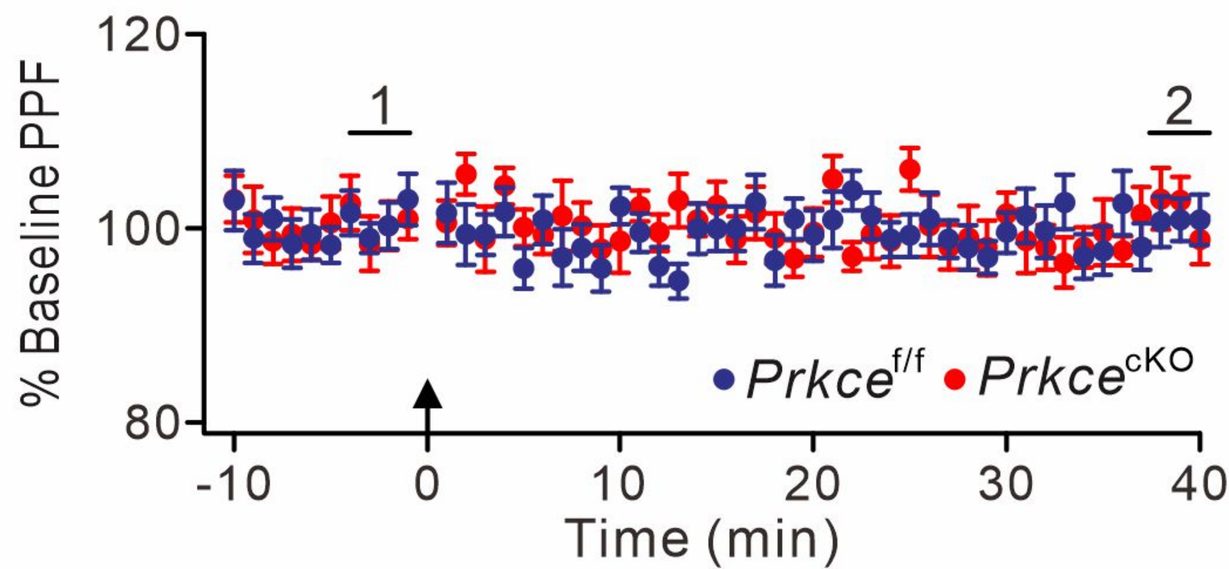

A

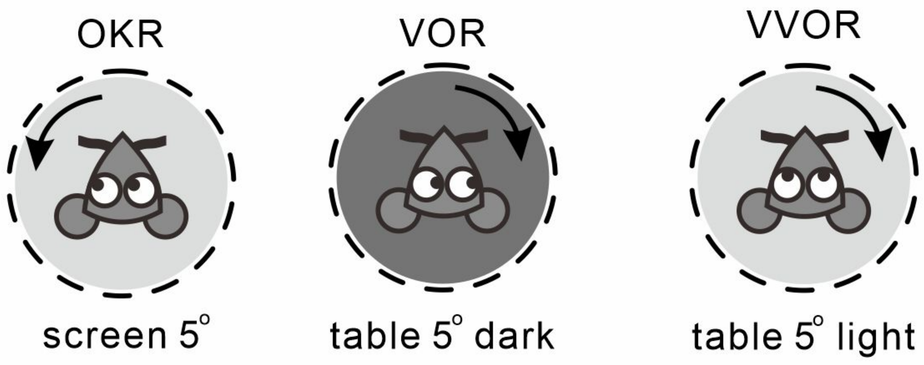

B

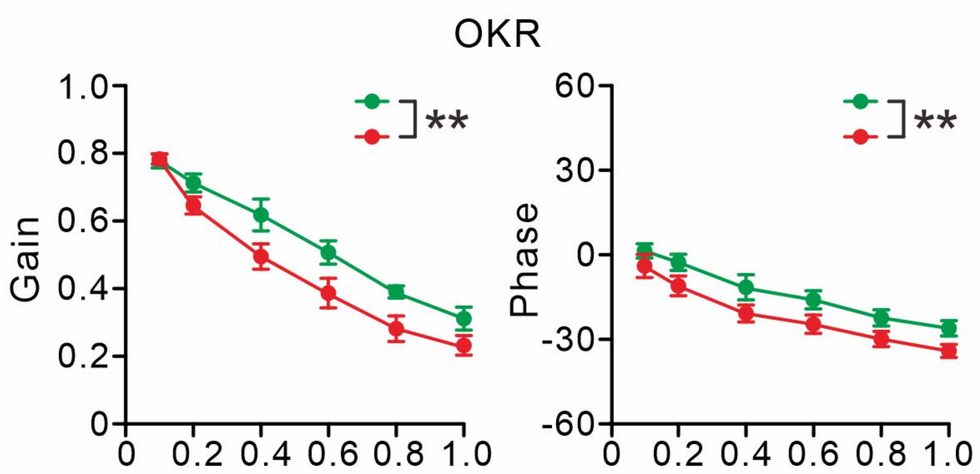

C

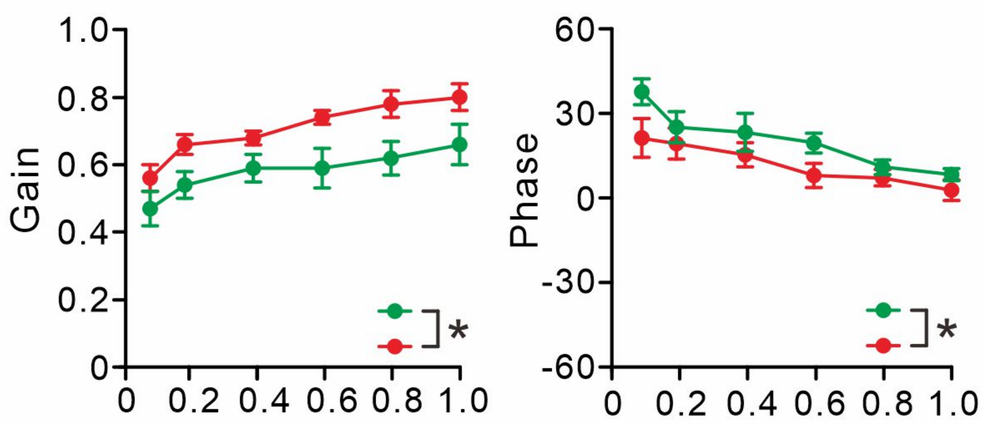

D

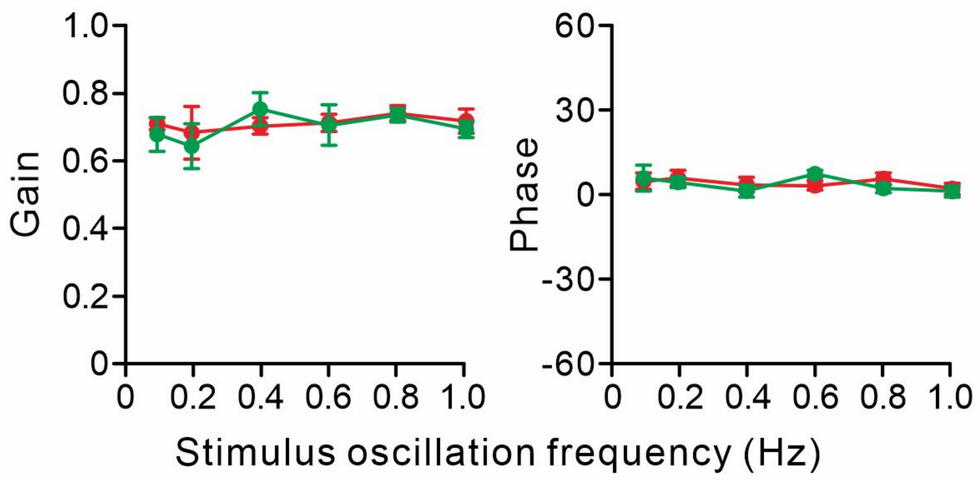

E

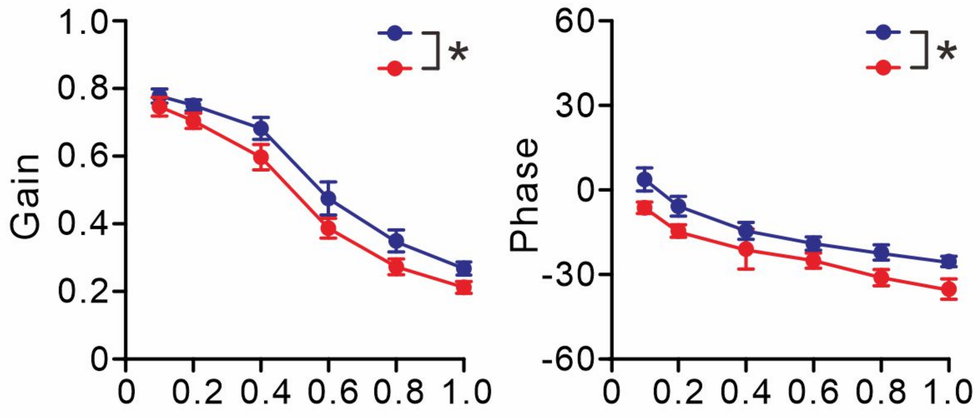

F

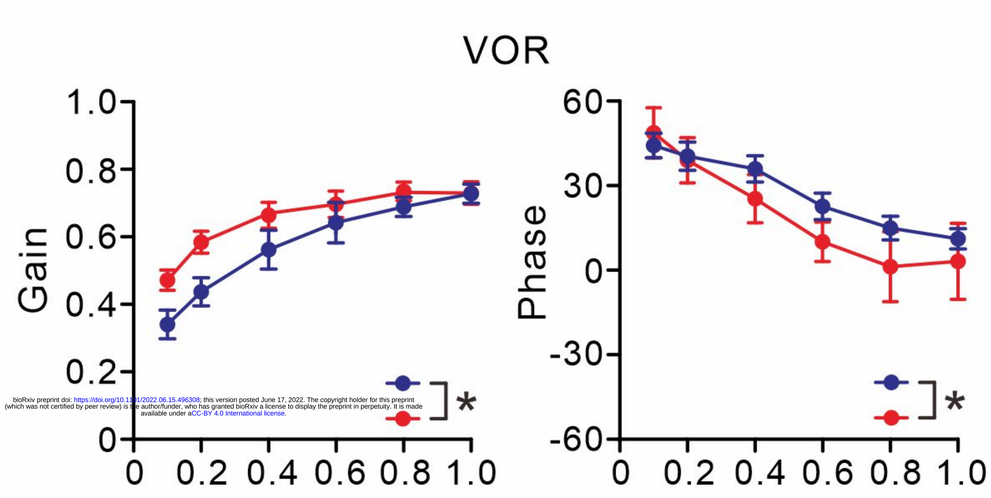

G

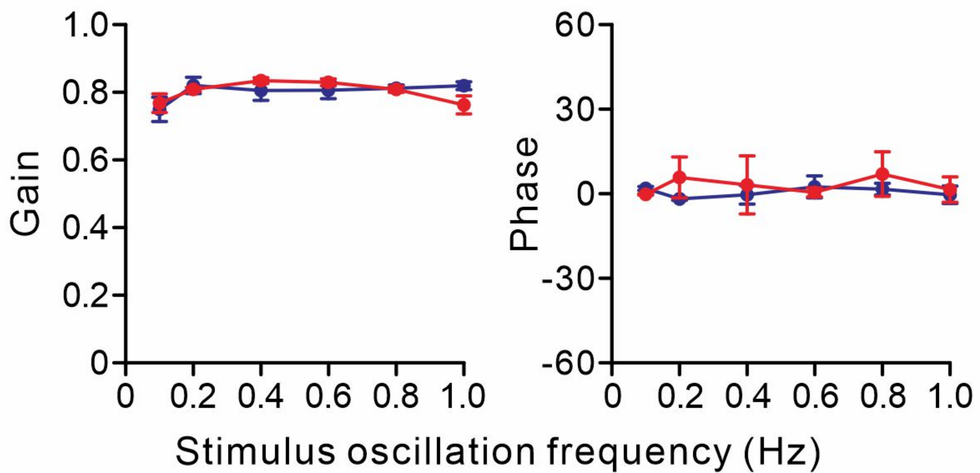

H

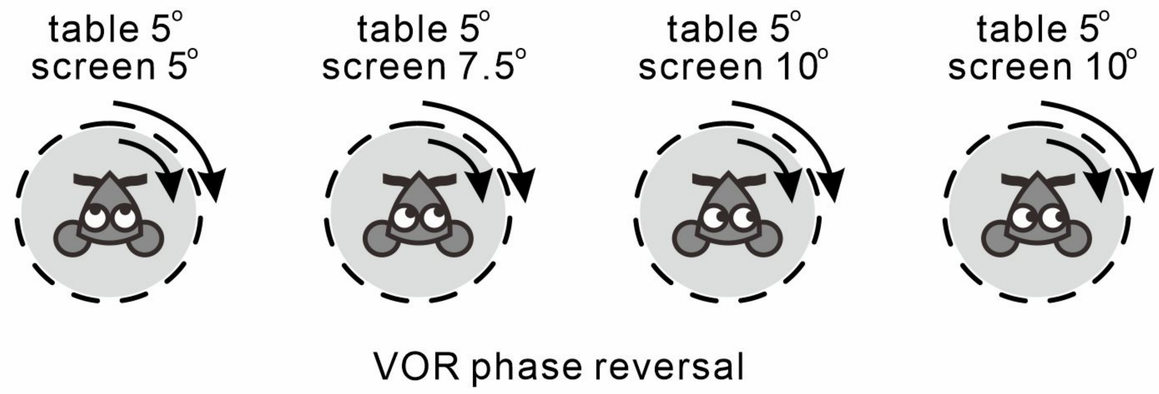

I

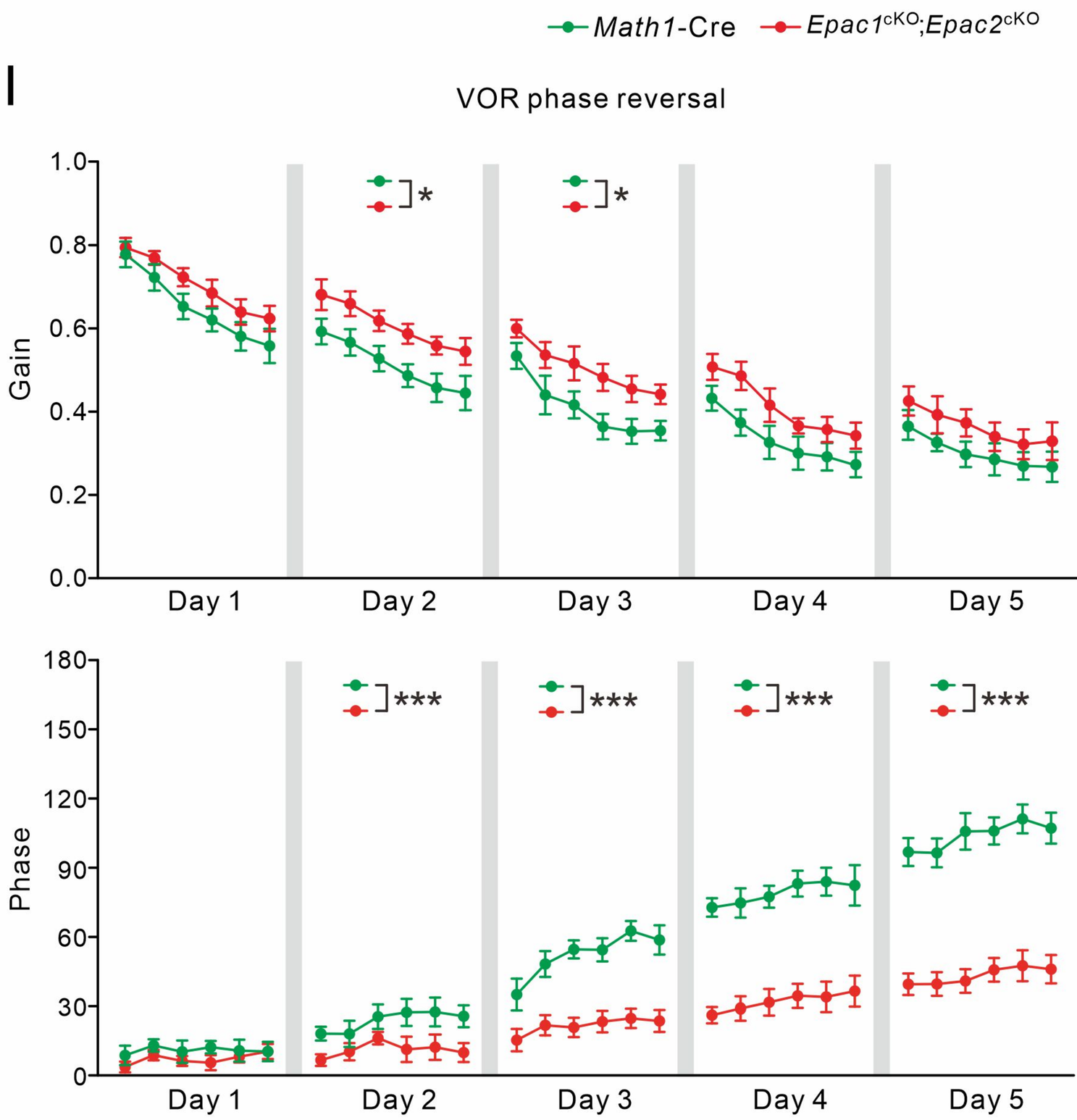

J

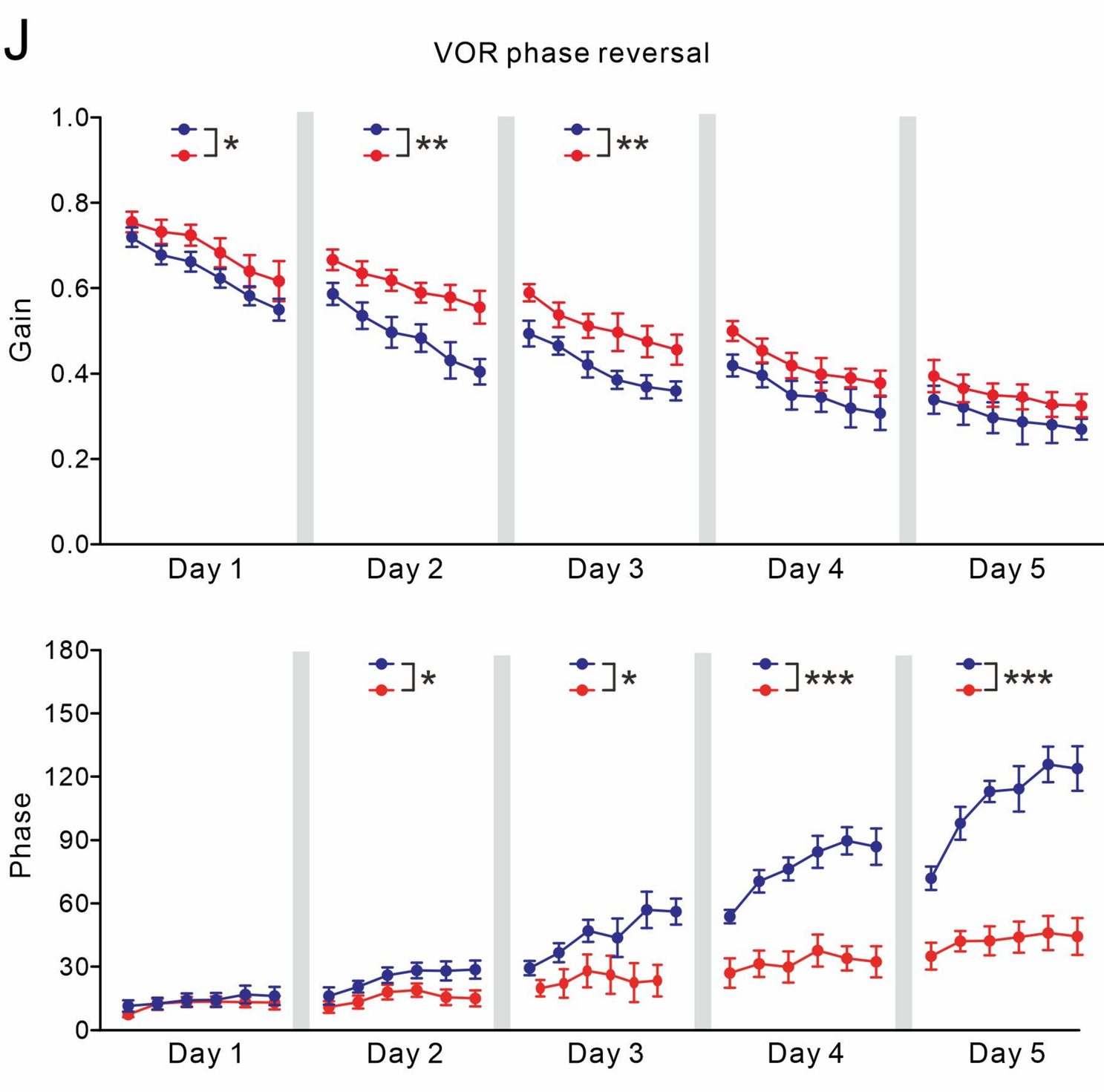

A

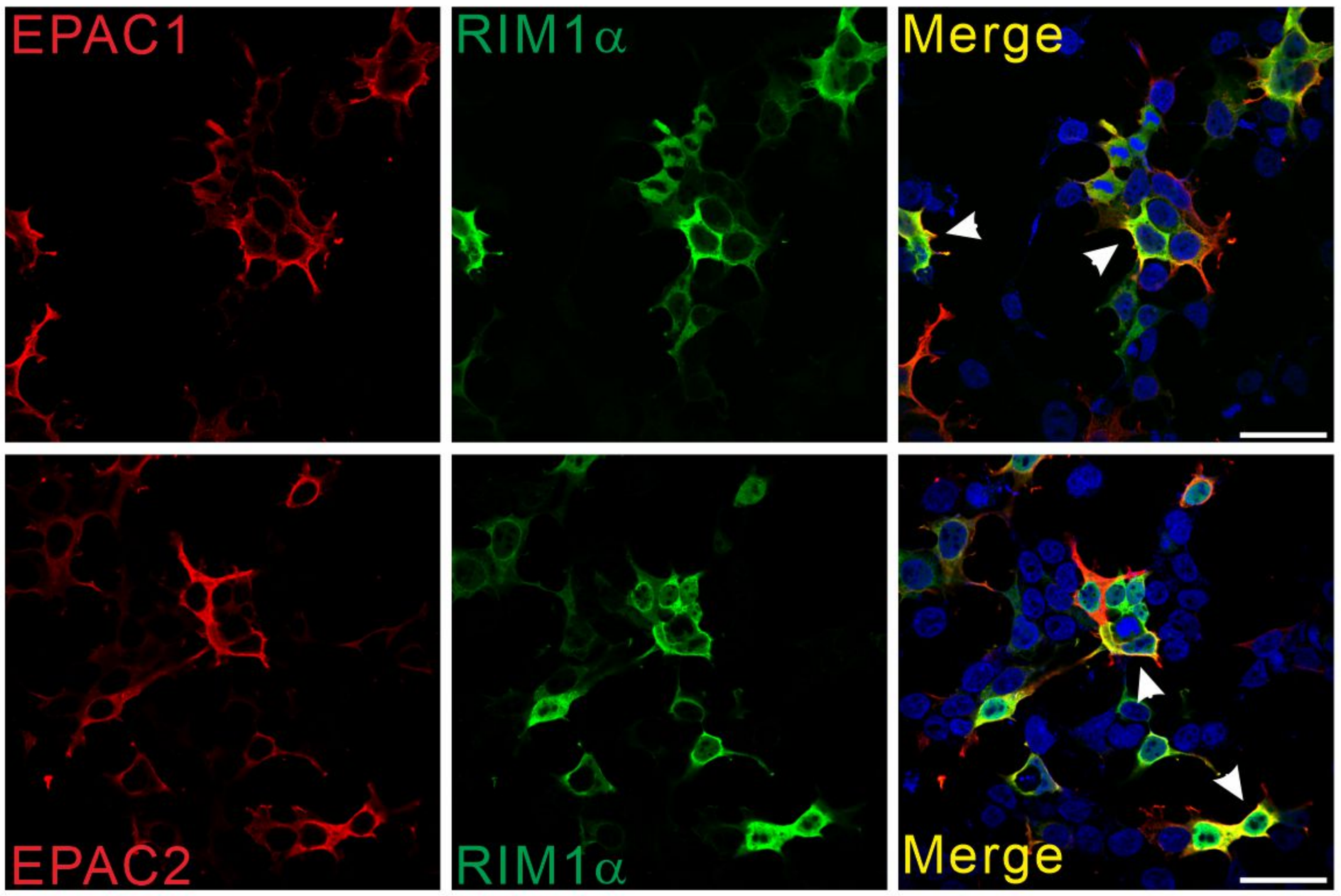

B

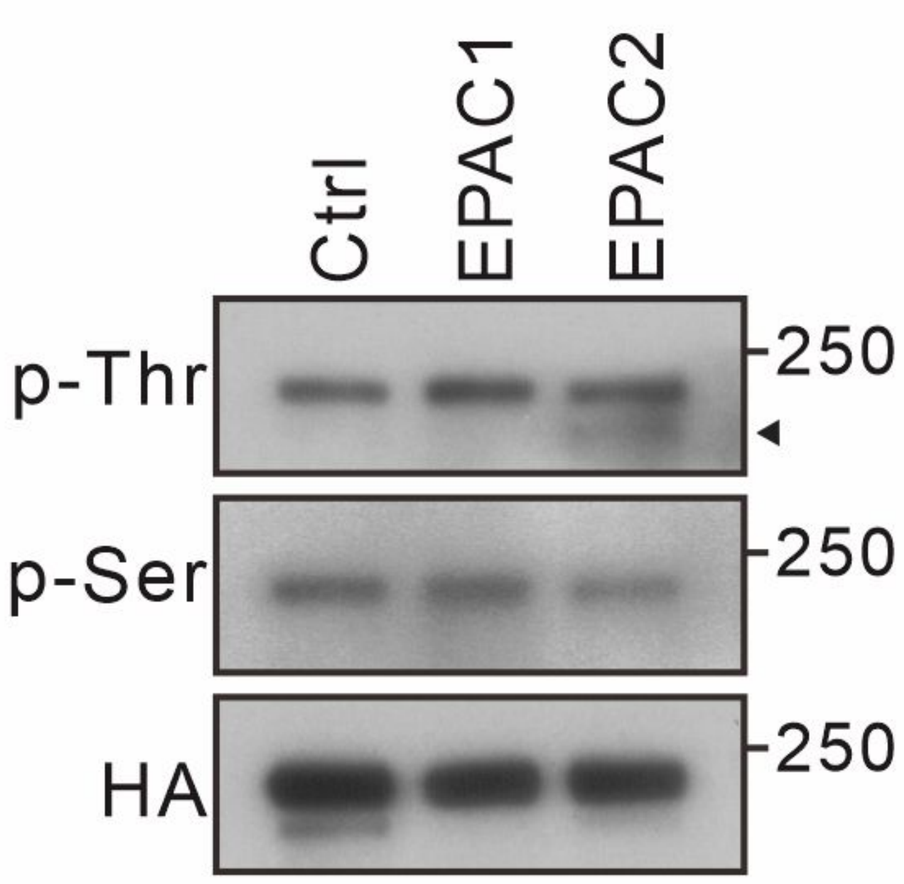

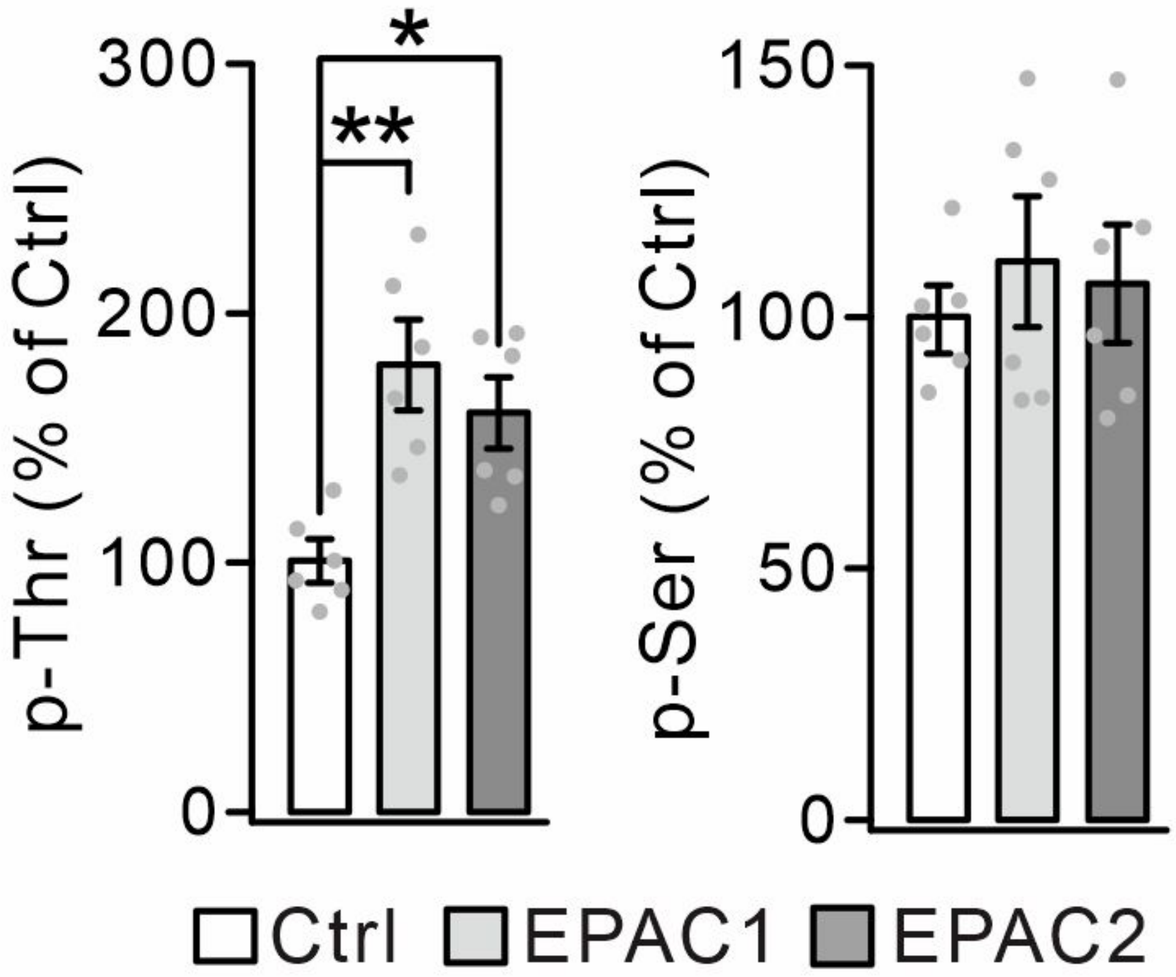

C

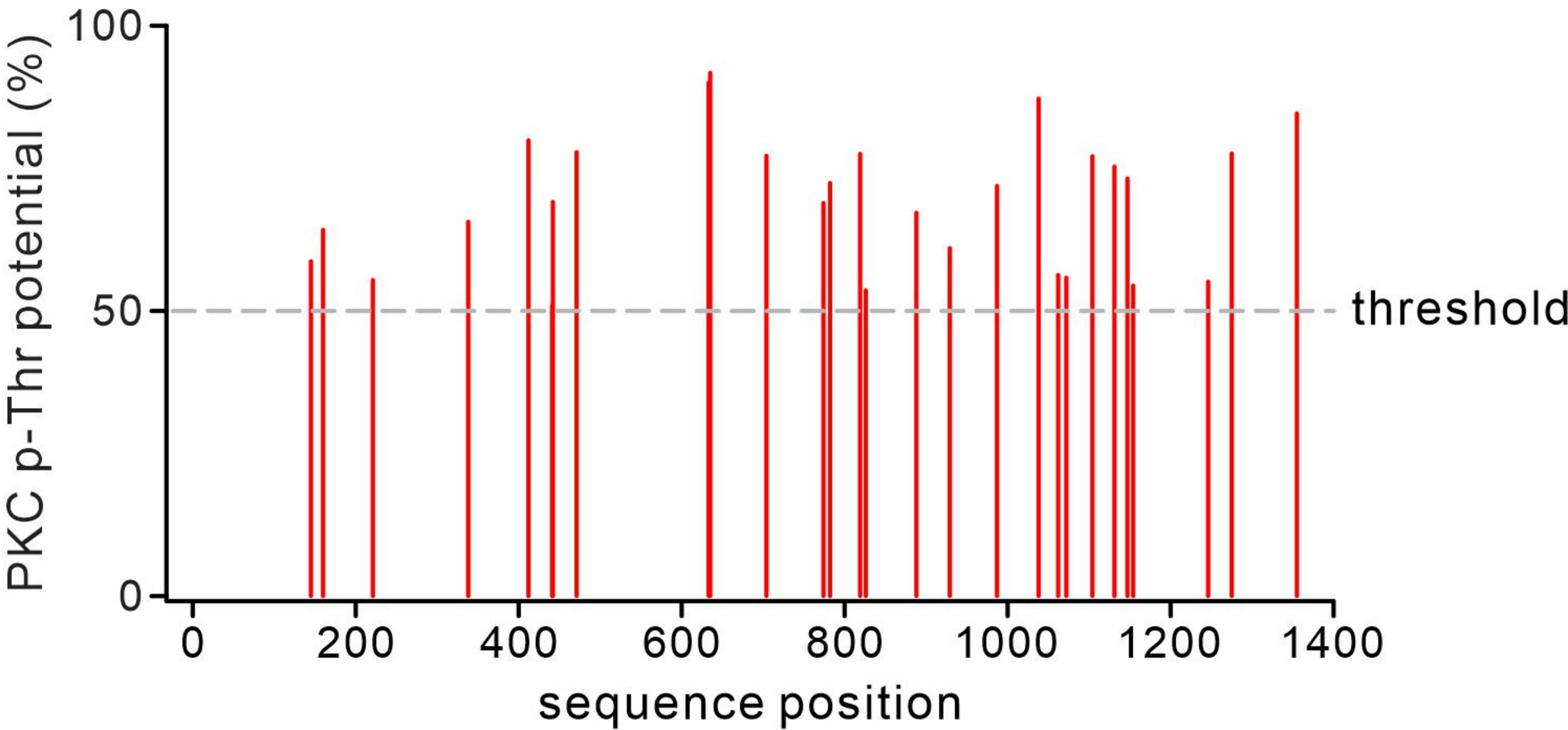

A

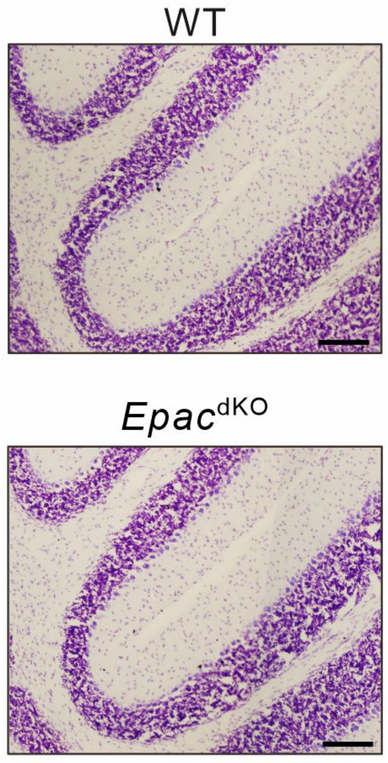

B

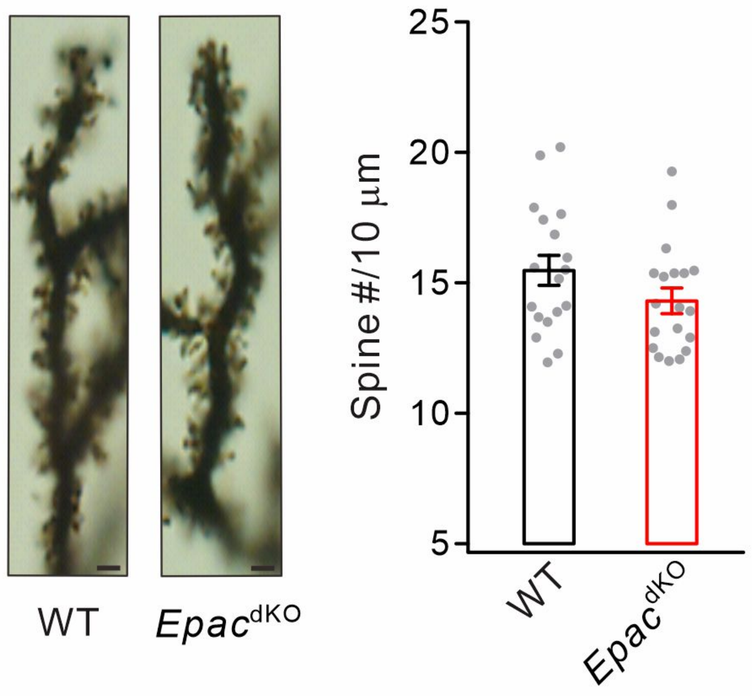

C

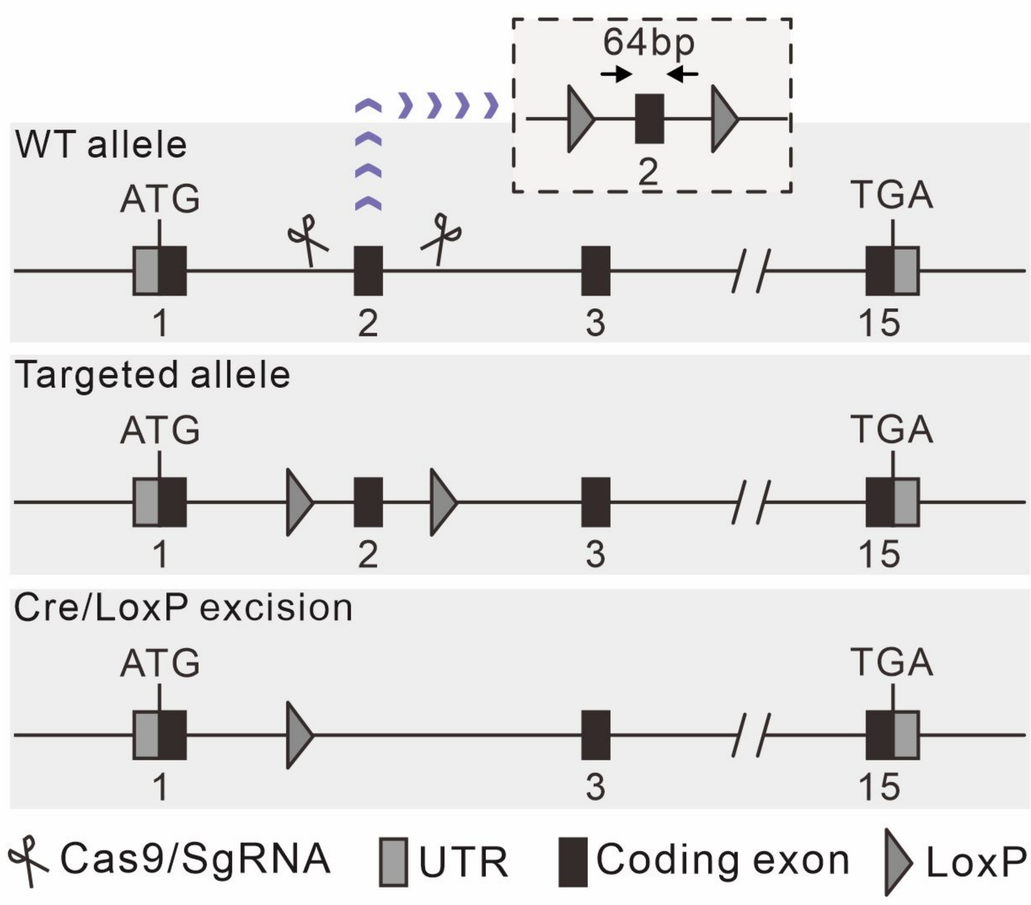

D

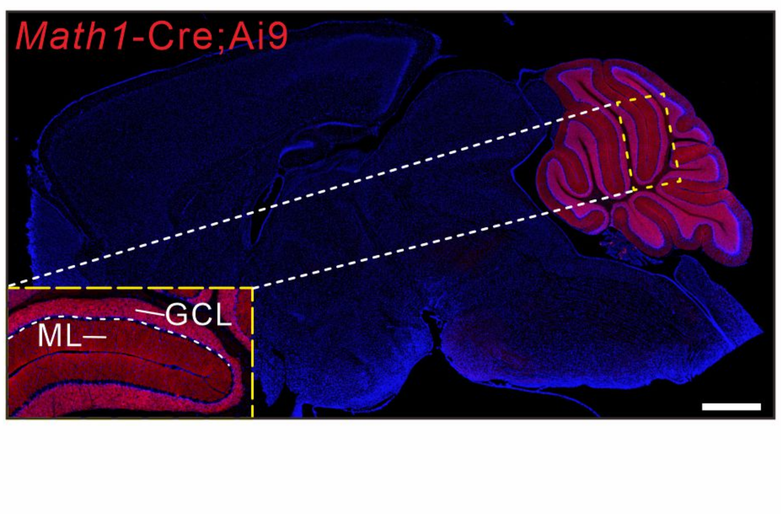

E

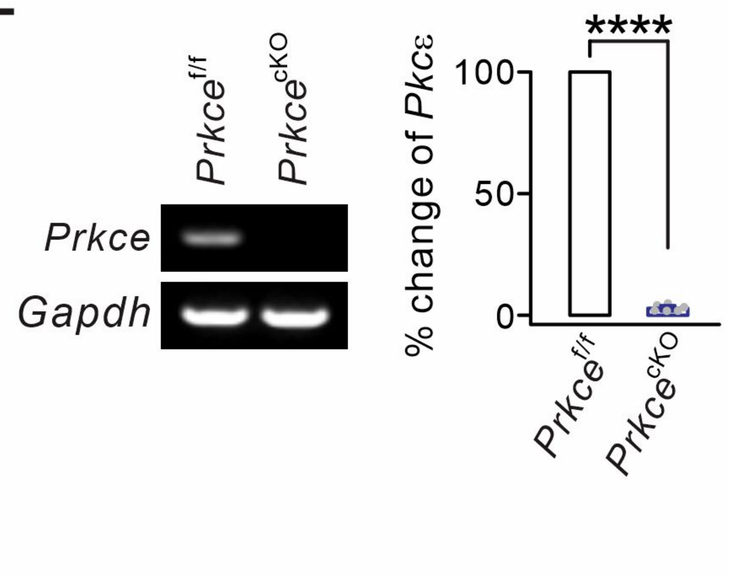

F

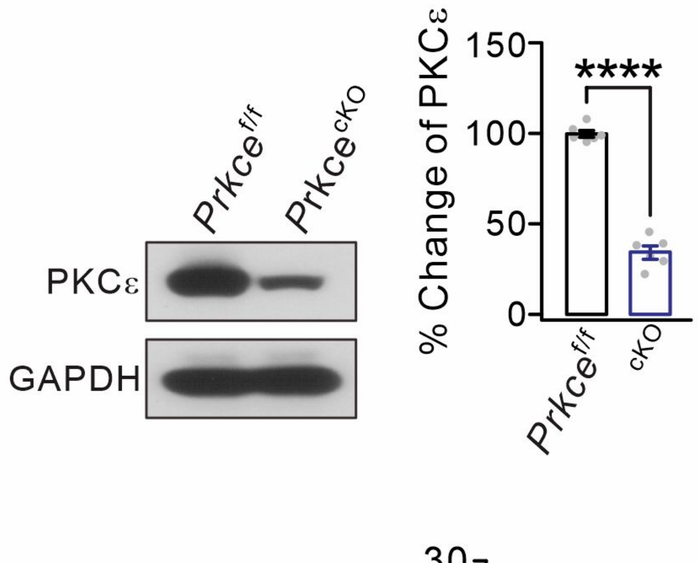

G

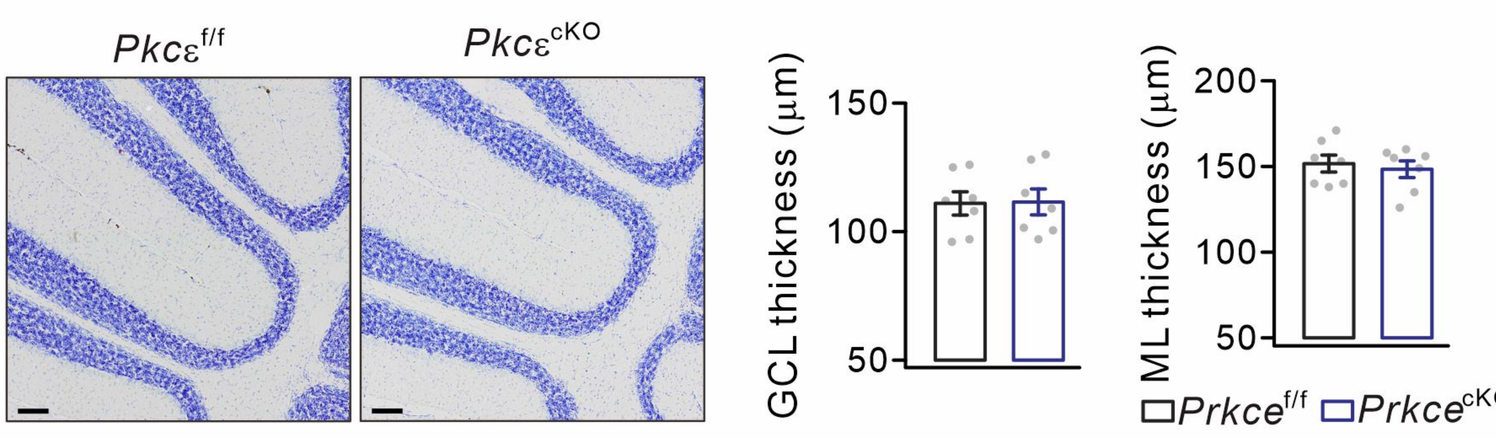

H

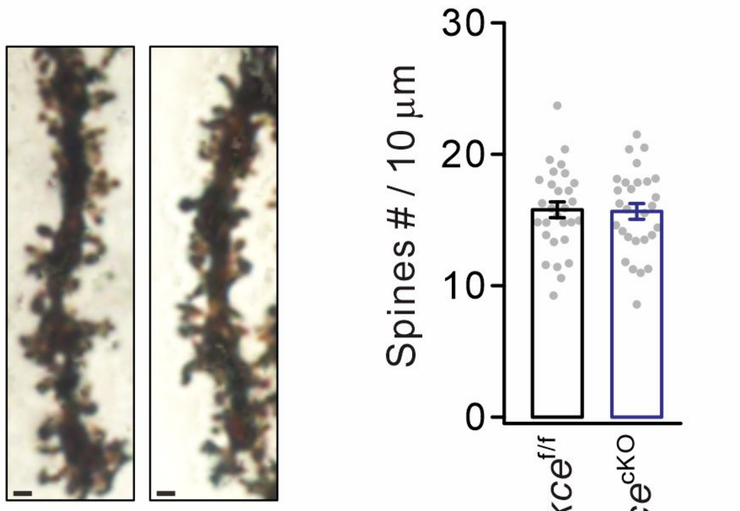

I

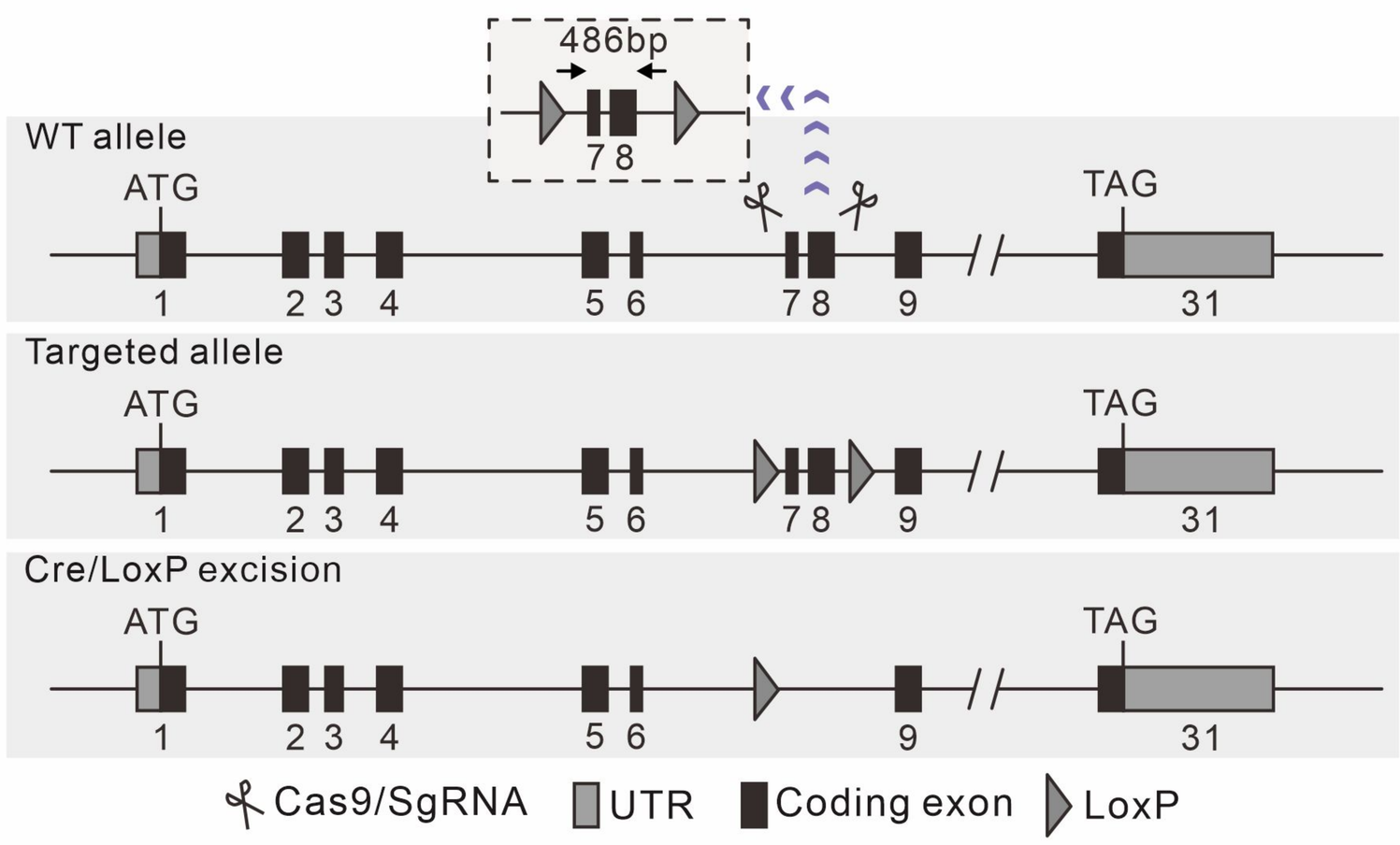

J

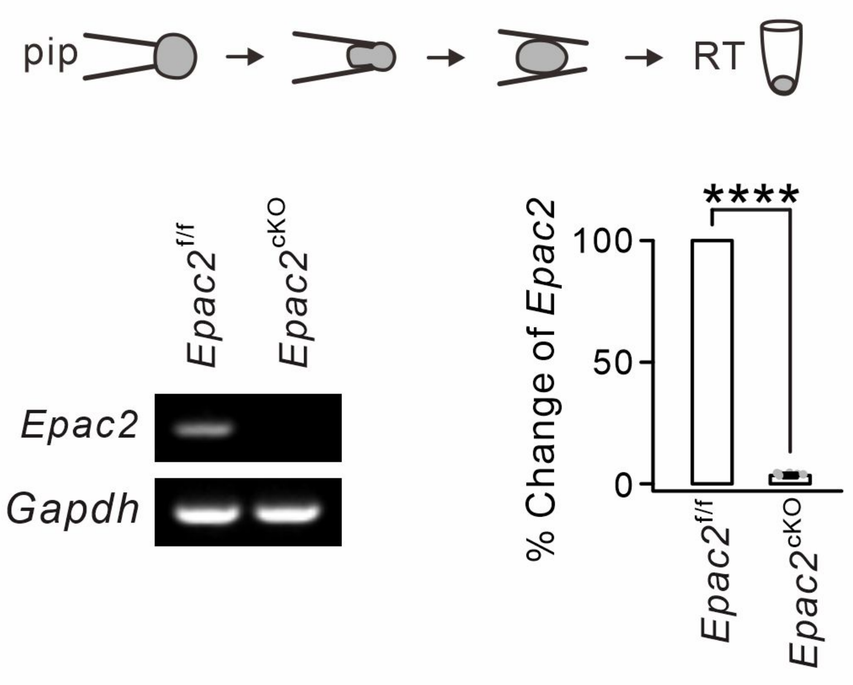

K

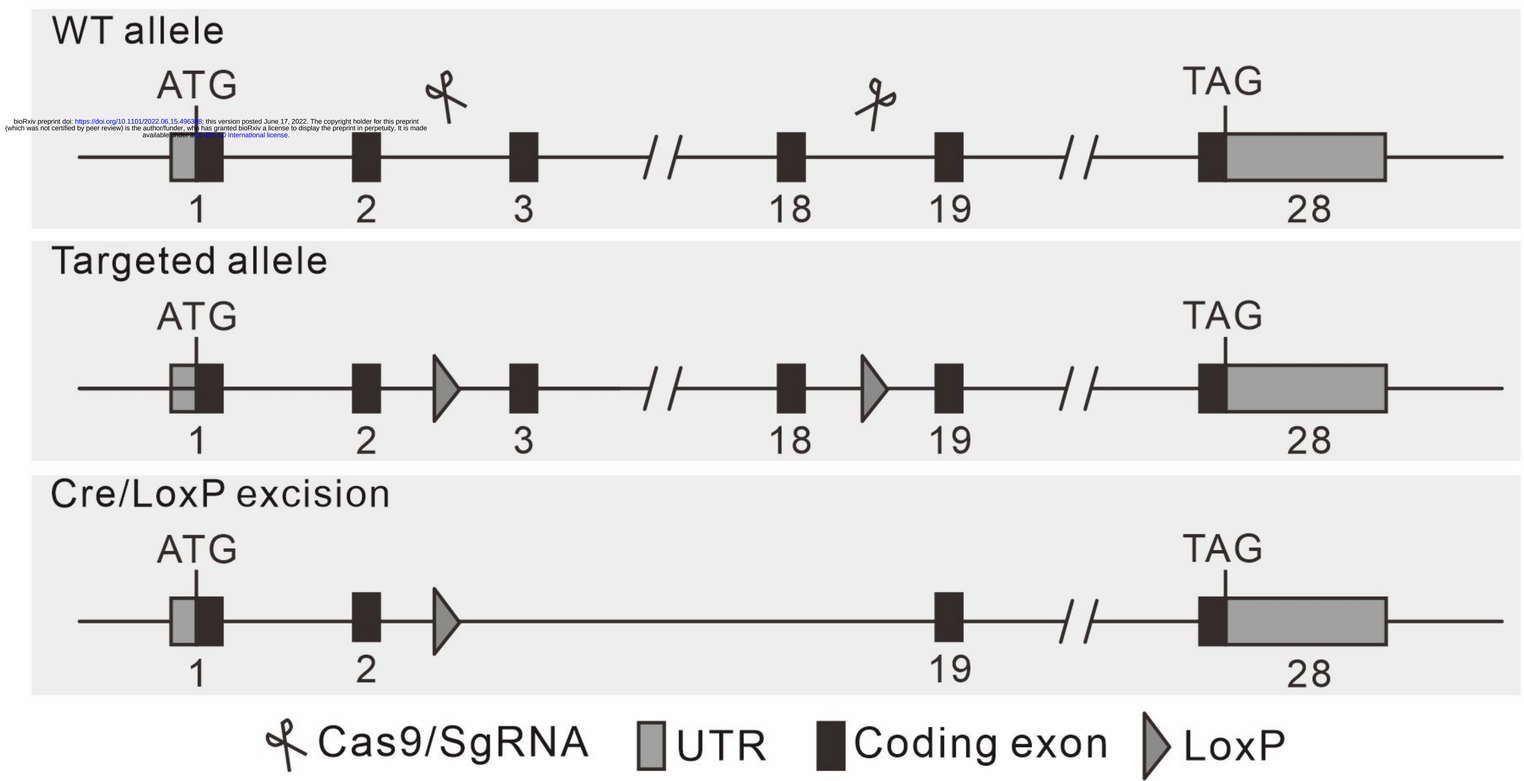

L

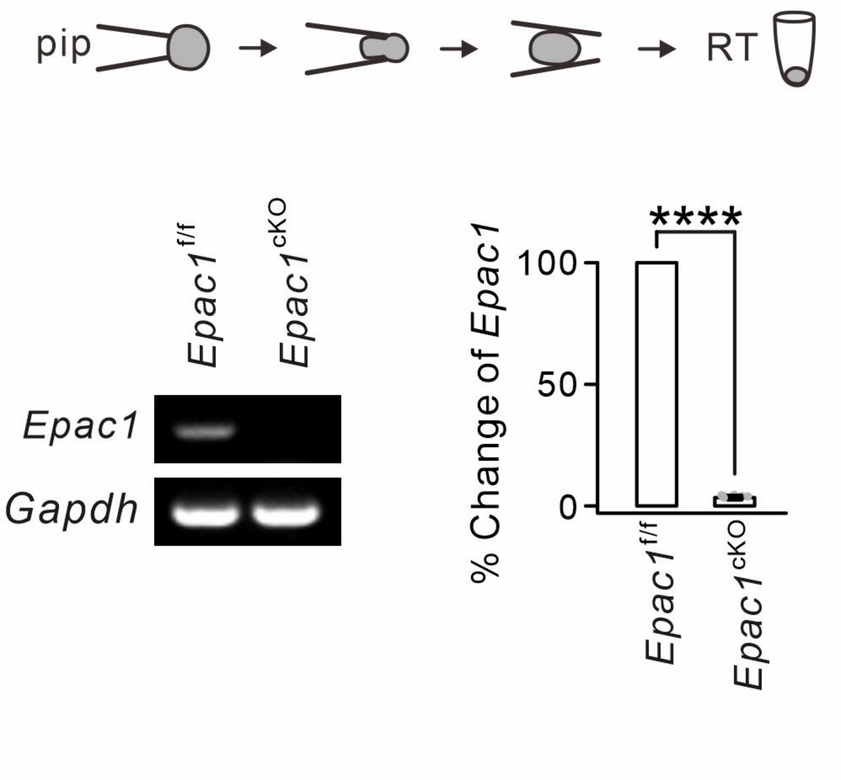

A

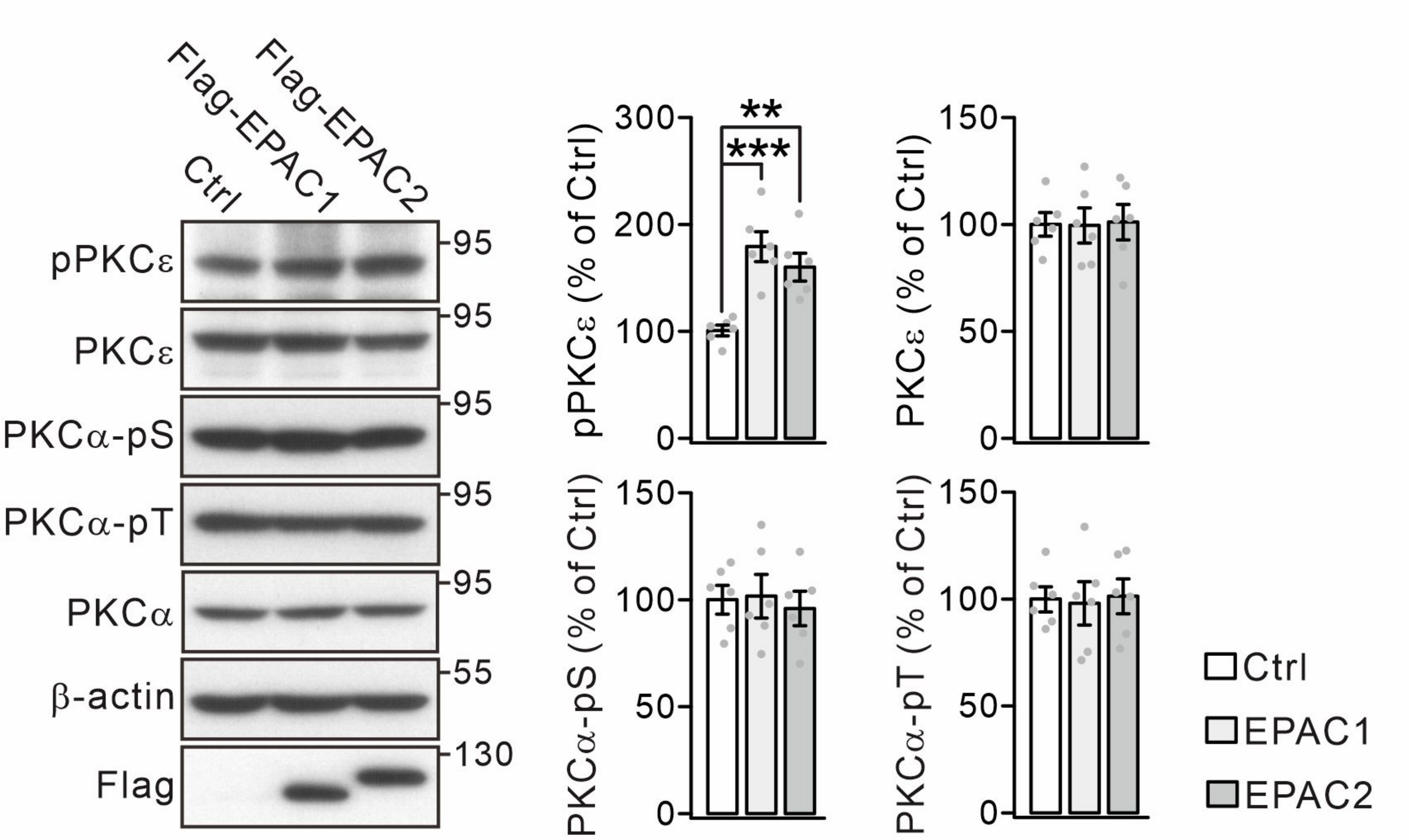

B

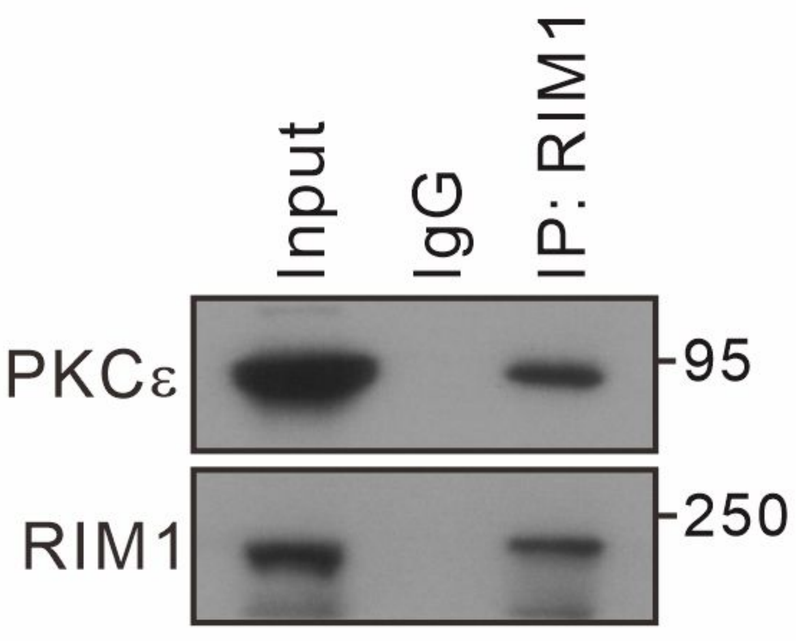

C

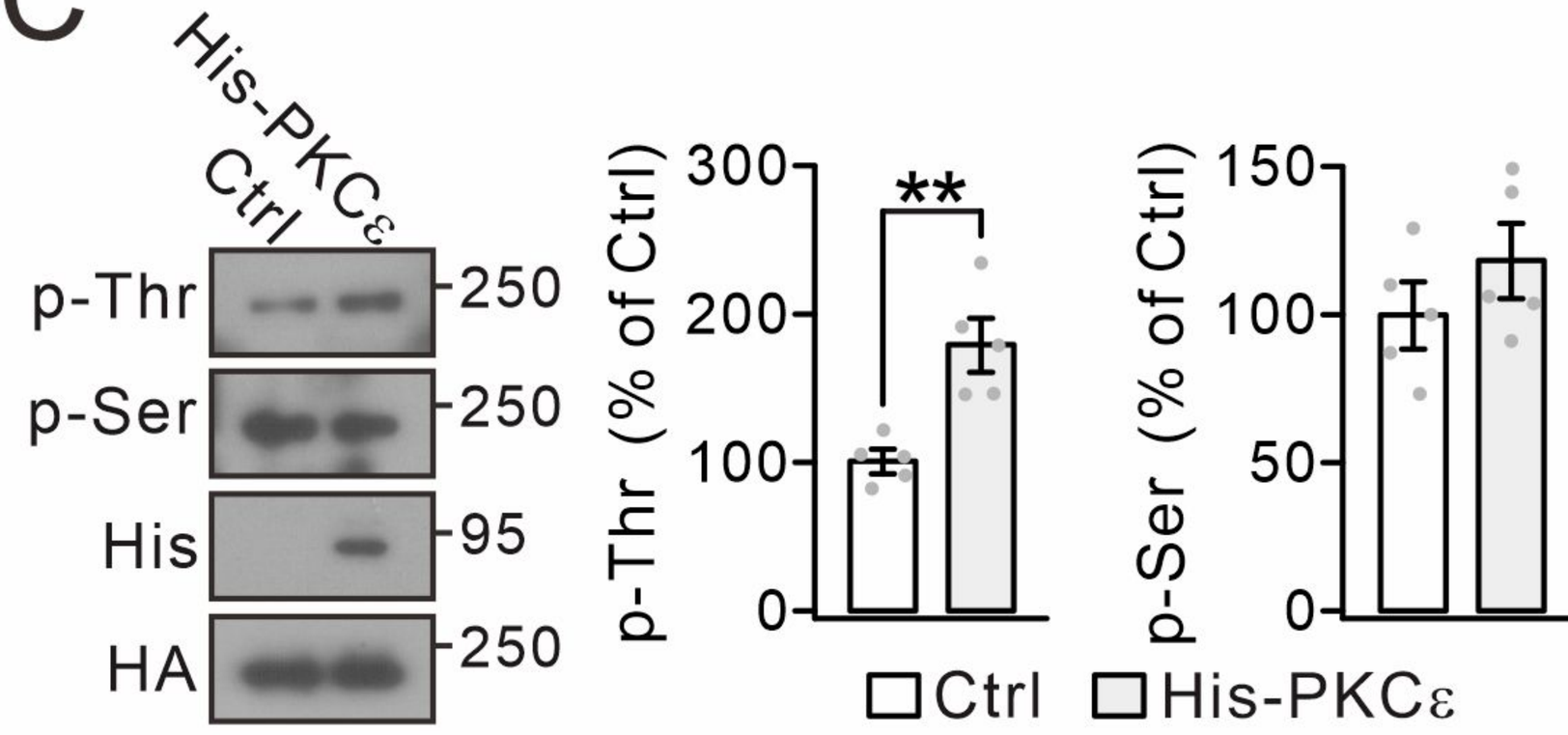

D

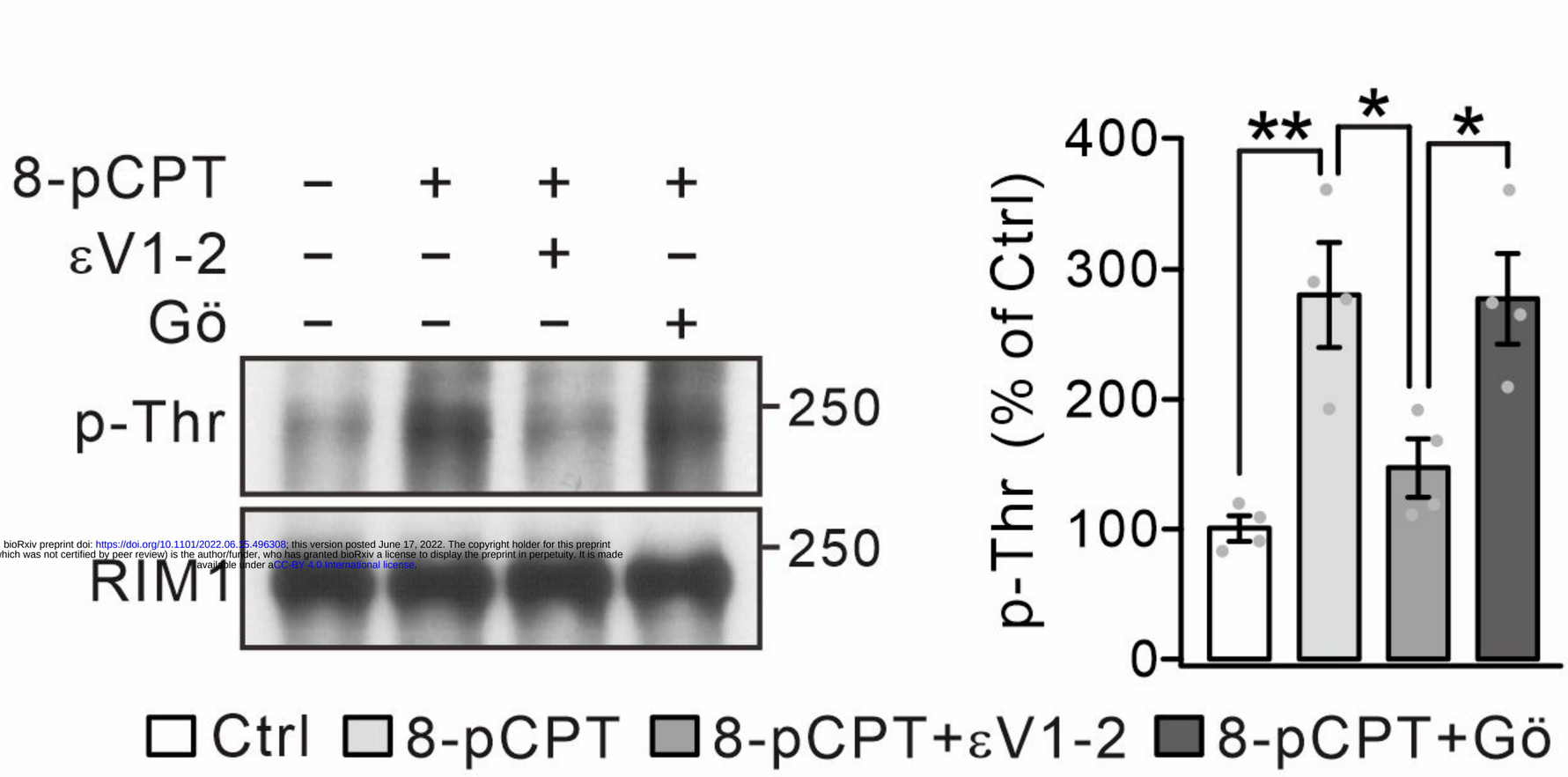

E

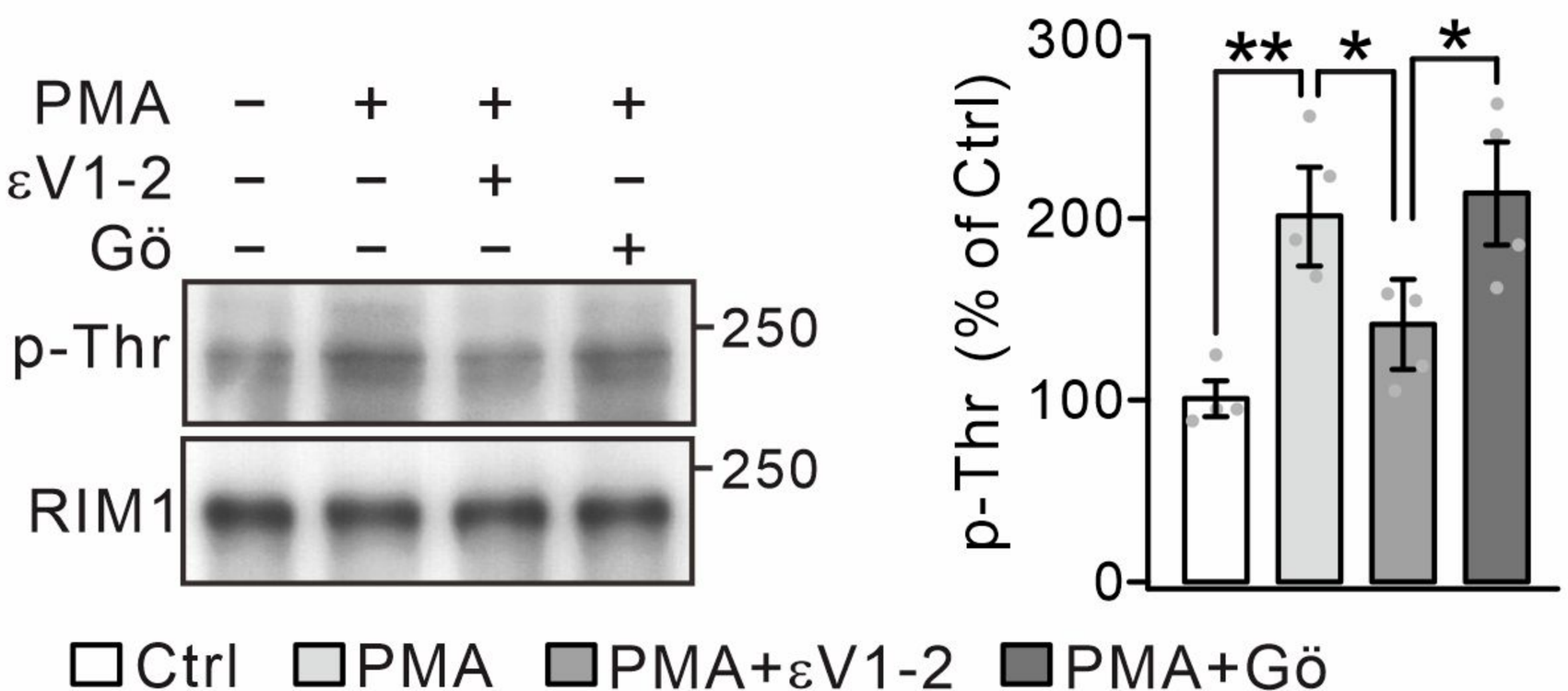

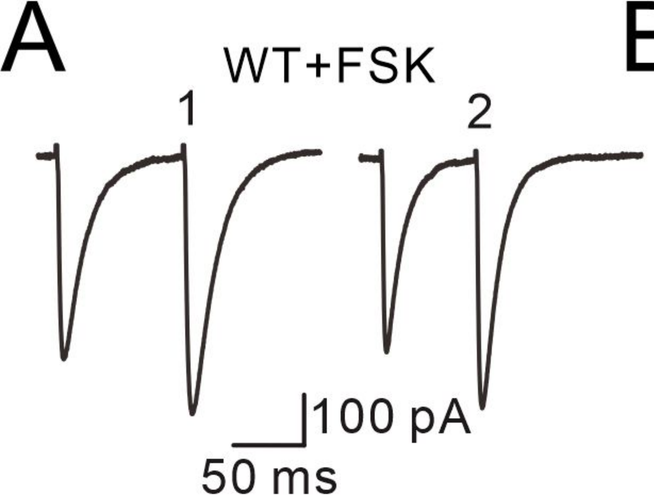

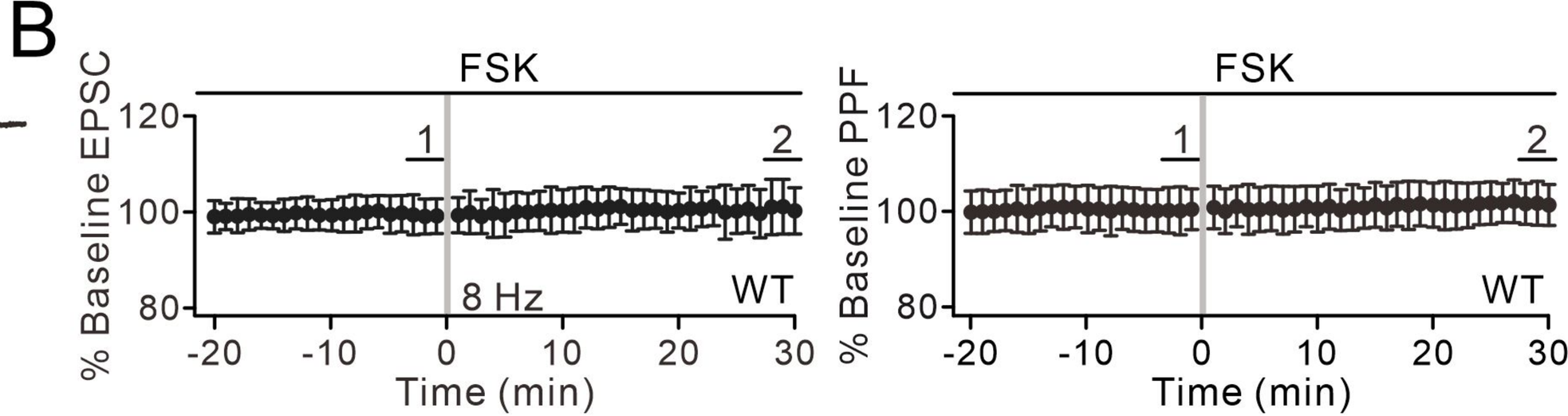

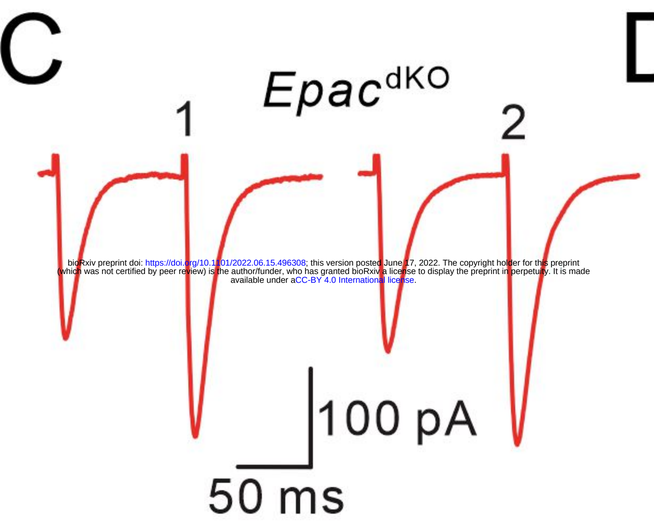

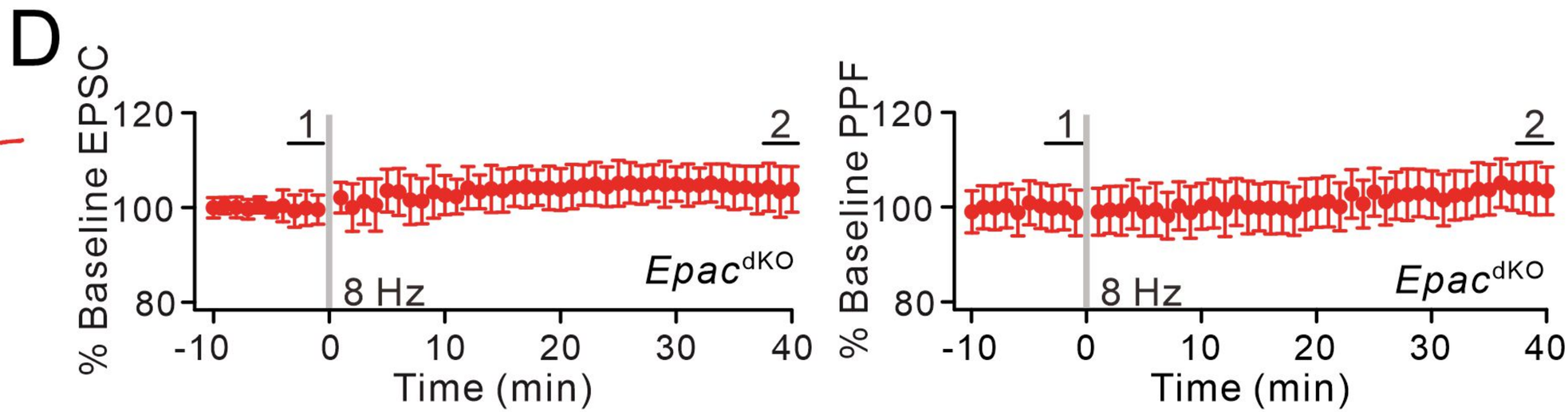

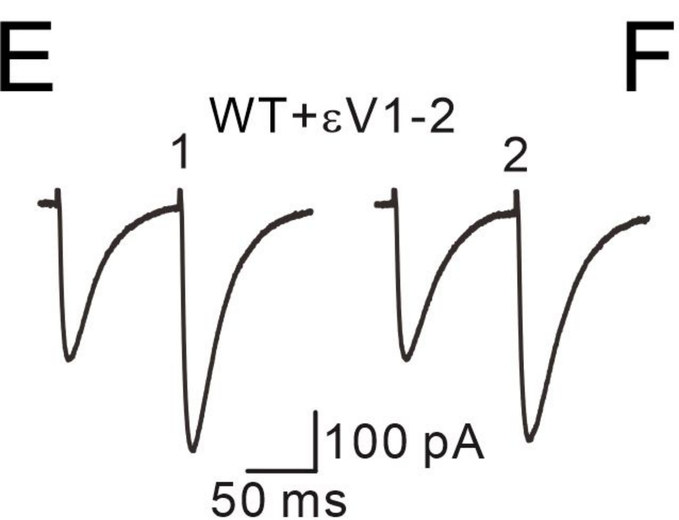

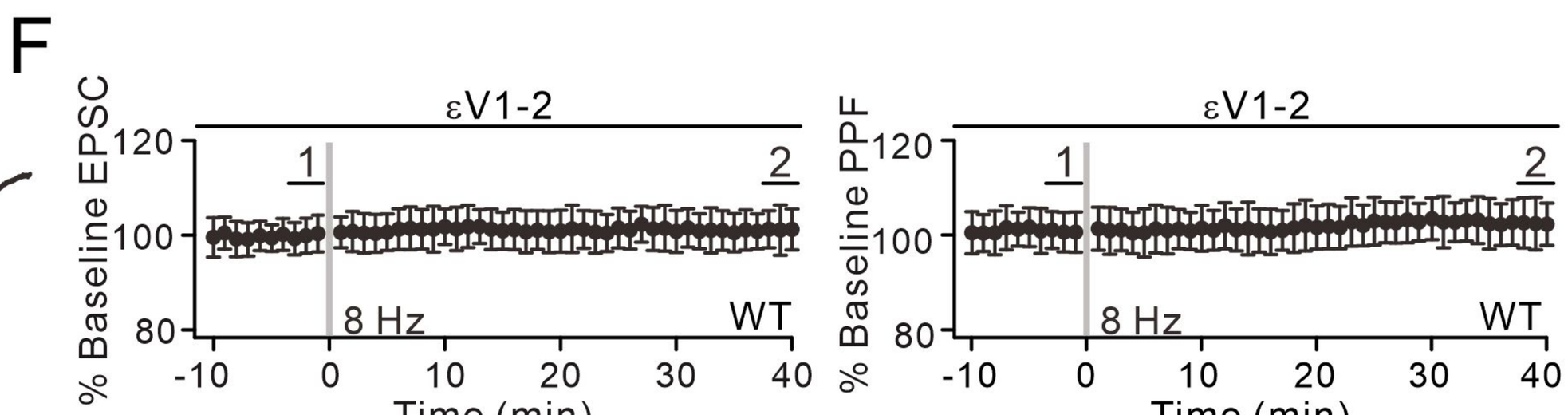

A

OKR

Gain

Phase

WT

Epac^{dKO}

**

**

B

VOR

Gain

Phase

**

*

C

VVOR

Gain

Phase

Stimulus oscillation frequency (Hz)

D

VOR phase reversal

Gain

Phase

*

**

**

**

**

**

**

***

***

Day 1

Day 2

Day 3

Day 4

Day 5

Parallel fiber

cAMP

EPAC

PKCε

P

Thr P

PKCε

Rim1

Rab3

Munc13

Rim1

Glu

GluA2/3

GluA1/2

Purkinje cell

Time

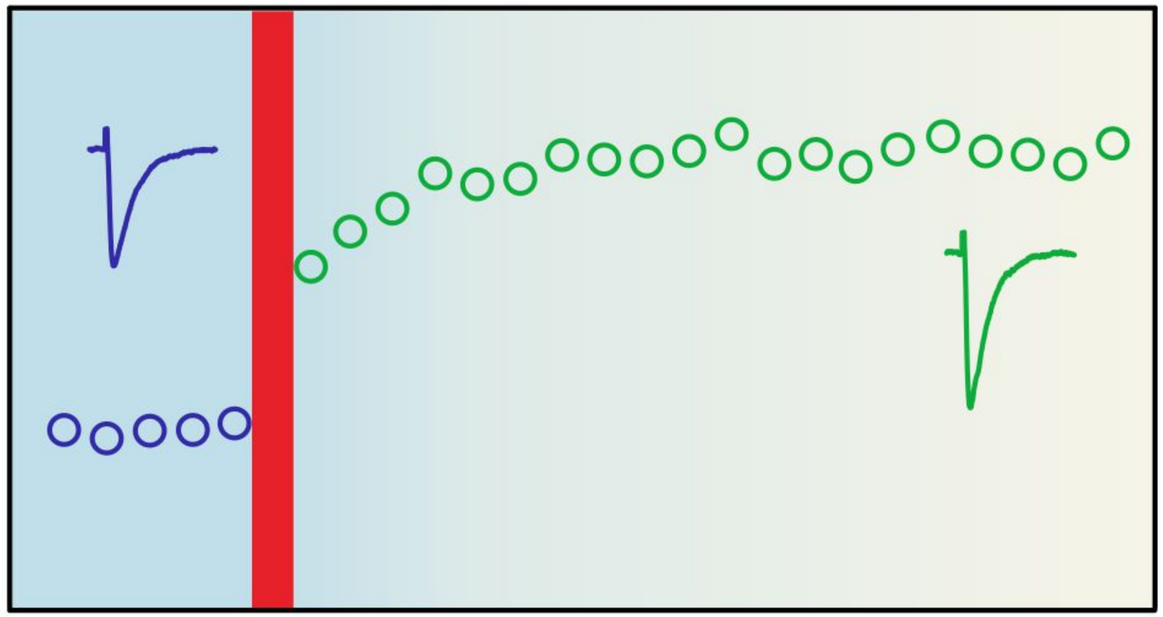

Presynaptic LTP

Motor learning

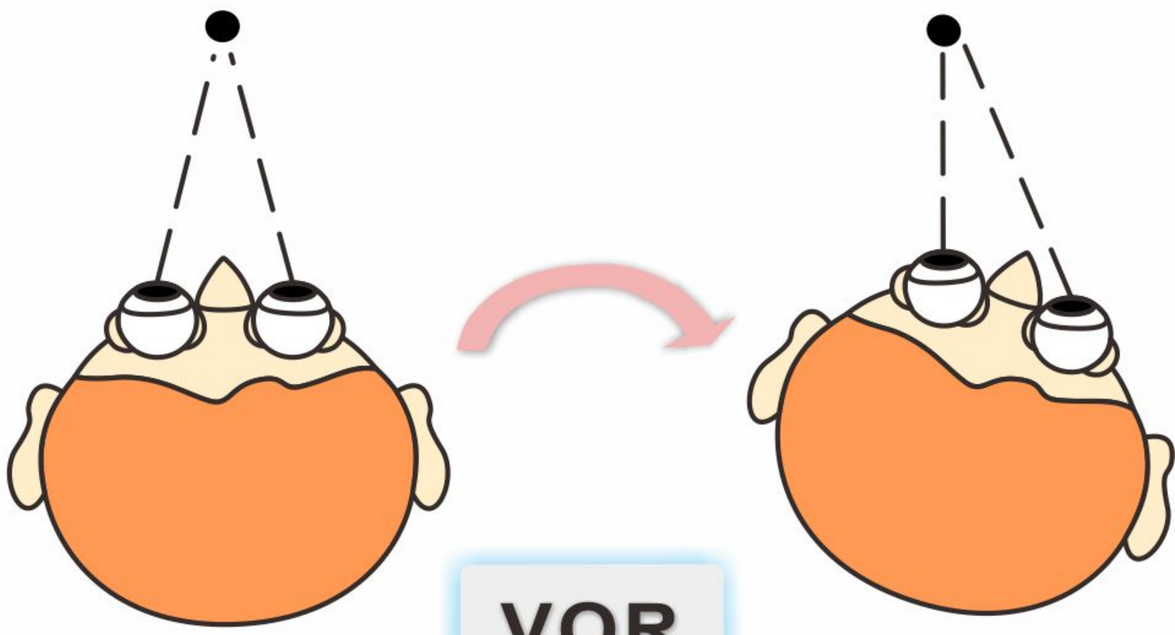

VOR